Universidade de Lisboa
Faculdade de Ciências
Departamento de Física

An SiPM-based PET-TOF demonstrator:
Test and evaluation of the image reconstruction software and implementation of a TOF algorithm for improved imaging

Liliana Filipa Nunes Pereira

Mestrado Integrado em Engenharia Biomédica e Biofísica

Perfil em Radiações em Diagnóstico e Terapia

Dissertação orientada por:

Professor Doutor Pedro Almeida

2016

Universidade de Lisboa
Faculdade de Ciências
Departamento de Física

An SiPM-based PET-TOF demonstrator:
Test and evaluation of the image reconstruction software and implementation of a TOF algorithm for improved imaging

Liliana Filipa Nunes Pereira

Mestrado Integrado em Engenharia Biomédica e Biofísica

Perfil em Radiações em Diagnóstico e Terapia

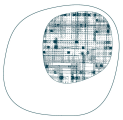

PETsys Electronics SA

Dissertação orientada pelo Professor Doutor Pedro Almeida com Agregação da Faculdade de Ciências da Universidade de Lisboa

2016

Acknowledgements

The work presented in this thesis benefited from the contribution of people I had the pleasure to meet and work during these months and the support of those who accompanied me during this small adventure. Therefore, I would like to express my gratitude to those who directly or indirectly helped to make this work possible.

I would like to thanks to my supervisor Professor Pedro Almeida for all help and support, for the opportunity to participate in this project and guidance throughout these months. A special thanks for trusting in my capabilities and for reviewing this thesis.

To my colleagues from PETsys, for being always available to share their knowledge with me and answer all my questions. Their expertise, understanding and patience added considerably to my project. Specially, to Tahereh Niknejad, who supervised my work during the first months in the project and introduced me to the endless details of the SiPM TOF-PET demonstrator and the ongoing project. Her constant concern on providing me good work conditions, the team work, the guidance and the numerous work discussions were clearly decisive on putting this work on its path.

From IBEB, I would like to express my thankfulness to Professor Eduardo Ducla-Soares, whose energy, initiative and fascination for science are truly inspiring; and to Professor Nuno Matela for the interesting suggestions, for encouraging me to come to this project and for being available to help me at any time.

I would like to express my truly and deeply gratitude to my family and friends that always supported me in the best and the worst moments. There are no words to describe how grateful I am to my parents and my brother for their trust in my capabilities. To Ana Borba for the endless patience and for always being by my side. A very special thanks to Tatiana Ladeira for the incentive and unconditional support and love.

Thank you all for the your precious contribution!

Resumo

O cancro da mama é a neoplasia maligna com maior taxa de incidência nas mulheres, sendo também uma das maiores causas de morte por cancro. Nos últimos anos têm sido realizados esforços no sentido de se desenvolverem novas técnicas imagiológicas que permitam uma deteção do cancro da mama no seu estado mais inicial. O uso destas técnicas permite a existência de um da doença com metodologias menos agressivas para o paciente e potencialmente mais eficazes. Estas novas técnicas visam também ultrapassar as dificuldades sentidas pelas técnicas mais antigas em analisar, por exemplo, mamas densas, ou até em detetar lesões em zonas anteriormente de acesso muito difícil, como a zona axilar.

Atualmente, a tecnologia de imagem médica mais usada para a deteção e acompanhamento destas neoplasias é a mamografia por raios-X. Outros métodos de imagem, tais como os ultrassons e a ressonância magnética, desempenham um papel importante como técnicas auxiliares à mamografia por raios-X, principalmente quando a sensibilidade do uso de raios-X é baixa (por exemplo, devido a uma elevada densidade da mama). As tecnologias acima referidas produzem, essencialmente, imagens anatómicas, não sendo capazes de obter informação sobre alterações funcionais ou metabólicas nos tecidos. Assim, os métodos de imagem médica molecular, como são a Cintigrafia, a Tomografia Computorizada por Emissão de Fotão Único (SPECT) e a Tomografia por Emissão de Positrões (PET), introduzem informação complementar aos métodos de imagem anatómica. No entanto, estas técnicas de imagem funcional estão direcionadas para imagens de corpo inteiro, verificando-se uma baixa sensibilidade de deteção das pequenas lesões da mama. Neste contexto, tem-se assistido nos últimos anos à criação de equipamentos compactos baseados na cintigrafia e na tecnologia PET, com elevada sensibilidade para detetar as neoplasias características do cancro da mama. Esta evolução, direcionada para a imagem no diagnóstico e tratamento do cancro da mama, surge assim, como uma nova tecnologia designada por Mamografia por Emissão de Positrões (PEM).

A Mamografia por Emissão de Positrões (PEM) é uma técnica promissora e decisiva na conquista deste objetivo. A PEM apresenta-se como uma técnica imagiológica funcional e não-invasiva, que se dedica à imagem da mama, partilhando os seus princípios físicos com a tomografia por emissão de positrões (PET). Alguns sistemas de imagem têm sido desenvolvidos neste âmbito, no contexto dos quais surge o novo protótipo desenvolvido e aqui estudado e que se denomina SiPM-based PET-ToF demonstrator. Este apresenta-se como um scanner de alta resolução e sensibilidade com capacidade de obtenção precisa de informação do tempo-de-voo (TOF) das partículas após aniquilação, desenvolvido pela

PETsys Electronics, S.A em parceria com o consórcio de PET e com o LIP - Laboratório de Instrumentação e Física Experimental de Partículas. O SiPM-based PET-ToF demonstrator apresenta uma geometria de ângulo limitado que proporciona flexibilidade na colocação do scanner ao redor do paciente, bem como a possibilidade de o de combinar com outras técnicas de imagiologia e diagnóstico.

É de grande importância referir que o protótipo avaliado ao longo deste projeto foi desenvolvido com capacidades para obtenção da informação do tempo-de-voo das partículas, característica que tem sido alvo de muitos estudos para obtenção de melhores resultados na reconstrução da imagem final. Ou seja, através da integração da informação do tempo-de-voo das partículas no software de reconstrução de imagem é possível estimar a localização precisa do local onde ocorreu a aniquilação dos positrões ao longo da linha-de-resposta (LOR) estimada. Isto tem importância na reconstrução de imagem, uma vez que permite obter uma melhor e mais correta quantificação da imagem final, melhorando por consequência a deteção de uma possível lesão.

Com base nisto, o trabalho desenvolvido no âmbito desta dissertação de mestrado tem como principal propósito avaliar e melhorar o software de reconstrução de imagem utilizado pela PETsys Electronics S.A, especificamente para o *SiPM-based PET-ToF demonstrator*, bem como a inclusão do algoritmo de tempo-de-voo nesse mesmo software. Para tal, recorreu-se ao método de simulação de Monte Carlo. A metodologia adotada procurou reproduzir de uma forma realística, a geometria do detetor, o ambiente de radiação e fatores instrumentais relacionados com o sistema de imagem. Foram executados testes para validação dos dados simulados recorrendo ao uso de dados obtidos experimentalmente. Foram também avaliados os dados experimentais de forma a obter a resolução espacial intrínseca do protótipo em estudo.

Após validação da geometria simulada do *SiPM-based PET-ToF demonstrator*, foi avaliado o processo de normalização, já utilizado para outros scanners desenvolvidos na PETsys Electronics S.A, para correção de artefactos na obtenção da imagem final. Este estudo foi feito com base em dados obtidos através de simulações de Monte Carlo, e teve como principal objetivo otimizar o processo de normalização utilizado especificamente para este novo protótipo. Após validação e otimização da metodologia de normalização no processo de reconstrução de imagem, o software foi alterado de modo a incluir o algoritmo do tempo-de-voo. Para validação desta alteração, foi realizado um estudo recorrendo a simulações de diferentes fantomas, onde as imagens foram posteriormente reconstruídas utilizando o software com e sem o algoritmo de tempo-de-voo. A resolução espacial, o número de contagens, a sensibilidade e a razão sinal-ruído foram alguns dos parâmetros avaliados ao longo desta tese.

Os resultados obtidos demonstraram que os fatores utilizados no processo de normalização têm uma grande influência no que diz respeito a estimar imagem final, uma vez que permite a obtenção de imagens com formas melhor definidas e com menos ruído de fundo. Da mesma forma, a integração do tempo-de-voo na metodologia de reconstrução de imagem confirmou ser um ótimo complemento, uma vez que permitiu a obtenção de melhorias na qualidade das imagens. No entanto, é importante realçar que foram verifica-

dos alguns erros durante o tratamento dos dados desta última parte do estudo apresentado nesta tese, que necessitam de ser avaliados e corrigidos futuramente.

Palavras-Chave: Tomografia por Emissão de Positrões (PET); Mamografia por Emissão de Positrões (PEM); Tempo-de-Voo; Simulação de Monte Carlo; Reconstrução de Imagem.

Abstract

Positron Emission Mammography (PEM) with 18F-Fluorodeoxyglucose is a functional imaging technique useful for breast cancer detection. The improvement of the detection of early stage breast cancer depends on the development of dedicated imaging systems with high sensitivity and spatial resolution. Also, many studies have supported the inclusion of time-of-flight information in the image reconstruction methods since this can allow for the improvement of image quality and quantitative accuracy, thereby improving lesion detectability. The SiPM-based PET-ToF demonstrator is a high resolution and sensitivity scanner with TOF capabilities developed by PETsys Electronics, S.A. in partnership with the PET-Consortium (eight technology and medical institutions, since 2003) and LIP-Laboratory for Particle Physics, Lisbon (Detector and electronics development for CERN experiments since 20 years).

The work presented in this thesis focus on the study of the performance of detector imaging quality and on the inclusion of TOF algorithm in the image reconstruction method used in the PETsys Electronics Systems. The image reconstruction method used during the work was already studied for the Clear-PEM system and it's here adapted for the SiPM-based PET-ToF demonstrator geometry and configuration. To achieve this, a realistic design of the detector was performed in the software used for numerical simulations of the final imaging. Monte Carlo data was provided to validate and optimize the changes done in image reconstruction algorithm and to investigate the normalization process in final imaging acquisition.

It was demonstrated that the normalization factors used in image reconstruction have a big influence in the final result obtained, since it allows to obtain better defined image shapes and with less background noise. Similarly, the integration of time-of-flight information has confirmed to be of value in image reconstruction methodology, since it improves PET imaging quality. However, the image reconstruction methodology proposed here is still imperfect, resulting in the need for future work.

Keywords: Positron Emission Tomography; Positron Emission Mammography; Time-of-flight; Monte Carlo simulation; Image Reconstruction.

Contents

List of Tables

List of Figures

Chapter 1

Context and Main Goals of the Work

Due to high incidence and mortality rates specially in women, breast cancer is a great concern worldwide. A number of different types of cancers can develop within different areas of the breast. Among the most common types are carcinomas *in situ* and the invasive carcinomas. Carcinomas in situ are cancerous lesions that have not penetrated into other breast tissues surrounding their region of origin. This type of breast cancer is usually classified as a pre-invasive form of breast cancer since it is a precursor, in the majority of the cases, of invasive carcinomas, which are the most dangerous ones.

The detection of breast cancer on its early stage opens the path to early therapeutic interventions, resulting in less aggressive treatments and increased chance of cure. Based on this, many studies have been performed in order to achieve better imaging results for different types of imaging modalities. Positron Emission Tomography (PET) imaging can contribute decisively towards this objective. PET is a functional technique, where an abnormal increase of cell metabolic activity may be detected before anatomical manifestations develop. However, the spatial resolution of whole-body PET scanners prevents the detection of lesions smaller than about 1 cm, which threatens the detection of this disease.

These limitations have encouraged an active interest in the development of compact positron emission tomography cameras dedicated for breast imaging, a technique named Positron Emission Mammography. In the last 20 years there has been a great effort from the industry and scientific community to develop such devices, with a variety of detector designs and geometries, innovative radiation detection schemes, new scintillation crystals and adapted image reconstruction algorithms being studied in order to optimize this technique.

Among PEM systems, the Clear-PEM, was developed within the framework of the CrystalClear collaboration at CERN. Clear-PEM is composed of a dual-plate detector head that is housed in a robotic mechanical gantry, which allow the examination of the breast and the axilla regions. The detector heads can be positioned at different separation distances, allowing for the accommodation of different breast sizes. The unusual geometry of this system gantry and specific acquisition characteristics demand the development of dedicated software. Many studies were performed for this system, some benefits were

found, but also some limitations. In order to overcome some of the limitations presented in Clear-PEM system, a new detector appears within the framework of the CrystalClear collaboration at CERN, the SiPM-based PET-ToF demonstrator.

The SiPM-based PET-ToF demonstrator is a high resolution and sensitivity scanner with TOF capabilities developed by PETsys Electronics, S.A. in partnership with PET-Consortium (Eight technology and medical institutions, since 2003) and LIP-Laboratory for Particle Physics, Lisbon (Detector and electronics development for CERN experiments since 20 years). The detector is a high resolution small animal PET scanner, which can be adapted to breast cancer imaging due to its configuration. Demonstrator presents a limited angle geometry can provide flexibility in detector placement around the patient as well as the ability to combine it with other imaging modalities.

It is important to highlight that the referred prototype was developed with TOF capabilities, which can introduce a great improvement in image reconstruction. Since TOF algorithm allows to estimate the precise location of the positron annihilation along the line-of-response. Included in the image reconstruction methodology, TOF information can improve image quality and quantitative accuracy, thereby improving lesion detectability. Based on this, many studies about image reconstruction in PET systems, that are going to be further referred and better explained in the State-of-Art of this Thesis, have supported the inclusion of time-of-flight information in the image reconstruction algorithm.

Accordingly, the main aim of this dissertation is to study the inclusion of TOF information in the image reconstruction methodology used in the PETsys Electronics System. Which will allow to better understand the benefits and the limitations of the inclusion of TOF algorithm on image quality and specificity, for a specific software and system (SiPM-based PET-ToF demonstrator). To achieve this purpose, the image reconstruction method already developed for the Clear-PEM system need to be tested and adapted for the new system. Only after that, it's possible to add the TOF algorithm in the image reconstruction method, which was developed in C++. Also, a realistic design of the detector needs to be performed in the software used for numerical simulations of the final imaging. Simulation and design of different phantoms is similarly required for data acquisition purposes.

Chapter 2

Background

2.1 Positron Emission Tomography

Positron emission tomography (PET) is a nuclear medicine imaging technique that uses radioactive markers to enhance the visualization of metabolic processes on cells with a specific behaviour of interest. Therefore, the use of an appropriate radiopharmaceutical, also known as tracer, allows PET technique to study of a wide range of disorders. This tracer has in its composition a radionuclide tagged to a pharmaceutical that participates in a specific physiologic function or has preferential uptake on a specific organ. In contrast to computed tomography (CT) and magnetic resonance imaging (MRI) that provide essentially detailed anatomical or morphological information, PET shows great superiority in monitoring the functional metabolism in normal and neoplastic tissues [1]. Current whole-body PET scanners allow multipurpose, whole-body or region specific scans. As result, Oncology, Neurology and Cardiology are the main areas where this technique is used.

18F-uorodeoxyglucose (FDG) is the most used radiopharmaceutical for oncology purposes, which is a glucose analogue that has a higher uptake on cells with high energetic needs, as the ones undergoing fast proliferation. To do a FDG-PET exam, FDG is injected intravenously in the patient, then this compound will travel through the bloodstream until it is captured by cells with high metabolism, like tumour cells. The radionuclide, due to its natural radioactive decay, emits one positron per decay that will annihilate with a nearby electron. This annihilation will give rise to two 511 keV photons ejected in nearly opposite directions, which will travel through tissues and escape the body finally interacting with PET detectors. As this interaction produces light, it will then be processed by the system, which comprises a detection chain including photo-detectors and signal converters, to obtain a volumetric image representation of the emission sites. Each pair of photons detected in coincidence represent a line, called coincidence line-of-response (LOR), along which the photons were emitted. Evaluating all the LORs and intersections between them from all detected coincidences, it's possible to map the spatial distribution of the tracer inside the body.

Of special interest to oncology, PET allows detecting an abnormal increase of the metabolic activity may be detected before anatomical findings take place. So this func-

tional information provided by the PET technique can increase the chances of early cancer detection provided by anatomical imaging techniques. As an example, the sensitivity and specificity of whole-body PET for breast cancer detection has been reported as 85% and 79%, respectively [2]. For dense breast PET imaging do not represent a problem for lesion detection, since the decision is based on a higher radio-pharmaceutical uptake and not the tissue's density. Also, for axilla imaging and detection of metastasis on breast cancer patient's whole-body PET showed to be suitable. However, spatial resolution of current whole-body PET scanners (4-6 mm) limits the detection of low-uptake sub-centimetre lesions [3]. This fact associated with the costs of a PET study makes its use as a screening tool not cost-effective. PET is not clinically indicated as a breast cancer detection tool [4].

Based on this, there has been considerable advancement of the technology and instrumentation in PET over the last 30 years since the first tomography ring systems were developed. Significant improvements have been made in detectors, hardware, and image processing that impact both image quality and accuracy of quantification.

Figure 2.1: Positron emission scan of the whole body.[5]

2.2 Positron Emission Mamography

Breast cancer imaging is an example of how medical imaging modalities can diminish the number of patients suffering from this highly prevalent and deadly disease. The most used technique for breast cancer imaging is X-ray mammography, which is used as a complementary tool to clinical diagnosis and a screening tool for the early detection of the disease. The main problems of this technique are related with its low sensitivity in women with dense breast tissue and low specificity in the detection of malignancy. Other imaging

methods such as breast Magnetic Resonance Imaging and Echography play important roles as adjunct techniques to X-ray mammography. Nonetheless, the information provided by the aforementioned techniques is mainly anatomical, thus leaving space for imaging methods that are able to obtain information regarding functional or metabolic changes in tissues [2].

Based on these, molecular imaging methods using labeled radiotracers such as Scintigraphy, SPECT, Positron Emission Tomography (PET) and PET-CT, have been found to provide useful complementary information to the anatomical methods regarding detection diagnosis and staging of breast cancer. Nevertheless, the standard technology of whole body scanners has in part precluded molecular imaging using radiotracers from contributing with its full potential to the imaging of the breast, due to its limited spatial resolution and to its disadvantageous geometry, which limits sensitivity [7].

These limitations have prompted an active interest in the development of compact positron emission tomography cameras dedicated for breast imaging, a technique named Positron Emission Mammography (PEM). This technique uses adequate types of crystals, photodetectors and associated electronics, an increased interest over the last years on breast cancer dedicated scanners has been seen. In these systems detectors are closer to tissue, have smaller detectors and depth-of-interaction measurements, which increases the sensitivity and the spatial resolution when compared to whole-body PET scanners. Also, allow suitable geometries for the body part under study and are less expensive than whole-body PET scanners [3, 20].

Either as prototypes or as commercial equipment, PEM scanners have provided data that confirms a huge improvement in technical characteristics with regards to whole body scanner, thus showing great promise of becoming a valuable modality in the clinical practice. In fact, Positron Emission Mammography, for which there are now two commercial equipment available, has demonstrated higher detectability than PET/CT and comparable or better sensitivity than MRI. It seems now to be clear that PEM is valuable technique when MRI cannot be used [5, 21].

In this section, a brief description of the principles behind the tomographic method for molecular imaging isotopes and the performance parameters of dedicated PEM scanners will be reviewed. Since the study presented in this thesis was developed in the scope of the SiPM-based PET-TOF demonstrator, which is a high resolution scanner dedicated for breast imaging.

2.2.1 Principles of PEM

PEM uses the same physical principles underlying Positron Emission Tomography (PET) imaging. Using radio-labeled molecules it's possible to image structures of interest, since the metabolism of those molecules inside the human body follow a known path or participate in a reaction of interest. As it was previously referred, the 18F-fluorodeoxyglucose (FDG) is the widely used radiopharmaceutical in the context of cancer assessment for nuclear medicine techniques, which consists of glucose labeled with Fluorine-18. After injection of this compound, it will travel through the blood stream towards cells with high

energetic needs, as cancer cells, due to high metabolic activity and enter phosphorylation along with normal glucose molecules. However, instead of one of the hydroxyl groups that composes normal glucose, this glucose analog has the 18F isotope, which will prevent further phosphorylation, trapping the molecule inside the cell. The 18F atom has an unstable nucleus with an excess of protons, which means that is a positron emitter. It decays into 18O by conversion of a proton to a neutron and emission of a positron and a neutrino. This interaction will allow the molecule to recover the hydroxyl previously missing and proceed to glycolysis (glucose degradation resulting in energy production), by capturing a H^- from the surrounding aqueous medium that will bond to the Oxygen.

The positron resulting from the radioactive decay process is of great interest for imaging purposes. Due to interactions with electrons of the tissues, it will progressively lose its energy until annihilates with a nearby electron, when the remaining energy allows to assume both particles are at rest. The annihilation process produces two photons which, due to energy and momentum, are emitted 180° apart and that's described as back-to-back emission. Both photons are emitted with the same energy (511 keV each), derived by Einstein's mass-energy equivalence $E{=}mc^2$, where m is the sum of both particles masses and c is the speed of light.

Gama photons cross the tissue until they reach high density crystals composing the detector and interact by photoelectric effect, depositing all their energy. The annihilation's origin is estimated by the line joining the two opposite detectors where these interactions took place and, since positrons' range in tissue is small, it's also possible to estimate an activity distribution.

It is important to highlight that, although gamma photons present high energy and good chances of escaping tissue and be detected, it is not straightforward that all photons will in fact reach the detector or, if they do, that their path was undisturbed and the line joining both detectors passes on the annihilation site. Effects and interactions, as Photoelectric effect and Compton scattering, can occur generating inaccuracies in the determination of the activity distribution. Ultimately, a loss of photons can also happen due to their direction or interaction in the tissue.

2.2.2 Types of Detected Events in PEM

After positron-electron annihilation, which is usually known as an event, one or both emitted photons can interact while traveling on surrounding tissues, or finally with the detector components. In a PEM acquisition, an event is recorded by the system if two photons reach the detector within the coincidence time window defined. This finite width called time window allows the possibility that two uncorrelated single detection events occurring sufficiently close together in time can be mistakenly identified as a true coincidence event. To represent the possible positions where the annihilation took place, the line that joins two detector crystals in coincidence is defined and it's called Line-of-Response (LOR). The recorded events are known as prompt events and include information about true coincidences, random, scattered and also single and multiple events. The three first types of events are later written to a List Mode File (LMF) for posterior processing and

reconstruction. The other two, single events and multiple events, are not useful for activity distribution recovery and therefore will not be include in the LMF, however the detection system has to deal with them.

Accordingly, events can be classified in:

Single events. When a one photon of a coincidence pair reaches the detector during the time window defined, it is called a single event. This effect occurs for approximately 90% of all the photons detected [6]. Main causes for the loss of the second photon are due to trajectories that do not lead the photon towards the detector or interactions with the medium resulting in absorption or severe loss of energy.

Multiple events. Multiple events are, conversely to single events, caused by the detection of more than two photons in the same time interval, invalidating the attribution of a single LOR to this event. An example of this situation is when a simultaneous detection of a true and a single event happens. The data acquisition system discards these interactions.

True events. If two photons which had their origin on the same annihilation and traveled through tissue without interaction, finally reaching the detector, it is called a true event. Both photons maintain their original energy and direction information since no interaction occurs along the path. This allows an accurate determination of the activity distribution on tissues. Ideally, a Positron Emission Tomography acquisition would only detect this type of events.

Random events. These type of events are described as two uncorrelated photons originated from two different annihilations reaching the detector during the time interval defined by the time window and being accepted as a true coincidence pair. Random events do not reflect the actual distribution of the radiotracer since were not originated by the same positron-electron annihilation. As the counting rate raises, the probability of occurrence of these events increases. The random rate Rr for each LOR is proportional to the square of the singles rate Sr and the length of the time window T. Its dependence with the singles rates for detectors i and j defining the LOR can be described by Equation 2.1. The probability of detection of this type of events will therefore increase with higher activities.

$$Rr_{ij} = 2\tau Sr_i Sr_j \tag{2.1}$$

Using low count-rate studies and using fast scintillation crystals and electronics it's possible to obtain a decrease in the counting of random events, which also reduce system's dead time. The main responsible for the detection of random events in a PEM system is the activity from outside the Field-Of-View (FOV).

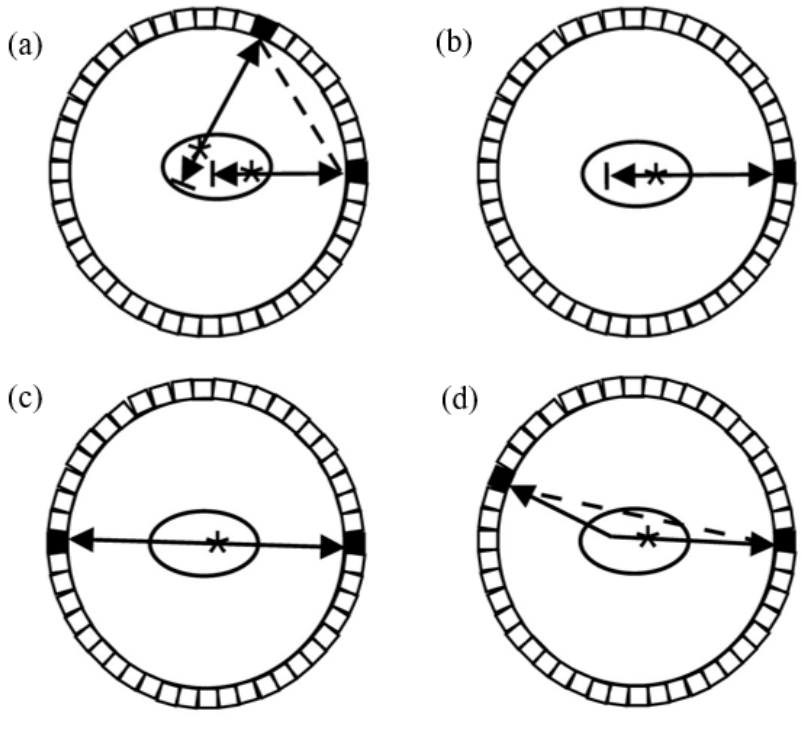

Figure 2.2: Detected events in PET: a) Random Coincidence; b) Single Event; c) True Coincidence; d) Compton Event. [3]

Scattered events. Energy and directional information of an event will change if photons from the same annihilation undergo a Compton scatter interaction. Nevertheless, they maintain their time information nearly unchanged and, in case both of them reach the detector with energy above an electronically imposed threshold, they will be validated as a coincidence and recorded, independently of whether one or both photons experience scatter. When this happens the LOR attributed by the system will no longer reflect the possible points from where those photons were emitted. Since the radiation detector systems present some limitations regarding energy resolution, perfect energy discrimination is not possible and some scattered and un-scattered photons will remain indistinguishable. Some inaccuracies in activity distribution estimation will appear due to the directional information lost during the scattered process.

Organs with high glucose consumption and close to the breast tissue, such as the heart or the liver, present a special importance in PEM imaging due to their high glucose consumption. Since it will contribute to an increase of the number of detected singles, random and scatters, originated outside the field-of-view. Out-of-FOV activity can lead to image degradation and for a decrease of the imaging system's performance for high activity constrains.

2.2.3 Performance Evaluation of PEM System

System's performance on successfully detecting the smallest lesion possible with minimum dose absorption for the patient in a PEM system depends of several parameters. To compare scanners or deal with corrections for the effects of random and scatter events or

attenuation, it's necessary to know the value of some of these parameters. Accordingly, a brief description of the most important parameters, such as energy, time and spatial resolution, sensitivity and noise equivalent count rates, is provided in this subsection.

Sensitivity

The determination of the quotient between the number of detected events per unit of time and the activity emitted by the source depends of the system's sensitivity. One of the characteristics present in a PET system that directly influences this parameter is the geometric efficiency of the scanner. Dedicated scanners frequently assume unusual geometries that are more suitable for imaging a specific body part. On some cases, as detectors are closer to the region of interest, this increases the system sensitivity, but on others, some scanners will not present an angular coverage as wide as common cylindrical scanners. Thus a number of these scanners adopt a rotative operating mode to prevent the loss of statistics and deficient angular sampling.

In addition, the characteristics of the crystals used in the system, as density, atomic number and the time needed to recover from the excitation produced by an incoming photon, directly influence sensitivity. Also, presence of gaps between detector elements can compromise detection sensitivity. To prevent photons to escape or not being detected, denser crystals can be used, since it is known that higher densities lead to a higher stopping power, which combined with good scintillation characteristics increases the probability of interaction with gamma photons with crystals [4, 21]. In fact, statistical fluctuations and noisy images are consequences of low sensitivity acquisitions.

Time Resolution

The precision of the system to determine the temporal difference between the acceptance of two photons is called time resolution. Improvements in this parameter can be achieved using fast scintillation crystals and electronics. Also it is essential, to avoid losing events, to define a coincidence time window during which the photons are paired. Since photons from the same annihilation reach the detector with small time differences and crystal's characteristics also determine random delays on the production of scintillation light [6].

Using this kind of strategies narrow time windows can be defined, consequently limiting the acceptance of random events that in addition to data combination, increase count rates and ultimately can lead to dead time constraints.

Energy Resolution

In a PET scanner, the measurement of the photon's energy with a higher precision is a result of a good energy resolution. Therefore, it is important to define a narrow energy window to process the acquired data, since scattered events present lower energies and

the acceptance of them will be, in this case, much smaller. A suitable window has to be chosen when processing the acquired data, accordingly to the system's energy resolution. It is relevant to highlight that this is accomplished with nearly no cost to the sensitivity to true events.

Spatial Resolution

When two distinct point sources are close to each other is essential to distinguish them, which is directly related with the spatial resolution of the system. Measuring the response of the system to a point source at full width at half maximum (FWHM) is the most common way to evaluate this parameter that can be affect by several factors. Some of them, like positron range and photon non-collinearity, are related to the physics underlying the annihilation process. After the radioactive decay, the positron will travel a certain distance and suffer multiple interactions until annihilate with an electron from the medium. Since it's not possible to predict all of this changes of direction due to interactions, this small path is sufficient for the introduction of an offset in the determination of the annihilation position. Also, the positron range varies and depends on the radionuclide used and the medium that is crossed. For 18-F in water, it is estimated to have a range of 0.6 mm [8]. It is important to highlight that at the time of annihilation the positron is not completely at rest in spite of losing almost all its energy on several interactions. Based on this, an effect called photon non-collinearity occurs, which means that photons originated from a positron-electron annihilation will be emitted with an angle that is not exactly 180° as it was supposed. This effect is smaller when the distance traveled by photon until detection is short, which means in PET scanners with small FOV.

The size of the detector element, the precision on the determination of the detection coordinate along the crystal length and scatter on the detector elements are some other factors also known to degrade spatial resolution [9]. Scatter interactions on the detector elements can occur, resulting in an erroneous estimation of the line-of-interaction along which the annihilation took place. In order to solve some of these problems, smaller detector elements can be used to improve the ability to discriminate the interacting coordinates of the photon-crystal interaction. So, this strategy is used for dedicated or small animal scanners for imaging small structures, but at a higher monetary cost. Not only the size is important, crystals used on PET detectors present characteristics that are chosen carefully to increase the probability of a photoelectric interaction to occur between the photon and electrons from the crystal atoms. However, the distance the photon travels across the crystal until it is absorbed is variable and, in many systems, the depth-of-interaction (DOI) coordinate is not recovered, especially when small FOV scanners are used. Therefore, the developments of scanners with DOI measurement capability are becoming more common [10].

Noise Equivalent Count Rates

Strother *et al.* [11] introduced a metric to measure the statistical quality of the acquired data even before any reconstruction takes place, usually expressed in the form of Noise Equivalent Count (NEC) rate curves exhibiting a peak. The NEMA standards (National Electrical Manufacturers Association, 2001, 2008) recommend it for testing the scanner's performance. Nevertheless, this metric should be combined with others since the influence of the reconstruction algorithm used, the use of data corrections or spatial resolution effects, are taken into account [8]. To describe the NEC index, the follow equation is used.

$$NEC = \frac{r^2}{(T+S) + f_k R} \tag{2.2}$$

Where T, S and R represent the number of true events, scattered events on the object and random events present on the acquired data, respectively. Random coincidences whose lines-of-response actually intersect the object being imaged are described in the fraction f. Lastly, k shall be equal to 1 in case of noise free random rates estimates. For noisy estimates, k shall be equal to 2, reflecting the consequent doubling of the noise contribution [12].

At the end, it is important to highlight that NEC varies widely with the phantom or patient imaged. Due to all these limitations, the peak value of the NEC curve does not necessarily correspond to the best possible image that can be obtained from the acquire data [13].

2.3 Description of the SIPM-based PET-TOF Demonstrator Prototype - Concept and Design

The SiPM-based PET-TOF demonstrator prototype is a high resolution and high sensitivity scanner with TOF capabilities developed by PETsys Electronics, S.A. in partnership with the PET-Consortium (Eight technology and medical institutions), since 2003, and the LIP-Laboratory for Particle Physics, Lisbon (Detector and electronics development for CERN experiments since 20 years).

The SiPM-based PET-TOF demonstrator has an inner diameter of 230mm, featuring a highly integrated readout and a data acquisitions system (DAQ) and was used in the context of this project. The detector is a high resolution small animal PET scanner, which can be adapted to breast cancer imaging due to its configuration which is possible to verify in Figure 2.3. Also, one of the design goals of SiPM-base PET-TOF demonstrator is to increase the detection sensitivity, reducing the time needed for a complete breast exam, while maintaining a good spatial resolution. The demonstrator presents a limited angle geometry, since PET Scanner demonstrator ring is 2/3 equipped, which can provide flexibility in detector placement around the patient as well as the ability to combine it with other imaging modalities. The two detector heads are positioned in each side of the breast, and the projection data can be acquired at different angular positions.

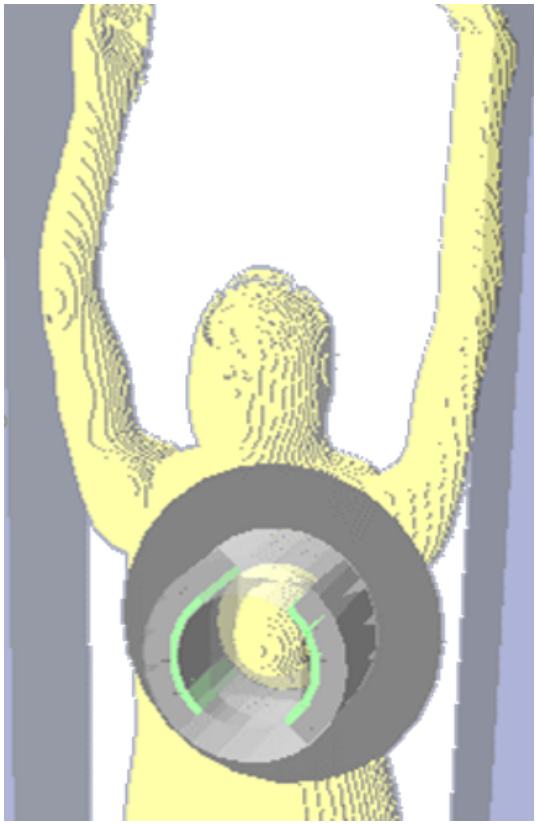

Figure 2.3: Example of how the SiPM-based PET-ToF demonstrator prototype can be adapted to breast cancer imaging.

The PET ring comprises 18 compact Detector Modules, where each module integrates 128 gamma-ray detection pixels of 3.1x3.1x15 mm^3 LYSO crystals coupled to MPPC photo sensors. The modules have two 64-channel readout TOFPET ASICs integrating signal amplification and discrimination circuitry and high performance TDCs for each channel, featuring 25 ps r.m.s. intrinsic resolution and fully digital output.

A data acquisition system comprises multiple frontend digital boards (FEB/D), each collecting the data of 1024 channels (8 Detector Modules) data frames through a serial link (3.2Gb/s), and a single DAQ board connected to the PCIe bus of the acquisition PC.

First performance results about energy resolution were done based on the Time-over-Threshold technique. In this methodology the expected curve is nonlinear which is described in [14]. Thus, an internal circuitry was used to obtain the ToT curve as function of the deposited charge and, after that, to check the linearity of the energy scale in different channels, discrete radiation sources (Ge-68 source) were used to plot the nominal versus the measured energy. Based on that, a resolution of 24.5% FWHM at 511 keV over all the channels was obtained. All obtained results, the associated methodology and more detailed characteristics about the SiPM-based PET-TOF demonstrator prototype are described in [14].

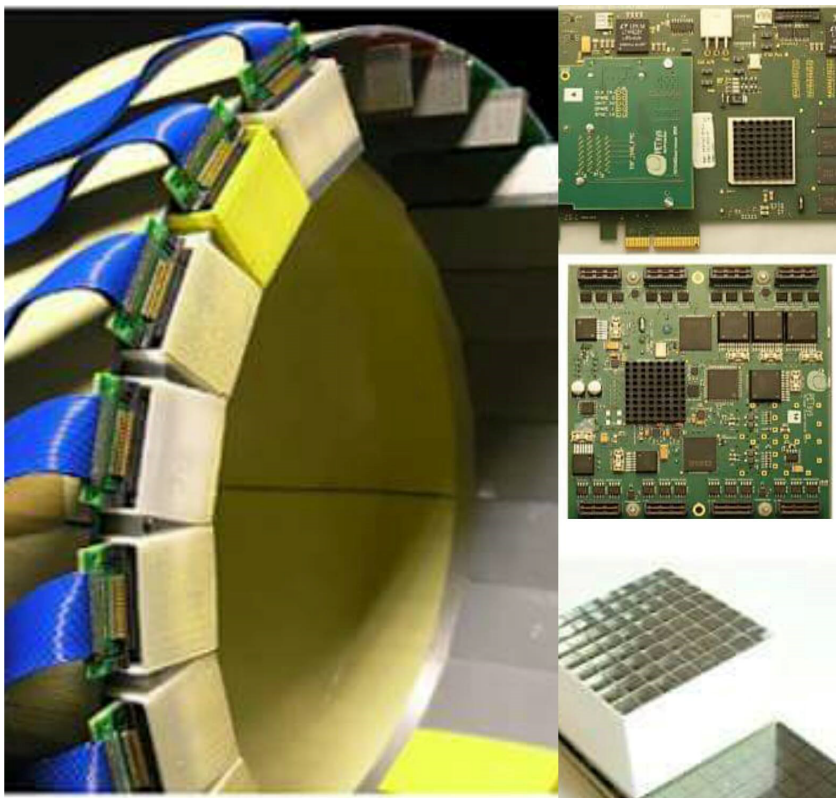

Figure 2.4: A) SiPM-based PET-ToF demonstrator prototype. B) DAQ Board is a PCIe data acquisition board that collects data from the fronted FEB/D boards. C) Front End Board Type D (FEB/D) reads the data from eight FEB/A boards. D) Detector module that consists of 2 matrices of 64 LYSO crystals each coupled on one end to a SiPM MPPC array, assembled on a compact front end board (FEB/A). On the back side of the FEB/A lies the front end electronics with two TOFASICSs to form a Detector Module (DM) [14].

2.4 Image Reconstruction Techniques

One of the image reconstruction problems present in Nuclear Medicine can be expressed as transforming signals measured by the electronics composing the detector into a 3D representation with clinical interest of the emitted radiation. To consider the whole set of all LORs shows the region with increased radiopharmaceutical uptake, is required to assume that each count on a line of response joining two detectors in coincidence directly represents the possible positions of annihilation and the number of counts is directly proportional to the activity along that line.

In the absence of physical effects such as attenuation, scattered and random coincidences, the activity is proportional to the total number of detected coincidences events between two scintillator detectors. The image reconstruction process involves solving the following equation:

$$p = Af + q \tag{2.3}$$

Where p represents the projections of the unknown object, A is the assumed detection model for the system, f is the estimated image after reconstruction and q=r+s is the error

associated to the observation that accounts for the presence of random, r, and scattered, s, coincidence events [13]. Commonly, the approach to deal with this problem is to assume that measured data has a deterministic character containing no statistical noise. Thus, the value of q in Equation 2.3 is known without uncertainty and an exact solution for the image can potentially be found.

Filtered Back Projection (FBP), based on the Central Slice Theorem, is the simplest and most widely used analytic method [15,16] This theorem states that a one dimensional (1D) Fourier transform of a projection is equal to the two dimensional (2D) Fourier transform of the slice to be reconstructed. The basic principle is to perform the Fourier transform of angular projections and apply a "ramp filter" in the frequency domain to enhance high spatial frequencies and suppress low ones, before the inverse Fourier transform or back projection being performed [15]. Although FBP is fast and images can be obtained within short reconstruction times, it requires data corrections either before or after the reconstruction. This generally results in images with limited quality. Nevertheless, FBP is usually available in the commercial imaging systems and it is still considered adequate for clinical procedures that do not require image quantification.

In fact, the acquired data have an intrinsically stochastic nature inherent to the radiation detection process: radioactive decay; the presence of random and scattered events (q in Equation 2.3); as well as attenuation effects in the medium. Assuming this more realistic approach, which means to presume a statistical model for the data, makes an exact solution for the image formation not achievable. In such cases, the problem is called ill-posed. However, it is feasible to obtain approximate solutions, close enough to the original activity distribution to be of diagnostic value in the clinical practice. The problem is solved by estimation methods that successively iterate an image estimate of the original emission object. Convergence method starts from an initial guess of the object, usually a blank or uniform image, which is forward projected by a mathematical operator that accounts for the major characteristics of the imaging process. The resulting projections are then compared to the acquired data from the object and the difference between them is used to update the guess solution before new projections are generated. Iteration process is continued until the image estimate is considered, by some statistical criterion, to be a close representation of the true image. The image reconstruction methods that follows this approach are called iterative algorithms [16]. Due to more realistic description of the imaging process, this type of algorithms offers improvements over analytical ones in terms of image quality, presenting less artifacts, lower noise levels (although the noise increases with the number of iterations), enhanced signal detectability and consequently a more accurate quantification capability [17].

The added complexity also brings some limitations for the routine application of iterative methods such as, a slow convergence to a stable solution associated to the requirement of high performance computing facilities. Advances in computational speed have contributed to overcome this problem, which has allowed to increase the acceptance of these methods in the clinical environment. Several iterative algorithms have been developed for tomographic reconstruction: Algebraic Reconstruction Technique (ART) [18], Simulta-

neous Iterative Reconstruction Technique (SIRT) and Maximum Likelihood-Expectation Maximization (ML-EM) [19], among other [16]. Presently, the method available in most commercial emission tomographic systems is an accelerated version of ML-EM, what is commonly understood as the Ordered Subset Expectation Maximization (OS-EM) algorithm.

2.5 State of Art - TOF in PET imaging

2.5.1 TOF Basic Principles

As in most imaging modalities, statistical noise and image resolution limits PET imaging. The physical size of the detector element usually plays the dominant role in determining resolution, but the combined contributions from a collinearity, positron range, penetration into the detector ring, and decoding errors in the detector modules often combine to be of similar size. In addition, the sampling geometry and statistical noise further degrade the effective resolution. An effect that can be controlled is the size of the detector. If events are always assigned to the correct detector (which is not always the case), smaller detectors yield improved spatial resolution. Several factors have limited the miniaturization of PET detector crystals. An important factor is that it is not feasible to couple each crystal to its own photomultiplier tube, if the crystals are small and numerous [22]. Numerous studies have been performed in order to understand the ideal characteristics of a PET system and great improvements have been experienced.

Another way to improve image quality in PET imaging can be achieved by accurately measuring the arrival time of the two 511 keV positron annihilation photons in the ring of detectors that surrounds the patient, the location of the positron annihilation can be constrained. While this constraint is not tight enough to improve the spatial resolution, it can significantly reduce the statistical noise in the reconstructed images. This technique is known as time-of-flight (TOF) [25].

In PET imaging, coincident LORs are normally detected and recorded at many angles, and tomographic images are generated through traditional filtered-back-projection or iterative reconstruction in order to generate 3D images. Using TOF, the difference in arrival times between the 2 coincident photons is also measured for each annihilation event. Supposedly, as the location of each annihilation event can be identified on the basis of photon arrival time difference information within each LOR, with perfect (i.e. infinitely small) TOF information, image reconstruction would be unnecessary. However, even imperfect timing information helps to improve the reconstruction because TOF information serves to better localize the coincidence, which reduces the propagation of noise along the LOR [23] during image reconstruction.

The distance that a given event is projected along the LOR can be defined by an uncertainty Δx and the diameter of the patient (or phantom) as a distance D. With good time resolution, Δx can be much smaller than the distance D over which counts would be distributed equally in the forward- and back-projection steps of non-TOF reconstruction. A reduction of noise can be equated to an increase in sensitivity, and this effective sensi-

tivity gain was estimated [24] at the centre of a uniform distribution to be proportional to $D/\Delta x$ and

$$\Delta x = \frac{c\Delta t}{2} \tag{2.4}$$

Where c is the speed of light, and Δt is the timing resolution (full width at half maximum [FWHM]). Based on this, fixing a diameter D of a phantom with a uniform distribution, it's possible to accomplish a bigger sensitivity gain with smaller values of time resolution. These metrics argue that TOF gain increases not only as timing resolution improves but also as the object diameter increases, so we can predict the relative benefit of TOF as the patient size increases. However, it may be too simplistic to characterize the TOF gain as a single value, as we expect it to depend on both the task and methods of data correction and the image reconstruction.

The simple estimates of TOF gain, which were derived for analytic reconstruction and may not extend directly to iterative reconstruction, also do not consider the issue of faster convergence for an iterative reconstruction algorithm with TOF, an additional benefit of TOF that was shown [27] to depend on both the timing resolution and the statistics.

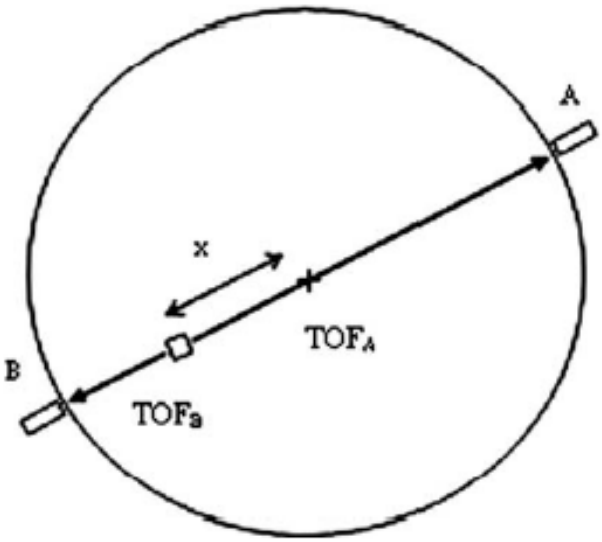

Figure 2.5: TOF PET scanner geometrical model. A photon pair is generated in the position indicated by the square pixel at x position from the centre. Two detectors A and B are selected in the detector ring. TOFA is proportional to the distance between the source and detector A, TOFB is proportional to the distance between the source and detector B. [26]

2.5.2 TOF History

The idea of using time of flight (TOF) information was recognized from the very early days (1960s) of PET in order to improve the knowledge of the location of the emission point along a LOR [28-30]. However, it was just on the early 1980s that the first generation of TOF PET scanners was developed for clinical use [31-36]. Initially, cardiology and brain imaging were the main areas for the application of PET systems. Hence, the motivation

for developing TOF PET was driven by the need to improve SNR in reconstructed images and reduce random coincidences in the collected data. This first generation of TOF PET scanners was based on CsF and BaF2 scintillators [37-39] and had a system coincidence timing resolution in the range of 450-750 ps [39-41]. Which means that the coincidence system considers the occurrence of a coincidence event when two particles reaches the detector within the defined timing resolution of the system. Also, poor spatial resolution and sensitivity were reached due to low density, low photoelectric fraction and low light output. Furthermore, the use of more expensive photomultipliers (PMT) with quartz window was needed since the ultraviolet emission of BaF2 made light collection difficult.

Comparatively, the non-TOF PET systems using slower scintillators such as bismuth germanium oxide (BGO) and NaI(TI) [42] reached high detection efficiency, acceptable light output, and a light emission wavelength of around 480mm. In this way, BGO became the standard in PET, but was unable to be used for TOF PET due to its low light output and long decay time of 300 ns.

A new phase of TOF PET research appeared in the 1990s with the discovery of new scintillators. LSO (Lu2SiO5) become frequently used in PET detectors since has a relatively high light yield, high effective Z, high density and a short decay time (see table **??**table21). This last characteristic was immediately used to reduce the coincidence window from the 12 ns typical of BGO scanners to 6 ns and it was later reduced to 4.5 ns using faster electronics. Based on this, the random coincidences in the acquired data became lower. Furthermore, a value of 300 ps for time resolution has been reported with two single LSO crystals in coincidence, which makes TOF PET a viable solution [43]. First attempts to perform TOF reconstruction on a commercial LSO PET scanner showed a measurable gain in signal-to-noise ratio (SNR) due to the TOF reconstruction [44,45] even with a poor 1.2 ns time resolution.

Table 2.1: Examples of scintillators and their properties. Compiled from [22, 20].

	NaI	**BaF_2**	**BGO**	**LSO**	**GSO**
Effective atomic number (Z)	51	54	74	66	59
Linear Attenuation coef. ($cm^{-}1$)	0.34	0.44	0.92	0.87	0.62
Light yield [%Na:TI]	100	5	15	75	41
Peak wavelength (nm)	410	220	480	420	430
Decay constant (ns)	230	0.8	300	40	456

More recently, a cerium-doped lanthanum bromide (LaBr3) has been investigated as a candidate for TOF PET since it has a lower decay time (16 ns), excellent energy resolution (typical energy resolution at 662 keV is 3% as compared to sodium iodide detectors at 7%) and twice as much light output than LSO, although it has a lower stopping power (density of 5.08 g/cm) [46]. The first TOF scanner developed with these crystals showed a 460 ps time resolution value, which was improved to 420 ps and there is evidence that time resolution could be brought down to 315-330 ps [47]. In 2006, Philips has introduced the first commercial time-of-flight PET scanner (Gemini TF PET/CT) which uses a LYSO scintillator crystal [27].The LYSO structure is very similar to that of the LSO, but here a fraction of the lutetium atoms in the crystal are replaced by yttrium. Not just the

structure, but also the physical properties are very similar to those of LSO, the main difference is due to yttrium lower weight which confers a lower density to the LYSO crystal when compared to LSO. Time resolution achieved with this scanner was about 585 ps if measured with a low activity source. Other clinical results from Siemens prototype scanner have been published and showed a time resolution of 550 ps [49]. Also, all biggest commercial manufacturers have introduced some version of an LSO- or LYSO-based TOF PET scanner system with timing resolution in the 450- to 560-ps range, the mCT time-of-flight PET/CT scanner from Siemens and the hybrid PET/CT Discovery-690 [50].

None of these new TOF PET scanner systems compromise system sensitivity or spatial resolution. In fact, the non-TOF performance of these scanners is the highest that has been achieved historically [23]. Also, due to having a good system energy resolution and the ability to correct and reconstruct large datasets because of advances in computer hardware, the current TOF scanners operate in fully 3D mode, which wasn't allowed in the older systems. Other advantages of the new systems are rely on the use of new small cost-effective PMTs with good timing performance. Moreover, progress in electronics with new application specific integrated circuits (ASIC's) and field-programmable gate array (FPGA's) designs have led to a more stable timing performance.

Lastly, is important to refer that the image reconstruction techniques have seen several significant developments since the beginning of TOF-PET systems. In the 1980s, predominantly analytic algorithms were used for image reconstruction, the most well known in literature are the most-likely-position [24] and the confidence-weighted (CW) backward projection [24, 37, 43]. In recent years, there have been significant developments in iterative list-mode reconstruction algorithms, with full system modelling (including TOF kernel) included in the reconstruction [44,47]. In combination with faster central processing units and parallelization of reconstruction algorithms, these techniques have become practical and feasible for clinical use.

Although TOF PET technology has suffered a lot of improvements due to all these technical advances which made it a necessary component of all modern PET scanners, the growth of 18F-FDG PET imaging in oncology is now the primary driver for most advances in PET technology.

2.5.3 TOF Gain Estimation

The TOF reconstruction reduces the noise propagation along the LOR during back projection of the data in the reconstruction process. The main factors that influence this reduction are the width of the kernel used and the time resolution of the system. In the early years, this noise reduction was studied mainly via modelling the noise propagation through analytical reconstructions processes in TOF and non-reconstruction [26]. Strother et al. using an analytical back-projection algorithm modelled in a simple case the conventional non-TOF signal-to-noise ratio (SNR) [54]. Considering a cylinder with uniform distribution of activity and a diameter D, one can estimate the SNR in an image element of size d starting from the data collected in the projection space.

$$SNR = const.n^{-1/2}[\frac{T^2}{(T+S+T)}]^2 \tag{2.5}$$

Where n represents the number of volume elements influencing the noise in such image element, T represents the total trues in the image and R the random coincidences.

For conventional non-TOF PET all volume elements that contain activity along the same LOR contribute to the same projection data. In reconstruction, it's not only considered the image element where the event was originated, each detected event is back-projected in all image elements along the LOR. Consequently, all n elements contribute to the noise in each image element and n can be easily estimated as $_{conv} = D/d$(figure 2.6a).

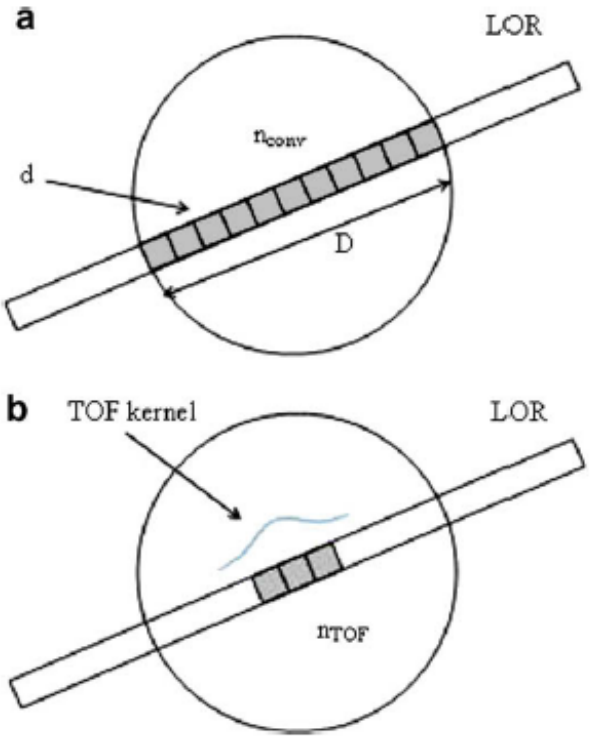

Figure 2.6: (a) In non-TOF reconstruction, all volume elements n found in the object along the line of response contribute to the noise in each image element, and $n_{conv} = D/d$. (b) In TOF reconstruction, because of the better localization of each event along the LOR, only the volume elements n adjacent to the position identified by the measured TOF contribute to the local noise, and $n_{TOF} = \Delta x/d$. The time resolution Dt limits the number of elements contributing to the noise, since it determines the localization uncertainty Δx. [26]

Otherwise, when TOF information is implemented, each event is TOF tagged. With this additional information in the reconstruction process, each event is back-projected only in the position associated to such TOF information and into few volume elements adjacent to it. The contribution weight of each volume is defined by a TOF kernel or probability function of width Δx. So Δx is the localization uncertainty, related to the time resolution Δt in the Equation 2.4. In this case, n is estimated as $n_{TOF} = \Delta x/d$(Figure 2.6b).

In this way, it's possible to obtain an estimate of the signal-to-noise ratio introduced

by TOF reconstruction if the appropriate values of n were used in Equation 2.5. The Equation 2.6 describes this estimation and it's used as measure of the TOF SNR gain in the literature.

$$SNR_{TOF} = \sqrt{\frac{D}{\Delta x}} SNR_{non-TOF} \tag{2.6}$$

Some modifications to this formula and other slightly different values were estimated by different researchers, but Equation 2.6 is still a reasonable estimate of TOF gain in analytical reconstruction [10]. However, this analysis can't be done when iterative reconstruction is considered. This is caused by the nonlinearity of this kind of the reconstruction and the complication added by the arbitrary choice of the iteration number. Using iterative reconstruction method, Equation 2.6 can roughly estimate the SNR gain between a non-TOF and a TOF image. This is due to the TOF has faster convergence, so reached similar contrast recovery but at different iteration number [26].

It is possible to define the noise equivalent count rate (NEC) as a measure of the detected counts corrected for the noise contribution of scatter and random coincidences. Alternatively, the NEC can also be taken as a measure of the effective sensitivity of the PET scanner. The NEC correspond to the quantity $T^2/(T+S+R)$ from Equation 2.5 and can be expressed as the square of the SNR. Consequently, the SNR gain can be seen as NEC gain or sensitivity gain. Derived from Equation 2.5 and 2.6, it's possible to define Equation 2.7 where TOF reconstruction is equivalent to an amplification of the PET scanner sensitivity.

$$NEC_{TOF} = \frac{D}{\Delta x} NEC_{non-TOF} \tag{2.7}$$

Based on Equation 2.7 it is possible to claim that the NEC gain is directly proportional to the size of the patient and inversely proportional to the time resolution of the PET scanner, which means that larger patients will benefit from TOF reconstruction. Also, for reach a better performance of the TOF PET scanner is essential improve time resolution. To finish, given a patient size equivalent to a 40cm diameter cylinder, the estimated TOF NEC gain is reported as function of the time resolution in Table 2.2. Based on results it's possible to assert the potential of TOF reconstruction as a "sensitivity amplifier" [26].

Table 2.2: Time Resolution, spatial uncertainty and estimated TOF NEC gain for 40 cm diameter uniform cylinder [26].

Time Resolution (ns)	**Δx (cm)**	**TOF NEC Gain**
0.1	1.5	26.7
0.3	4.5	8.9
0.5	7.5	5.5
1.2	18.0	2.2

2.5.4 Benefits of TOF PET in the Clinics

Image Recontruction

In order to distinguish benign and malignant tumours and to determine disease progression during therapy, the lesion uptake measurement is commonly performed on F18-FDG images. Using iterative methods for image reconstruction brings the lesion uptake measurement closer to convergence, however per each additional iteration of the algorithm the noise in the image will increase. To understand better this behaviour, a lot of work has been done in this last decade using both clinical studies [56, 57] and physical phantoms [45, 27, 56-58]. So, it has been shown that with TOF imaging the lesion uptake or contrast recovery coefficient (CRC) converges more quickly or requires less iteration to achieve the maximal contrast. TOF and non-TOF images are showed in Figure 2.7a [56] and were reconstructed from the same dataset for a 35 cm diameter lesion phantom as a function of iteration number. Due to fast recovery of lesion uptake, we can easily see that after the first iteration the smallest hot sphere (10 mm in diameter) is clearly detectable. For non-TOF images, no similar result can be achieved even after 20 iterations of the algorithm. In addition, in the latter case, the noise in the image is significantly improved.

In Figure 2.7b [56] it's possible to see images containing TOF information after 5 iterations and non-TOF after 10 iterations, both as a function of varying scan times. The number of iterations was chosen based on the relative convergence of the 2 image sets, with very little increase in lesion uptake as the number of iterations increased. Based on the image, it's possible to observe that even after a 5-min scan the 10 mm sphere is not visible for the non-TOF image, while to see the 13 mm diameter sphere one need a scan time greater than 2 min. With TOF, all lesions are visible after a scan time of 2 min.

Lesion CRC is plotted as a function of image noise for 13-mm diameter sphere, which it's possible to see in figure 2.7c [56] and conclude that for the same scan time and noise, TOF leads to a higher CRC. For a similar CRC, the non-TOF image has higher noise, and increasing the scan time from 2 to 5 min still does not lead to a noise level similar to the 2 min TOF image, indicating the potential to reduce scan time with TOF imaging. These phantom studies indicate that in patients TOF imaging should lead to increased lesion uptake measurements, which is important because clinical studies are performed to achieve a certain fixed level of image noise for either TOF or non-TOF data [50].

To conclude this analysis, results from a 5-patient study showing the average gain in contrast due to TOF information for several lesions within each patient are presented in Figure 2.7d [56]. The TOF and non-TOF images were chosen for a fixed number of iterations over all patients that gave a similar pixel-to-pixel noise within the liver. It's possible to conclude, similarly to the case of phantom studies, that TOF leads to a gain in lesion contrast measurement with a trend towards higher gains in larger patients. Other studies have been done in order to study the benefit of TOF information in image reconstruction. These studies demonstrated improved lesion detection and quantitative performance for routine clinical 18F-FDG imaging tasks allowing shorter imaging times and more uniform imaging performance over varying patient habitus [24]. In smaller patients, although the

benefit of TOF information may not be significant, one could consider using shorter scan times to achieve images with similar quality.

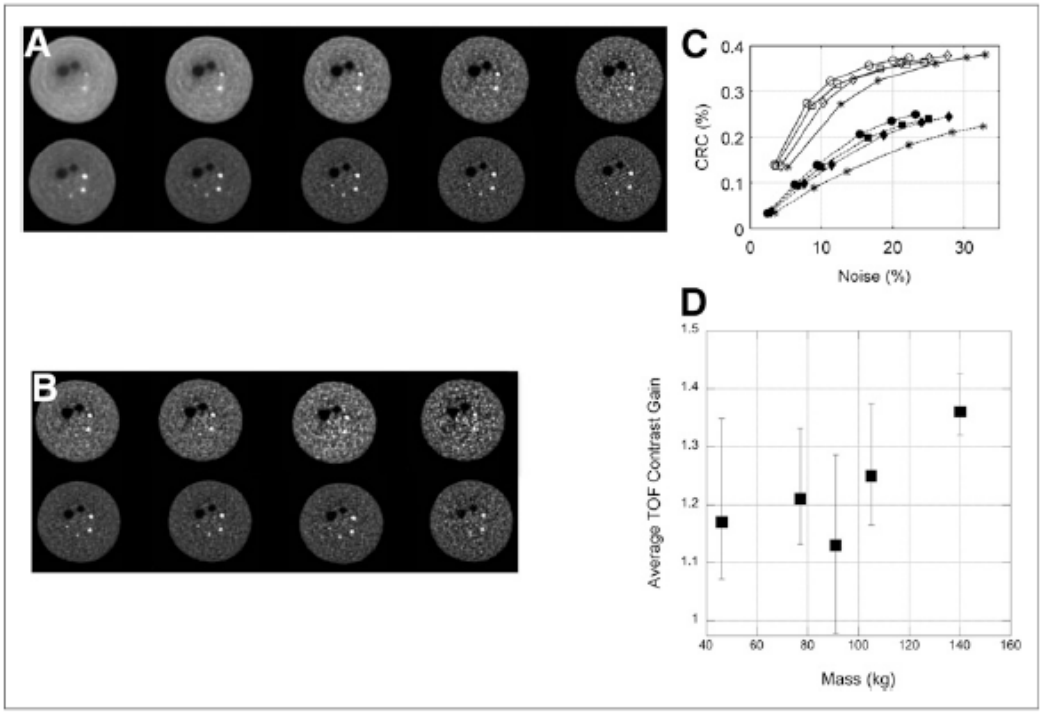

Figure 2.7: (A) Reconstructed non-TOF (top row) and TOF (bottom row) images for 35 cm diameter cylindrical lesion phantom for iteration numbers (left to right) 1, 2, 5, 10, and 20. Phantom has hot spheres (diameters of 22, 17, 13, and 10 mm) with 6:1 uptake relative to background and 2 cold spheres (37 and 28 mm). (B) Non-TOF (top row) and TOF (bottom row) images for 35 cm diameter cylindrical lesion phantom for scan times of (left to right) 5, 3, 2, and 1 min. Non-TOF and TOF images are shown for iterations 10 and 5, respectively, where lesion CRC values are at or close to convergence. (C) CRC for 13 mm diameter sphere plotted as function of image noise at iteration numbers 1, 2, 5, 10, 15, and 20. Closed symbols are for non-TOF and open symbols for TOF images with scan times of 2 (△), 3 (♦), 4 (■), and 5 (·) min. (D) Gain in lesion contrast as measured over several lesions in 5 different patients. TOF and non-TOF images were chosen for fixed number of iterations to achieve similar pixel to pixel noise in images. [24]

Partial Ring Detector

In recent years, dedicated partial ring PET devices have been developed for use in specific areas, especially in breast imaging. For this, a variety of detector configurations and scintillators are studied. The main objective of these developments is to achieve higher sensitivity than clinical PET scanners and reduce the attenuation of photons in comparison with what happens in whole-body PET imaging. The resolution of most of these dedicated scanners is in the range of 2-4 mm, with an emphasis on spatial resolution at the expense of sensitivity (resulting in the use of short crystals). Nevertheless, the detection of small tumours requires a fully 3D reconstructed tomographic image. This is not possible with any of the dedicated breast PET scanners proposed so far. The reason for this is the use of limited angle coverage of the imaging plane through a partial detector ring, leading to an incomplete sampling resulting in artefacts in image reconstruction [61].

Due to small object size, the use of TOF information in PET imaging will contribute limited quality gains in these partial ring devices. As a result, studies to investigate the performance of a limited angle, but TOF-capable, breast scanner to determine whether it is possible to achieve artefact-free tomographic images for detection and quantification of lesion in the breast.

In the present study done by Surti and Karp in 2008 [51] the impact of timing resolution in TOF as a function of angular coverage on achieving artefact-free images with high contrast recovery values for small, hot lesions, were investigate. Also, a simple SNR metric was used to study the trade-off in sensitivity achieved due to reduced partial angular coverage and improved timing resolution. The study was performed using Monte Carlo simulations for a breast scanner design. Image reconstruction was performed for three different ring geometries (Figure 2.8): a full scanner ring (complete 180 degree in-plane angular coverage), a two-third scanner ring (120 degree in-plane angular coverage) and a half scanner ring (90 degree in-plane angular coverage).

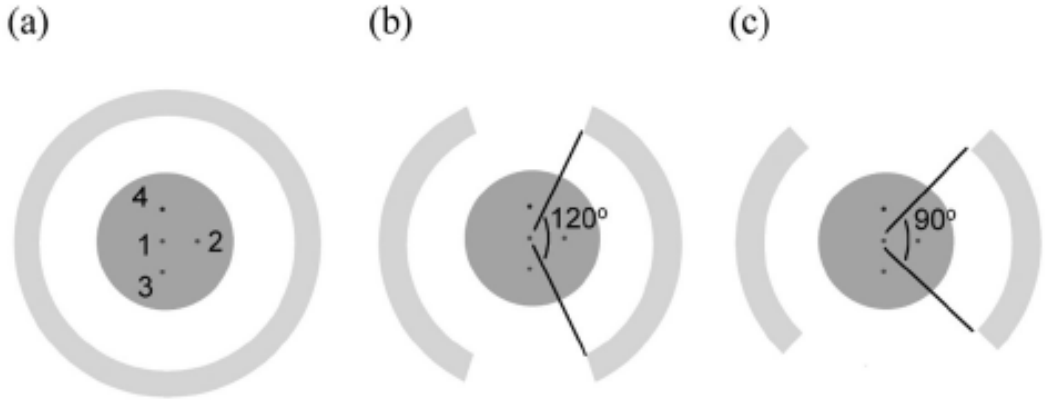

Figure 2.8: Design of the scanner for the (a) full ring, (b) 2/3 ring (120 degrees in-plane coverage), and (c) 1/2 ring (90 degrees in-plane coverage). In the middle of each scanner, a cylinder phantom was simulated containing three hot spheres and a cold sphere. [52]

These researchers showed that, without TOF information, the limited angle situation leads not only to distortions, but also to severe artefacts in the reconstructed image as the object size relative to the scanner ring diameter increases. Consequently, detector rotation needs to be employed to cover all the missing LORs, which however leads to longer scan times or essentially a reduction in effective sensitivity. By using TOF information, a lot of the distortions as well as non-uniform artefacts can be reduced without the need for detector rotation. However, as the angular coverage is reduced, better timing resolution is needed to produce artefact-free images. Furthermore, this study found that a timing resolution of 600 ps or better was needed for a 2/3 ring scanner (scanner ring diameter of 15 cm), while a timing resolution of 300 ps or better was necessary for the 1/2 ring scanner geometry, in order to achieve hot lesion CRC values similar to a full ring scanner. It was also showed that there is a gain in SNR with TOF information, since limited angle tomography leads to a reduction in sensitivity relative to a full ring scanner due to the

loss of counts in the missing LORs. These performances are possible to see in Figure 2.9.

Future Prespectives

Hereafter, TOF PET may play an important role in situations that require low-dose serial 18F-FDG imaging of patients and imaging with long-lived radioisotopes for targeted therapy. This is because these applications require low-noise images with reduced counts that are also quantitatively accurate, and TOF PET can provide significant advantages. The utilization of PET in these areas will benefit from ongoing instrumentation efforts to provide further improvements in system timing resolution, as well as more accurate data correction and image reconstruction algorithms.

Furthermore, the use of TOF PET imaging has an important application in the design of limited angle and application specific PET scanners. Since, can avoid the need for detector rotation to produce distortion and artefact-free images. This can have a significant impact in PEM scanners.

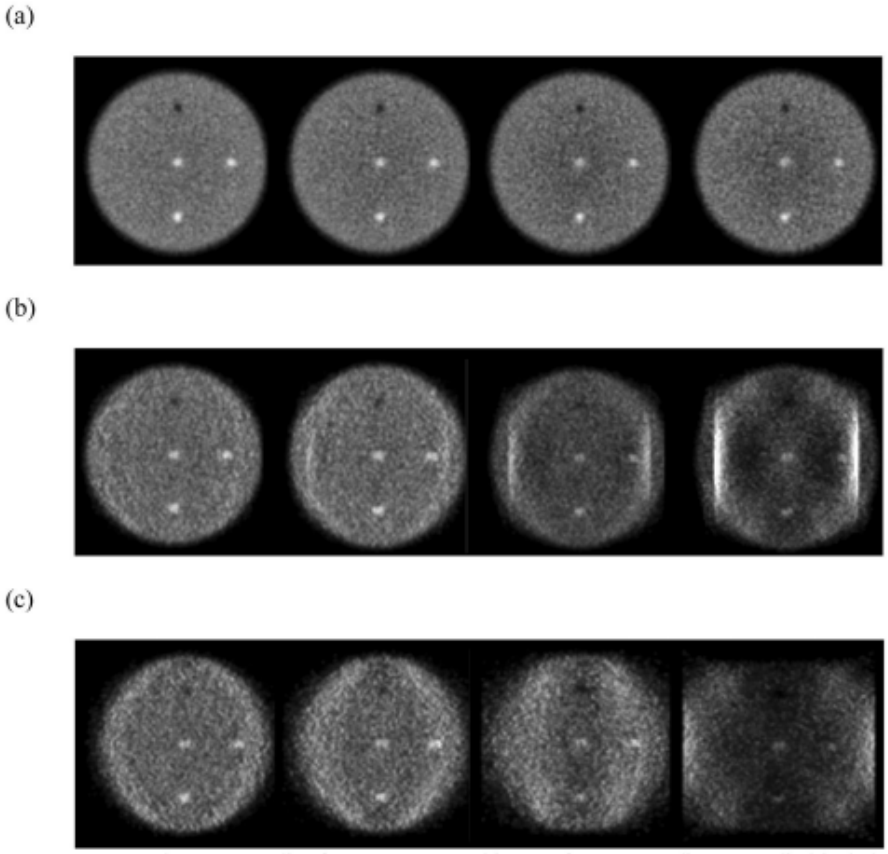

Figure 2.9: Reconstructed images for a cylindrical phantom in a (a) full ring, (b) 2/3 ring and (c) 1/2 ring scanner. With each set, the four images moving left to right are: 200ps TOF, 300ps TOF, 600ps TOF, and Non-TOF. [52]

Chapter 3

Materials and Methods

3.1 Monte Carlo Simulation – Detector Geometry

Monte Carlo simulation techniques have shown to be very useful predicting system's responses and solving problems in the medical physics context. These techniques are used with different purposes, here it will be used for image reconstruction and system validation. During the development of this project, Monte Carlo simulation were already used to model Clear-PEM system and predict its performance, to provide data for system validation of reconstruction algorithms [14] and to allow new system configuration and multimodality.

Based on these, in the work described here a Monte Carlo simulation tool was used to validate and simulate different normalization scenarios and to evaluate the benefit of adding time-of-flight algorithm in image reconstruction method. Simulated data were obtained using existing and open source software platforms. In this case a specific platform developed for medical applications, based on Geant4, GATE (Geant4 Application for Tomographic Emission) was used.

The Monte Carlo method was used also for scatter as it was in Clear-PEM project, since it is described as a high accuracy method. The basic principles of implementation were the same and it was done in C++.

Method implemented proceeds as follows [60]:

1. An input image depicting the objects' contour is provided to the algorithm;

2. A 511 keV photons pair is randomly generated inside the object;

3. The anti-parallel photons are transported through the medium and interactions (Compton Scatter and Photo-absorption) are modeled according to probability distributions;

4. Every Compton scatter interaction occurring along the photon's path is follow by the calculation, following know physical models, of the new direction and energy of the resulting photon;

5. If both photons reach the detector with energy above a pre-determined threshold, an event is recorded.

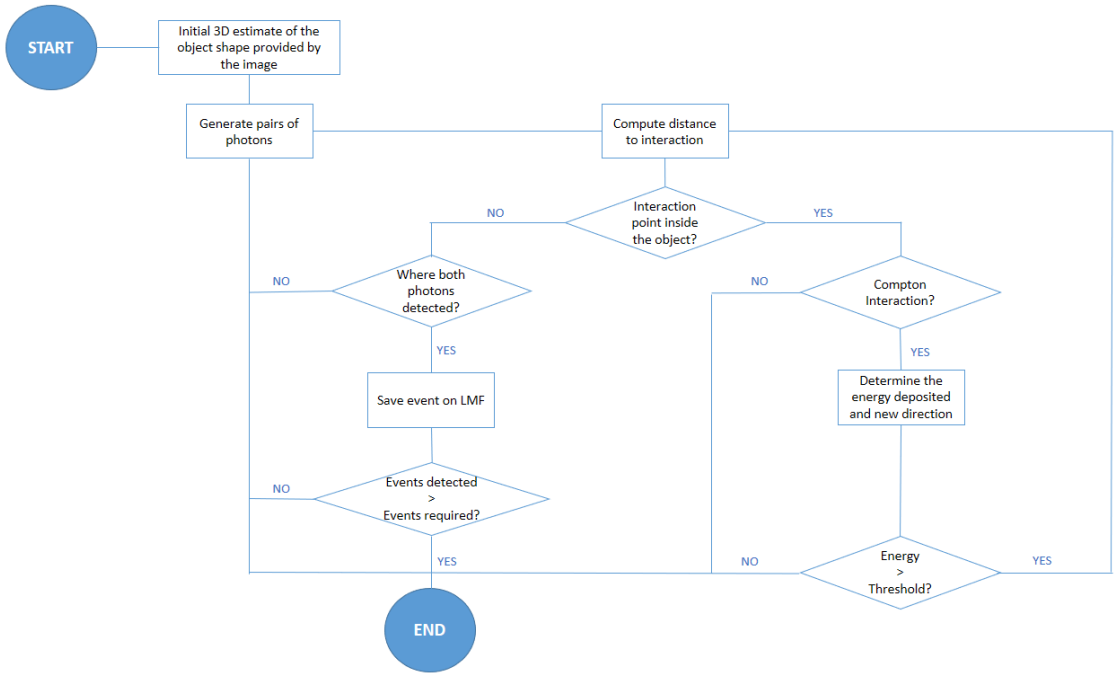

Figure 3.1: Representative diagram of the Monte Carlo method implemented from the beginning until the end of the process.

Since simulations using this tool are very time consuming due to their level of detail, for the purpose of validation, a small number of photons was simulated corresponding to approximately 1x10^3 detected events, for a detector head distance of 243.7 mm without rotation around the scanner axis. The analysis was performed using the ROOT toolkit, a data analysis framework developed at CERN. Generation, transport, interactions in the absorbing medium and detection energy resolution were assessed. The energy resolution implemented was 30% FWHM (Full With Half Maximum) accordingly to current value calculated from experimental data acquired for other studies performed in PETsys. More specific information of the simulated structure is presented above:

Detector module

- 4x4 array of LYSO (10% yittrium)
- Pixels of 3.06x3.06x15 mm^3 – 0.1 mm Vikuiti

Detector Head (15x15 cm^2

- 4x2 array of modules (15 mm pitch)
- Detector Heads distance: 243.7

Partial Ring Detector

- 8 Detector Heads x 2

Electronic chain

- Energy blurring 30%
- Energy window: 350 – 700 keV
- Time Resolution: 400 ps
- Coincidence chain Window: 2-10 ns

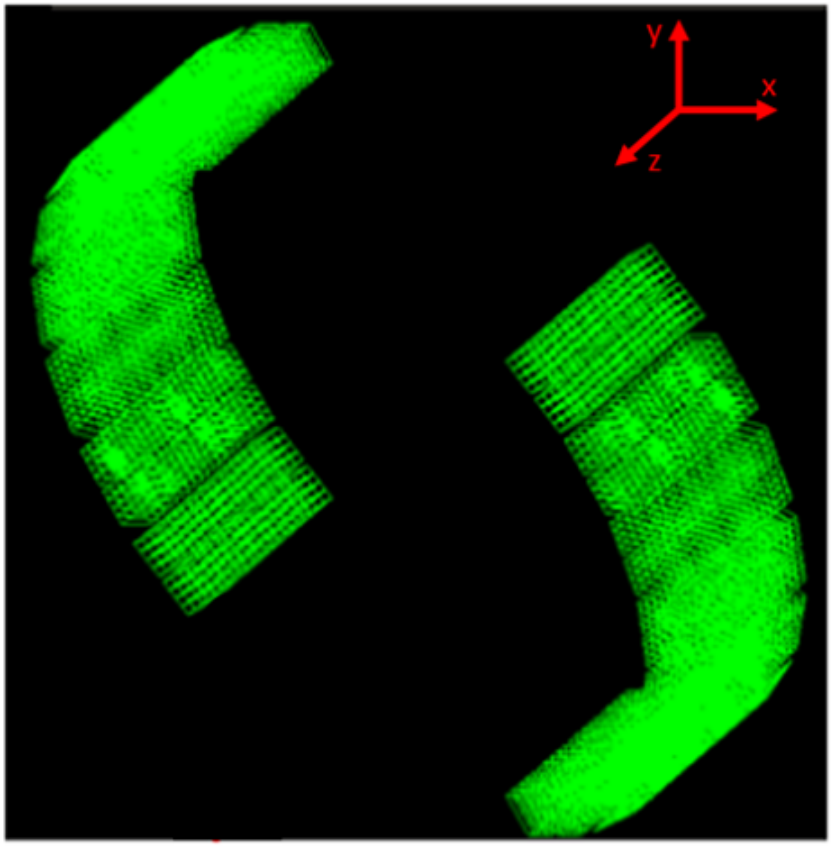

Figure 3.2: Simulation using GATE software of the SiPM-based PET-TOF demonstrator and the correspondent coordinate axis, which is used for the most of studies performed in this Thesis.

Based on this simulated detector, different types of sources with different shapes will be simulated using the GATE software to evaluate the method used for image reconstruction and also the benefit of introducing TOF algorithm the method.

3.1.1 Detector Geometry Validation

In order to validate the geometry and the acquired data for image reconstruction using GATE two different simulations were performed. The validation study compares experimental data with simulated one, both will be then reconstructed using the same code and obtained images will be compared. Also, this study will validate the adaptation made in the code for image reconstruction, since the method used was already developed for the Clear-PEM project and now adapted for the new detector configuration.

The first study will be performed using a point source of Na-22 with 1mm nominal diameter. The point source was placed in the centre of the detector and then data were acquired experimentally. By applying the same methodology, a Ge-68 line source with 1.5mm diameter and a length of 60mm was used. To compare and validate simulation data, the same sources and configuration for both cases were used in GATE simulations as is possible to see in Figure 3.3.

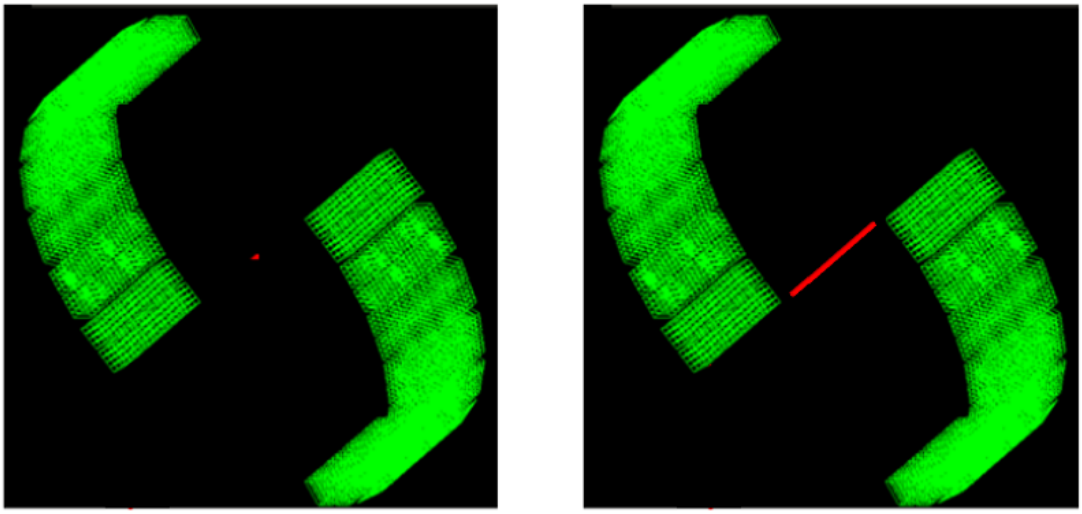

Figure 3.3: Simulation using GATE software of the SiPM-based PET-TOF demonstrator. A) Representation of the simulated Na-22 point source (red point). B) Representation of the simulated Ge-68 line source (red line).

It is important to highlight that this study was not used only for this purpose. Another of its purposes was the evaluation of the intrinsic spatial resolution of the demonstrator along the axial and the transaxial planes. Images were reconstructed based on the List-Mode reconstruction algorithm without TOF information that is described in 3.3. After finishing the reconstruction process, the images were evaluated using the AMIDE software using methods and metrics explained in 3.3.4.

3.1.2 Phantoms Simulation

During this work, several phantoms were designed and simulated in order to evaluate and better understand all the image reconstruction process. For all simulated data, Monte Carlo methodology used is based on a realistic and detailed description of the detector geometry. In this section of the work all the phantoms used for the different studies are described.

Cylinder

A simulation of a uniform cylindrical phantom with uniform activity distribution was performed. The phantom was placed in between detector heads, exactly in the centre,

with a radius of 50 mm, a length of 60 mm and an activity of 10 MBq (Figure 3.4). The simulated source was assumed to be uniform and with photon energies of 511 keV, also all data were acquired without rotation of the detector (only 1 angular position). This phantom is used in our studies in order to understand if it is possible to obtain a uniform and well defined shape when a considerable volume is used.

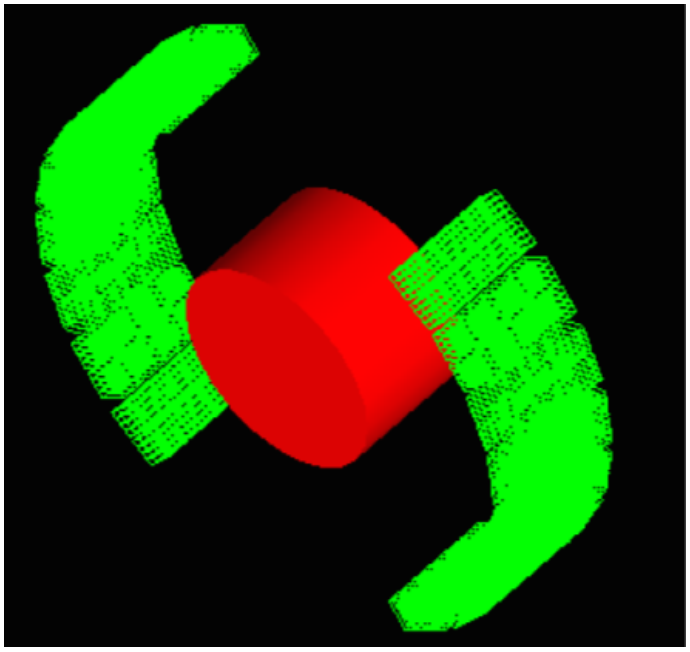

Figure 3.4: Simulation using GATE software of the SiPM-based PET-TOF demonstrator and a centred cylinder phantom with a radius of 50 mm.

Ring

The ring phantom was simulated with an inner radius of 45 and an outer radius of 50 mm, which matches to a thickness of 5 mm. The phantom was placed in between detector heads, exactly in the centre, and simulated with an activity of 10 MBq (Figure3.5). The simulated source was assumed to be uniform and with photon energies of 511 keV, also all data were acquired without rotation of the detector (only 1 angular position). The main objective of using a phantom with this shape and dimension is to evaluate the ability of the image reconstruction methodology for defining a thin shape when it is more farthest from the centre.

Point Sources

A cylinder full of water was simulated with a radius of 50 mm and a length of 60 mm. Inside of the cylinder six equal point sources with 1 mm diameter each were placed in the positions A - (0,0,0), B - (25,0,0), C - (50,0,0), D - (0,25,0), E - (0,50,0), F - (0,0,25) mm. All sources were assumed to be uniform and with photon energies of 511 keV, also the activity of each point source was defined as 7.5 Mbq. Figure 3.6 describes the configuration of this phantom. Data were acquired without rotation of the detector (only 1 angular position).

Figure 3.5: Simulation using GATE software of the SiPM-based PET-TOF demonstrator and a centred ring phantom with a radius of 50 mm.

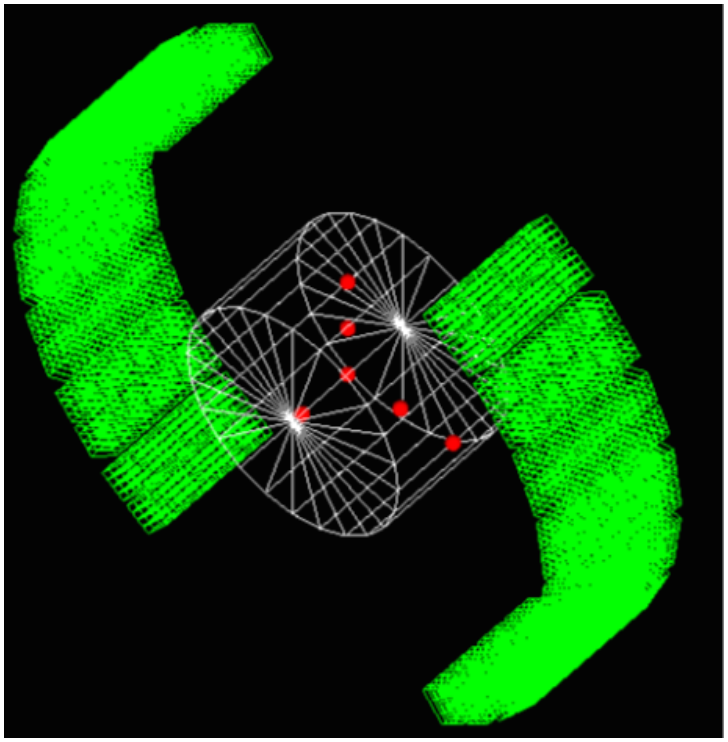

Figure 3.6: Simulation using GATE software of the SiPM-based PET-TOF demonstrator and a centred cylinder phantom with 6 point sources placed in the positions A - (0,0,0), B - (25,0,0), C - (50,0,0), D - (0,25,0), E - (0,50,0), F - (0,0,25) mm accordingly to the presented axis. All sources were assumed to be uniform and with photon energies of 511 keV.

Derenzo Phantom

A Derenzo Phantom composed by rods with radius of 1.25 mm, 1 mm, 0.75 mm, 0.675 mm and 0.5 mm. The overall dimension of the phantom was a cylinder with a length of 25 mm. The activity of each group of rods with the same dimensions were 12500 Bq, 10000 Bq, 7500 Bq, 6000 Bq and 5000 Bq, respectively. Also here, data were acquired without rotation of the detector (only 1 angular position) and the phantom was placed centred, in between detector heads. The phantom was assumed to be uniform with photon energies of 511 keV. In Figure 3.7 presented. So, the main objective of the simulation of a Derenzo phantom in this work is to understand how image reconstruction methodology can affect the capability of resolving the rods with different radius, i. e. to evaluate the intrinsic resolution of the system.

Figure 3.7: Draw of the Simulated Derenzo phantom for small animal PET. Derenzo phantom composed by rods with radius of 1.2 mm, 1 mm, 0.75 mm, 0.675 mm and 0.5 mm.

3.2 Amide Software

AMIDE is a Medical Image Data Examiner (AMIDE) that has been developed as a user-friendly, open-source software tool for displaying and analyzing multimodality volumetric medical images. Central to the package's abilities to simultaneously display multiple data sets (e.g., PET, CT, MRI) and regions of interest is the on-demand data reslicing implemented within the program. Data sets can be freely shifted, rotated, viewed, and analyzed with the program automatically handling interpolation as needed from the original data [53]. Based on this, AMIDE software was used during this project for image viewing and evaluation of different parameters.

In order to display the image, data already obtained from the image reconstruction method and placed in a .v file, need to be imported to the system. For our studies

data sets were loaded as it is demonstrated in Figure 3.9, here voxels were defined with a volume of 1 mm^3 and the dimensions were adjusted in order to match with the file size and, approximately, with the dimensions of the detector. For the purpose of this study, some specific tools of AMIDE were used for image evaluation. Line profile Tool was used to obtain Line profiles over each simulated image in different positions and directions. This tool allows FWHM evaluation which characterizes spatial resolution in PET imaging. Also, Regions of Interest were traced using ROI tool of AMIDE in order to evaluate quantitatively the displayed image.

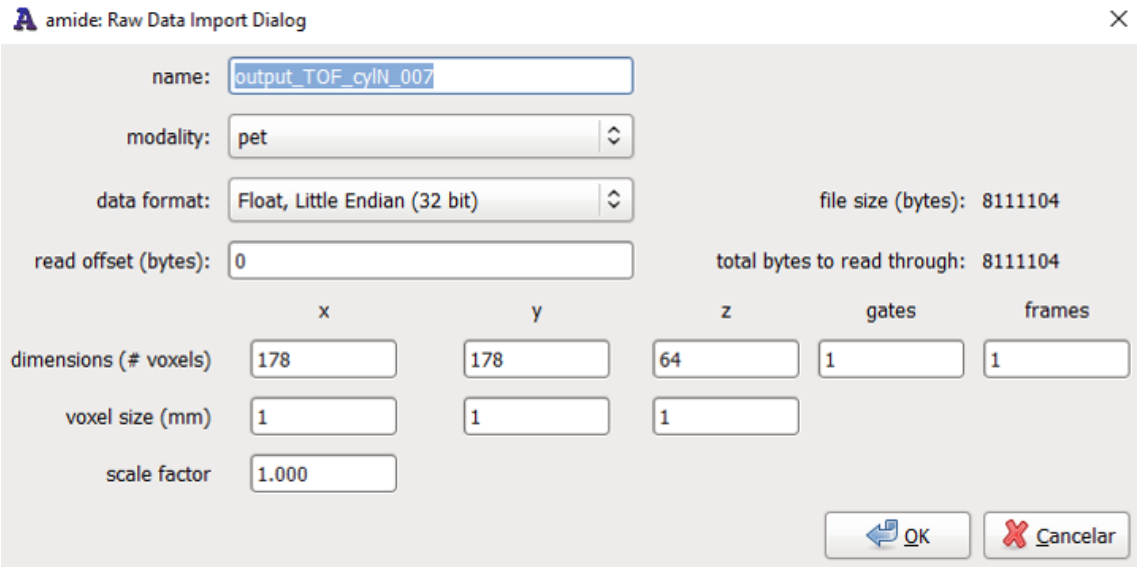

Figure 3.8: AMIDE's raw data import dialog used for data set loading and definition of dimensions.

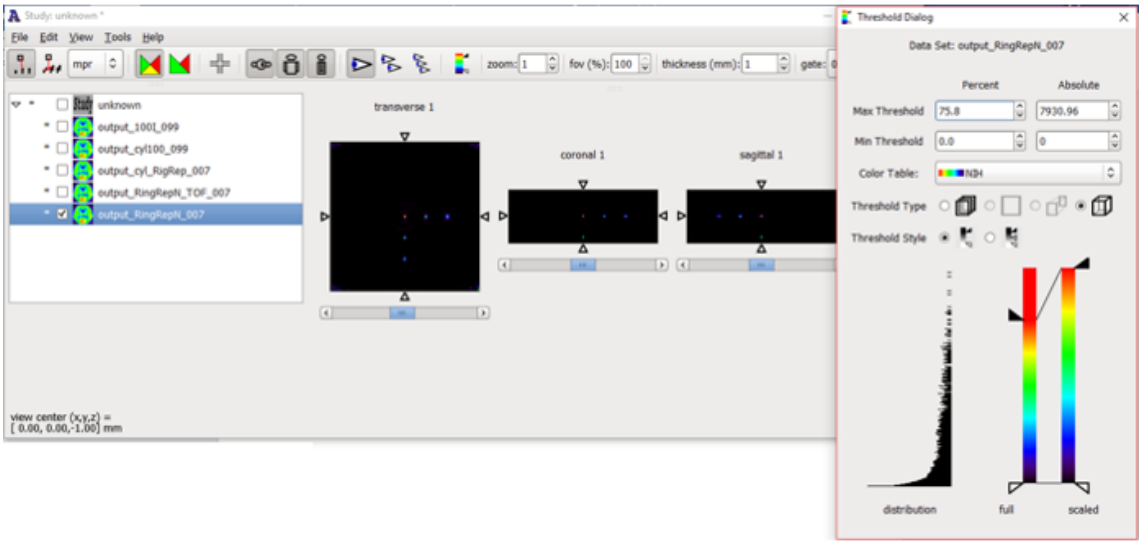

Figure 3.9: Main window of AMIDE shown in three cursor mode with aligned data sets loaded and displayed.

3.3 Image Reconstruction Methodology

The algorithm for image reconstruction used in this study was developed in the context of Clear-PEM project, and it was adapted and validate for the new detector characteristics. In Clear-PEM project, the development of 2D and 3D dedicated image reconstruction approaches were achieved and are comprehensively described in [7] for 2D reconstruction, in [10, 13] for 3D sinogram-based reconstruction and in [9] for 3D direct list-mode reconstruction (LM) methods. The work on data corrections and to integrate time-of-flight that will be done in this master's thesis project used the 3D reconstruction methods, so only these will be described in this report. Acquisition related details and data organization have to be taken into consideration, to successfully implement data corrections on the software. These and the main reconstruction algorithm chosen to reconstruct the data will be described in this section.

3.3.1 Data Acquisition and Organization

In this acquisition mode all the LORs defined by the combination between two crystals of opposite detector heads are accepted with no angular restrictions or compression procedures. The data acquired is presented by a N^2-1 segment formed by inter-ring crystal combinations, where N is the number of rings, contrasting with 2D acquisition mode machines where usually only coincidences detected by crystals of the same ring are considered. Several positions around the phantom are allowed, since a fully 3D tomographic scanner is used, which increases angular sampling and statistics.

In PET imaging, there exist two most used methods for data organization. The most straightforward is to store the information of each event (e.g. detection position of both photons in opposite crystals, energy, time information) in a list for posterior direct reconstruction in an event-by-event basis. This approach can result in long reconstruction times for high statistics data sets, thus is considered to be appropriate for low counts acquisitions where frequently some of the possible LORs will not register a single event.

The other method for data organization is to histogram the acquired data in a sinogram format. Events are sorted, for 3D acquisitions, by the distance of the LOR joining two detector elements to the axial axis of the scanner (s), the azimuthal angle (φ) that defines the projection angle, axial coordinate (z) and segment (δ). The combination of a sinogram bin, a given segment and an axial coordinate (2D slice of the object) represent each LOR, based on this a sinogram will group in each column LORs with the same distance to the axial axis and in a row LORs with the same azimuthal angle. In a sinogram, each LOR is described according to s and φ and a set of parallel LORs for a fixed φ is called projection.

Both list-mode and sinogram methods for data organization are available for the reconstruction tools developed for our system. The sorting process of the data into sinograms is performed offline and has input the list-mode file obtained at the end of an acquisition, also used for list-mode reconstruction.

3.3.2 Reconstruction Algorithms: MLEM and OSEM

After the acquisition of the data and based on the photon pairs detected, a whole new process starts in order to obtain a representation of the activity distribution. Assuming perfect conditions, the coincidences saved describe LORs along which the annihilation occurred, therefore representing the tracer distribution. The stochastic nature underlying radiation detection dictates, however, that a few more effects are considered to precisely describe the acquired data. The reconstruction process has to take into account the sensitivity of the system A and the contribution q of known physical effects, as random and scattered coincidences. Thus, considering an object with a given activity distribution, f, the reconstruction process objective is to obtain an estimate of this distribution from the measured projection data p, which can be described with the following equation:

$$P = Af + q \tag{3.1}$$

Here, A is a matrix where each element (a_{ij}) represents the probability that an emission from a discrete volume section j called voxel is detected by the crystal pair i. This is commonly referred as system matrix and it's a detection model of the system. A simplified version of this problem is commonly used and it's based on an analytical approach that is called Filtered Back Projection (FBP). This algorithm is based on the inversion of the Radon transform [70]. Analytical algorithms assume a continuous sampling of the object and the lack of physical effects, as scatter and random events. Moreover, assumption of absence of statistical noise allows to achieve an exact solution. All these simplifying limit the accuracy of analytical methods, since the model used does not reflect the real situation [70]. Nevertheless, FBP still an algorithm available as part of reconstruction software platforms of several imaging scanners, since it allows to obtain compute images in a very short period of time.

More complex statistical reconstruction techniques are needed to achieve an accurate description of the acquisition data. These should take into account probabilistic models of the noise, a realistic model of the physical effects and the acquisition of the data as a set of discrete measurements. In this case, there is no exact solution for the reconstruction problem and an approximation to the real activity distribution is done using an iterative scheme. It will progressively refine the estimates until reaches an acceptable agreement between estimated image and measured data.

To accomplish a more realistic approach it's associated a slow convergence to a solution due to the computational burden, which retained the use of iterative techniques clinically. Nevertheless, due to constant developments in electronics and computer power in the early years, iterative algorithms have been increasingly preferred in clinical practice. Five principal components are incorporated in iterative reconstruction algorithms which are finite parametrization, data model, system matrix, objective function and optimization algorithm. The last two components represent the reconstruction algorithm signature, since the system matrix and the image parametrization can be common to different algorithms. The objective function used in our reconstruction algorithm is the maximum-likelihood

(ML), firstly proposed by [11]. A known problem of ML methods is that the image solution tends to be noisy if the data is noisy too. Furthermore, is well known that the noise will increase during the iterative process (after each iteration) and the final solution provided by the ML maximization may be too noisy and not correspond to the optimum image. There exist some approaches to deal with increasing noise, as to smooth the images by filtering the highest frequencies.

The ML solution is finally obtained using a numerical algorithm that optimizes the objective function, as the expectation maximization (EM) algorithm [12]. This method provides estimates that iteratively approach the solution that satisfies the optimization of the objective function. These components together give rise to the Maximum-Likelihood Expectation Maximization (MLEM) reconstruction algorithms firstly proposed by Shepp and Vardi [19]. This algorithm is mathematically described with the follow equation:

$$f_j^{n+1} = \frac{f_n^j}{\sum_i a_{ij}} \sum_i \frac{a_{ij} p_i}{\sum_k a_{ik} f_k^n} \tag{3.2}$$

The operator that projects the image estimate into the projection space is called forward-projector operator and is defined with $\sum_k a_{ik} f_k^n$. While $\sum_i \frac{a_{ij} p_i}{\sum_k a_{ik} f_k^n}$ represents a back-projection in an inverse operation from the estimated projection errors, given by the comparison $\frac{p_i}{\sum_k a_{ik} f_k^n}$, into the image domain. The algorithm initiates from an initial estimate of the activity distribution, which is usually uniform, and then enters a loop of forward- and back-projections calculations until it reaches the maximum likelihood criterion or satisfies the stopping rule. Therefore, the current solution is updated in each iteration N based on the calculated error between measured and estimated projections. The procedures of the iterative reconstruction are presented in Figure 3.10.

An accelerated version of the MLEM algorithm was proposed by Hudson and Larkin in 1994 [15]. Ordered-Subsets Expectation-Maximization (OSEM) is the name of this algorithm and it's the approach most used to reconstruct our data. OSEM algorithm differs from the MLEM algorithm by grouping the projection data into subsets and creating sub-iterations where, instead of the whole projection data, only the selected sets are used to obtain an image estimate. The algorithm proceeds to a new iteration step after processing all subsets. This procedure is able to accelerate convergence by a factor proportional to the number of subsets [15], without compromising the quality of the reconstruction. It is important to highlight that a high number of subsets comprising less information each, will adversely increase the statistical noise in each estimate and in the final image.

The System Matrix

The system matrix is one of the main components of iterative algorithms and can incorporate a set of physical effects and the way of calculating it is not limited to one single option. This matrix can be used to model several aspects of the acquisition such as geometrical factors (g_{ij}), determining the probability of an emission from voxel j being detect by the detector pair i due to geometric constrains, the efficiency (d_i) of the pair of

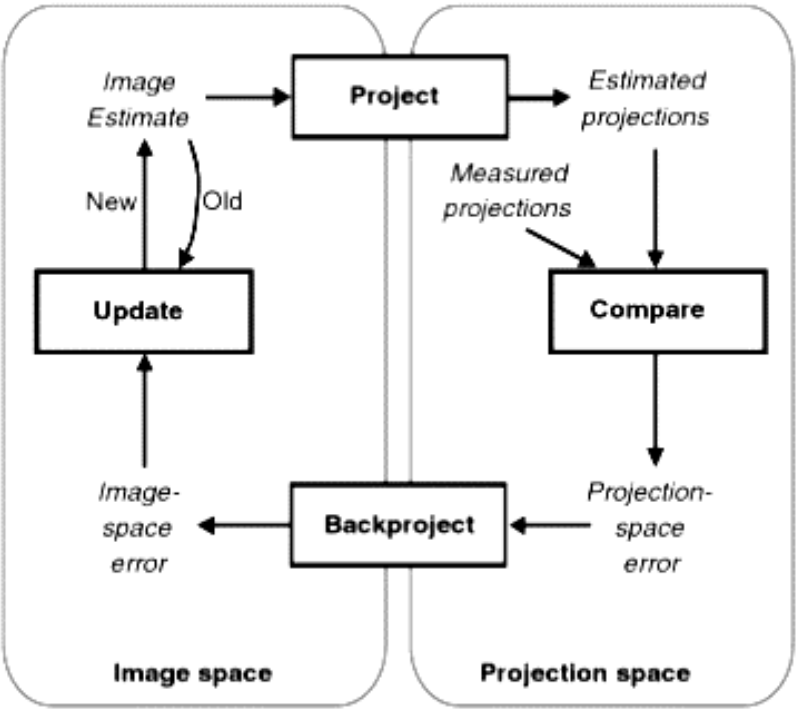

Figure 3.10: Iterative Reconstruction scheme. The scheme is repeated until it satisfies a stopping criterion. All process starts with an initial image estimate which is forward back-projected. In the projection space the measured projections are compared to estimated projections given by the previous operation and an error factor is derived and back-projected to the image space, using the system matrix. This error is used to update the current image estimate. [69]

detectors; and the attenuation of the medium (ρ) along the LOR defined. Jacobson et al. In 2000 [17] expressed this as:

$$a_{ij} = g_{ij} d_i rho_i \tag{3.3}$$

The existence of low sensitivity regions in the detector due to gaps between detector components can be compensated with the geometric probability factor, also known by solid angle factor.

In our system, gaps are accounted for, together the term d of the previous equation, using normalization acquisitions. These are performed measuring the response of the detector to a uniform source equally illuminating the whole detector area. Considering N the number of counts in each LOR, the normalization coefficients are then given by *1/N*. However, the number of LORs and voxels involved in the calculation of a system matrix makes difficult the pre-computation and storage process of such a large matrix. Thus, instead of the system matrix, a sensitivity image is pre-calculated and provided as input to the reconstruction algorithm. For LM reconstruction, the pre-computation of the sensitivity image consists on performing a back-projection of the efficiency correction coefficients.

3.3.3 Algorithm for Image Reconstruction and Normalization

List Mode Reconstruction Algorithm

3D-OSEM List-Mode algorithm. This is the most recently implemented reconstruction algorithm in the context of the Clear-PEM project [9]. This software provides images in a very short period of time for low statistic data sets, directly using DOI coordinates obtained by the system with no need for projection at the crystals face or histograming. Additionally, the algorithm incorporates correction for random events during reconstruction and the possibility of using Metz filtering inter-iterations for regularization. Using the delayed coincidences data obtained in parallel with the prompts data is performed correction of random events, via a smoothed correction image [10].

All the detailed steps about List-mode reconstruction method are described in [63] and will be briefly resumed here. In List-mode reconstruction, all detected events are considered one by one. Assuming that the i_{th} event is along the n_ith LOR, the reconstruction algorithm to maximize logarithmic likelihood function is formulated as

$$x_k^{n+1} = x_k^n \frac{1}{\sum_M^{j-1} w_j c_{j,k}} \sum_{i=1}^{N} \frac{c_{n_i k}}{\sum_{k'=1}^{K} c_{n_i k'} x_{k'}^n} \tag{3.4}$$

in which x_k is the reconstructed value of the kth voxel of the image, K is the total number of voxels to be reconstructed, M is the number of LORs, $c_{j,k}$ denotes the probability that an event from the k_{th}voxel is detected in the j_{th} LOR, N is the total number of events detected, and w_j is the weight assigned to the j_{th} LOR which accounts for attenuation and detector sensitivity. In this equation, random and scattered events are ignored. The system probability factor $c_{j,k}$ is calculated as the length of the ray from j_{th} LOR intersecting with the k_{th} voxel with the Siddon raytracing algorithm [56]–[68].

In this implementation, it is ignored the contribution of the attenuation correction to the sensitivity map and, therefore, it becomes independent to the imaged object. This is because the calculation of the sensitivity map for each specific study is very time consuming. Accordingly, the map is pre-estimated according to the results of acquiring, usually, a planar flood or a cylinder phantom containing Ge-68 or F-18 which placed in the center and aligned with the detector heads.

The actual sensitivity matrix can be formulated by

$$\varepsilon_k \approx S \cdot \hat{\varepsilon_k} \tag{3.5}$$

where S is the scaling factor that is constant throughout all the voxels k in the image space. The acquisition and calculation of the nominal efficiency matrix takes into account the geometrical settings of the system (e.g. distance between two detectors) [63]. So, if the same protocol f acquisition is used, the calculated matrix can be stored and reused for all the studies performed.

Although S in Eq. 3.5 is unknown, we make use of the self-normalizing and non-negative feature of the algorithm defined in Eq. 3.4 [51] and obtain the heuristic list-mode reconstruction algorithm without consideration of random and scattered events [63]. Here, a normalization factor is calculated for each iteration. Also, a 3D Metz filter is implemented as inter-iteration filtering to suppress high frequency noise, while preserving information in low frequency and amplifying signals in mid-range frequency [64], [65]. The transfer function Metz (k_x, k_y, k_z) of the filter in Fourier space is calculated according to

$$Metz(k_x, k_y, k_z) = \frac{1 - (1 - [G(k_x, k_y, k_z)]^2)^{p+1}}{G(k_x, k_y, k_z)} \tag{3.6}$$

in which *G(k_x, k_y, k_z)* is a Gaussian filter defined by the full width at half maximum (FWHM), p is called the Metz power. When $p = 0$, the filter is then degraded as a Gaussian filter. The choice of FWHM and p for the filter is dependent on the statistics of the acquisition. Here we select $FWHM = 3mm$ and $p = 0{,}5$ for standard clinical applications based on various tests and validations [63].

The method described above was already defined for the Clear-PEM project, but it was restructured and since the geometrical settings of SiPM-based PET-ToF are completely different. To obtained the final images using this method, the next procedure needs to be followed:

1. Reconstruct the image

./ClearPEM_LMRec -i <input_file.lm> -o <output_prefix> -n <normalization_prefix> -d <plates_distance>

./ClearPEM_LMRec -i mouse.lm -o mouse -n normalizacao -d 243 -pixel-lentgh 1

Optional

- iterations X: *to perform X iterations (default: 7)*

- filter-gauss3d X: *uses a FHWM filter of X mm (default: 1.5mm)*

Normalization

Data normalization can be challenging and aims at correction a group of effects with geometrical and non-geometrical causes [12]. The solid angle defined by the detector is one of the main effects of this kind. It describes the differences on sampling for different detector elements depending on the distance of the defined LOR to the center of the field-of-view. The angle of incidence of the photon and scatter in the crystals will also affect detection, mainly due to regions of low detection efficiency between crystals, gaps,

and the deviation of the photon trajectory out of the FOV. From LOR to LOR, crystals represent an important cause for non-uniformity and different detection probability. Their growing process and subsequent processing before being incorporated in an imaging scanner determine the presence of variations on the crystals' intrinsic efficiency that cannot be predicted. This effect, along with the small performance changes on the associated electronics, represents a non-geometric factor that contributes to image degradation.

Normalization can be performed using direct or indirect methods. Currently, the system uses direct method by the means of a long acquisition with a uniform and thin 68-Ge planar source. The source is placed half-way between the detectors heads, parallel to them, equally illuminating every crystal composing the heads. This type of source (thin) has been described as having an ideal geometry for normalization purposes [12] since it presents little scatter. The normalization coefficients are obtained by direct inversion of the number of counts obtained in each LOR. Due to source replacement constraints related to natural decay, a custom made fill able planar source considered and tested with 18F.

Sensitivity images used as input for normalization to obtained a better final image estimation represents the longest step and should be performed in advance to save time. The method used in this project was developed by Liji and follows the nest procedure:

1. Convert ELM2 file into List Mode format of the algorithm (common step in the reconstruction phase)

./elm2todkfz -o file.lm file.elm2

2. Create normalization files

./Norm_Total_Gen <plates distance> <pixel length> <angles file> <input file> <output prefix>

Example: ./Norm_Total_Gen 243 1 angles.txt normalization.lm normalization

3.3.4 TOF Algorithm

Due to the limited angular coverage provided by the two detector heads composing the detector, most of the particles that successfully escape the object will not strike the detector. Since PEM technique is based on the detection of both photons originated from the annihilation, an event is not considered valid unless the two generated particles hit the detector.

The detection process of the photon is modeled projecting the particle according to its final direction and calculating the intersection with three planar geometries, with the dimensions of the distance between SiPM detector heads. In the case of the photon reaches the detector and its energy is above the defined threshold, the event will be stored in a list mode file, otherwise it is discarded. MC methods allow to sort events by their history since generation to detection. During the simulation is performed energy selection, so the list

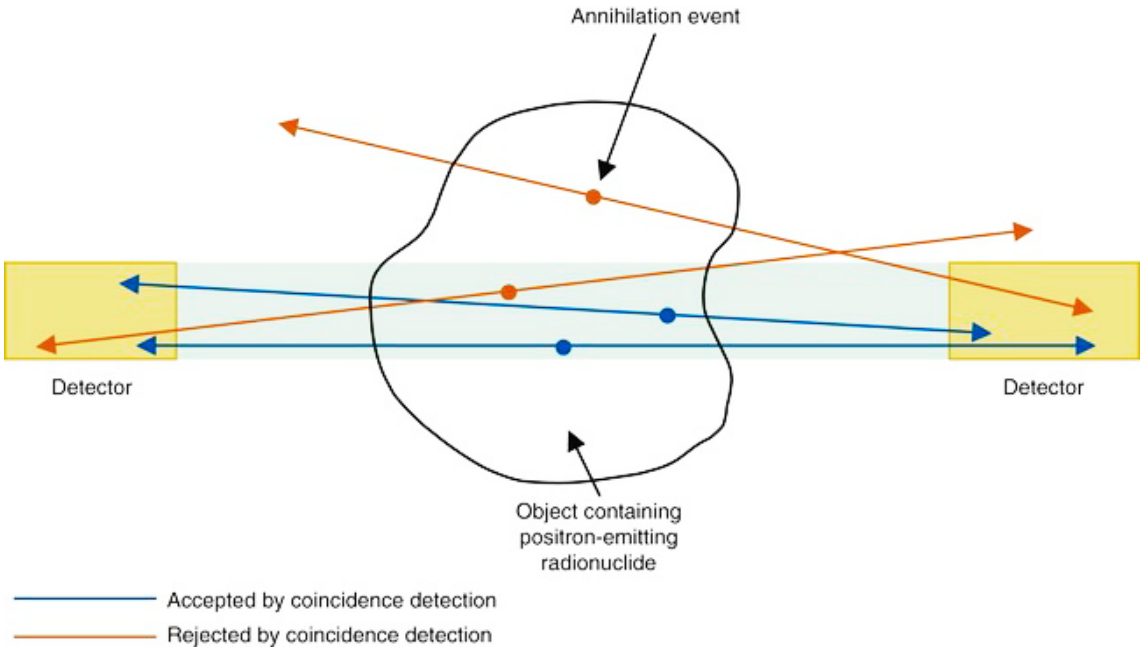

Figure 3.11: Representation of the detected events in Positron Emission Tomography. Volume (shaded area) from which a pair of simultaneously emitted annihilation photons can be detected in coincidence by a pair of detectors. Not all decays in this volume will lead to recorded events, because it is necessary that both photons strike the detectors. Outside the shaded volume, it is impossible to detect annihilation photons in coincidence unless one or both undergo a Compton scatter in the tissue and change direction.

mode file saved contained just positional information (x_1, y_1, z_1, x_2, y_2, z_2) plus to other fields – a weight and a flag – that ca be useful during reconstruction for data correction approaches. This positional information allows the calculation of the associated LOR.

$$LOR = \sqrt{(x_1 - x_2)^2 + (y_1 - y_2)^2 + (z_1 - z_2)^2} \tag{3.7}$$

Only this information is used for conventional back projection image reconstruction. Using this method, detected event is going to be projected to all voxels with same weight between detector pairs (figure 3.13a). This method is faster and needs less information, but the big disadvantage is related with the statistical noise from activity in one voxel will add noise to all voxels which will result in a large noise amplification.

In order to fight this big disadvantage, a technique called Time-of-Flight (ToF) has been applied in PET image reconstruction. This technique allows the use of the same procedure for data acquiring, but here the list mode file saved contain not only positional information, but also time information (x_1, y_1, z_1, t_1, x_2, y_2, z_2, t_2). This information will give up the possibility of determine the location along a line between the two detectors at which the annihilation photons originated by determining the difference in the time at which they are detected by the two detectors. If the difference in the arrival times of the photons is Δt, the location of the annihilation event, with respect to the midpoint between the two detectors, is given by

$$\Delta d = \frac{c(t_1 - t_2)}{2} \tag{3.8}$$

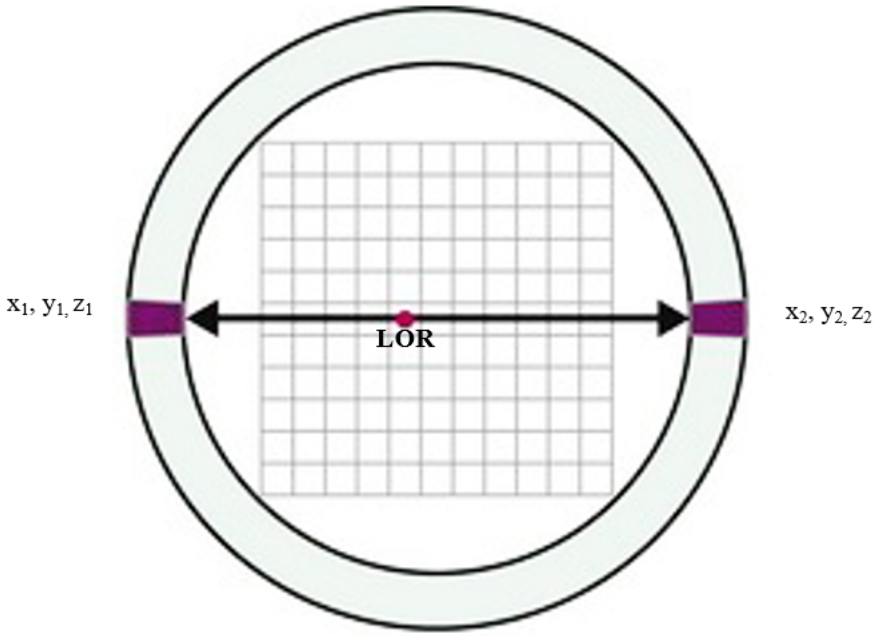

Figure 3.12: A pair of annihilation photons are emitted from a source (red dot) and detected in coincidence by opposing detectors. The LOR is defined by the photons path.

where c is the velocity of light ($3x10^{10}$ cm/sec). With this possibility of localize the annihilation point, detected event is going to be projected to voxels with probabilities that follow a Gaussian distribution, centered on pixel Δd, from the center of the scanner and with a full width at half maximum equal to the timing resolution of the detector pair (figure 3.13b). The Gaussian distribution will be characterized by (d, $c\Delta t/2$).

This method is more time consuming, but the statistical noise from one voxel will add noise to only a few nearby voxels which will result in Small Noise Amplification. Based on this the code already develop were adapted to have in account TOF information and the adapted part is presented on Appendix A.

3.4 Evaluation of the Image Reconstruction Method

3.4.1 Normalization Effects on Image Recontruction

In this section the effect of the normalization correction on reconstruction image is evaluated using computed Monte Carlo sensitivity images. For that purpose, three different uniform phantoms for system normalization were used, and then the sensitivity image of each one was reconstructed. These sensitivity images are then used as input to normalize the final image estimate in each iteration during image reconstruction. Consequently, the aim of this study is to evaluate the quality of the output images when different types of sensitivity images are used. It is important to highlight that the Monte Carlo methodology presented here is based on a realistic and detailed description of the detector geometry to calculate the sensitivity image.

Normalization procedures represent a method to equalize the response of single de-

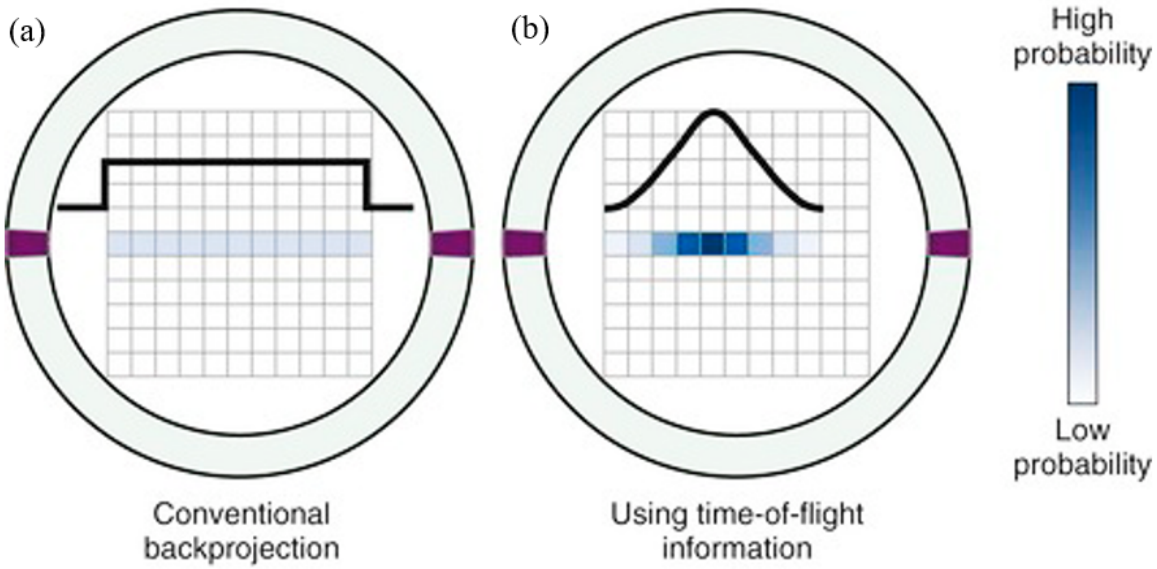

Figure 3.13: (a) In non-TOF reconstruction, all volume elements n found in the object along the line of response contributes in the same away to the noise in each image element. (b) In TOF reconstruction, because of the better localization of each event along the LOR, only the volume elements n adjacent to the position identified by the measured TOF contribute to the local noise. The time resolution limits the number of elements contributing to the noise.

tectors or line-of-response (LOR). These are performed measuring the response of the detector to a uniform source equally illuminating the whole detector area. The normalization coefficients are then given by $1/N$, where N is the number of counts in each LOR. When no attenuation and normalization coefficients are available artifacts will appear in the reconstructed image (e.g. lack of compensation for the gaps results in a stripe pattern).

As is was mentioned, PETsys demonstrator uses a direct method for normalization, by means of a long acquisition with a uniform and thin planar source. The source is placed half-way between the detector heads, parallel to them, equally illuminating every crystal composing the heads which was reproduced in this simulations for different types of sources.

The acquired sensitivity images are presented in images below. The first normalization study was performed using a uniform cylinder phantom, with a radius of 90 mm and a length of 60 mm. The cylinder was assumed to be made of water with photon energies of 511 keV. For the purpose of normalization, a long acquisition was performed for a detector head distance of 234.8 mm and without rotation of the detector. The analysis was performed using ROOT toolkit, a data analysis framework developed at CERN, and the image was then observed using AMIDE software.

The same procedure was used to obtain sensitivity images from a thin planar source and from a thin ring repeated 23 times along z-axis. Both sources were assumed to be made of water with photon energies of 511 keV. The planar source was simulated with a length of 60 mm and a thickness of 1.5 mm. Also, the ring was a thickness of 1.5 mm, an inner radius of 88.5 mm and, consequently, an outer radius of 90 mm. In order to fill all length of the demonstrator, the ring source was repeated in z-axis several times with

a distance of 1 mm. It is important to highlight that thin geometry was chosen since it is known as presenting little scatter.

The aim of studying the normalization process was to understand how the normalization correction on reconstruction image can affect the final image in terms of quality. Study was performed using computed Monte Carlo sensitivity images, based on three different simulated phantoms with different shapes. Sensitivity images were then reconstructed using data obtained from the simulation and with a specific algorithm already referred, and then these sensitivity images were used as input to normalize the final image estimate in each iteration during image reconstruction.

In order to understand qualitatively the behaviour of the sensitivity images in final image estimate, data from three different simulated phantoms were obtained and images were reconstructed using as input the three different sensitivity images. For that 3D-OSEM List-Mode algorithm was used and the next phantoms, described in section 3.1.2, were used:

- The uniform cylinder phantom with a radius of 50 mm, a length of 60 mm and an activity of 10 MBq;
- The ring with an inner radius of 50 and an outer radius of 45 mm, which matches to a thickness of 5 mm, and an activity of 10 MBq;
- A Derenzo Phantom composed by rods with radius of 1.25 mm, 1 mm, 0.75 mm, 0.675 mm and 0.5 mm. The activity of each group of rods with the same dimensions were 12500 Bq, 10000 Bq, 7500 Bq, 6000 Bq and 5000 Bq, respectively.

Images were displayed with AMIDE and line profiles were extracted from each reconstructed image using AMIDE Line Profile tool. After evaluate the results obtained, the better sensitivity image used for normalization was selected and used for image reconstruction in the next study.

3.4.2 The Impact of Using TOF on Image Reconstruction

Improvement of both spatial resolution and detection sensitivity in PET scanners has the potential to increase lesion detectability, needed for a diagnosis of the disease in early stages where the treatment is usually more effective. However, designing a PET scanner able to fulfil the requirements of high spatial resolution and high sensitivity simultaneously is quite demanding. Base on this, TOF information in image reconstruction appears to an alternative for noise reduction, faster image convergence and SNR improvement.

The aim of this step of the work is to understand the benefits of time of flight information in image reconstruction. For that purpose, a Monte Carlo simulation was performed and phantoms' geometries were defined using GATE software as well as the geometry of the demonstrator previously validated.

A cylinder full of water was simulated with a radius of 50 mm and a length of 60 mm. Inside of the cylinder six equal point sources with 1 mm diameter each were placed in the positions A - (0,0,0), B - (25,0,0), C - (50,0,0), D - (0,25,0), E - (0,50,0), F - (0,0,25) mm.

All sources were assumed to be uniform and with photon energies of 511 keV, also the activity of each point source was defined as 7.5 Mbq. Based on this simulation, images were reconstructed using 3D-OSEM List-Mode algorithm with and without Time-of-Flight information. For the algorithm with TOF information a fixed value of Time Resolution of 500 ps was used for a Energy window of 450 kev. This phantom was used in order to understand if the reconstruction algorithm using non-TOF information works correctly in all axis direction (x-, y- and y-).

Images obtained were evaluated using AMIDE. Both quantitative and qualitative analysis were done. To do that we extracted line profiles from each reconstructed image over axial slices on horizontal and vertical positions using AMIDE Line Profile Tool. Spatial resolution was evaluated for both images using this tool, since it can be characterized by the FWHM of a Gaussian fit to profiles taken in a transverse slice for the y- and the x- axis. Regions of Interest (ROIs) were also drown using AMIDE capabilities for ROI statistics calculations. Two ROIs with different dimensions were traced for both images. The smaller ROI had a volume of approximately 11 mm^3 and the bigger one a volume of 105 mm^3, covering 46 and 330 voxels of the image respectively. Results for TOF and non-TOF imaging conditions were evaluated.

Two more simulations were performed in the scope of this study which were then reconstructed using the 3D-OSEM List-Mode algorithm without and with TOF information. The first simulation consisted of a uniform cylindrical phantom with a radius of 50 mm, a length of 60 mm and having a uniform activity distribution of 10MBq. The data acquired from this simulation was already reconstructed using the non-TOF algorithm in the previous study, and is used here to understand if it is possible verify improvements reconstructing the same data using TOF algorithm. The second simulation consisted of a Derenzo phantom, in order to investigate if the intrinsic resolution of the system is enhanced with the use of TOF information in image reconstruction. The phantom is composed by rods with radius of 1.2 mm, 1 mm, 0.75 mm, 0.675 mm and 0.5 mm, each group with activities of 12500 Bq, 10000 Bq, 7500 Bq, 6000 Bq and 5000 Bq, respectively. Also here, all sources were assumed to be uniform and with photon energies of 511 keV. Obtained results in this step of the study were evaluated qualitatively using AMIDE.

Chapter 4

Results and Discussion

4.1 Simulation in GATE – Validation Study

As stated before, during the first months of this work, we performed an extensive literature research on the available TOF-PET systems and image reconstruction methods for this technique. While doing this research, we had into account the methods already developed for the Clear-PEM project and now adapted for the new detector configuration. In order to evaluate and understand better all the reconstruction image process, a first study without TOF information for different sources was done. Also, this study was essential to evaluate some of the demonstrator characteristics, such as its intrinsic spatial resolution in different planes.

As stated above, data acquired experimentally from a point source of Na-22 was used in the scope of this study and the intrinsic spatial resolution of the demonstrator in axial and transaxial planes was evaluated. The images were reconstructed based on the List-Mode reconstruction algorithm without TOF information. After finishing the reconstruction process, the images were evaluated with AMIDE software. A line profile in both planes for the point source was traced with the profile tool present on AMIDE to allow the evaluation of the full width at half maximum (FWHM) value. It was seen that the best value, which means the smallest one, corresponds to the axial plane (1.449mm) and, considering all the plans, an average value of 1.77 +/- 0.003mm FWHM was achieved (Table 4.1). It is important to refer that these values were obtained without correction for the source dimension in the centre of the field of view.

By applying the same methodology, results for the Ge-68 line source present in Figure4.2. As expected from previous studies, the smaller value of the FWHM was obtained in the axial plane (1.953mm) and an average value of 2.23 +/- 0.002mm FWHM was measured considering both planes.

In the line source measurements, a problem in image reconstruction for compensating the gaps was found (Figure4.2 – coronal view). This problem could be due to the normalization procedure and has to be evaluated and corrected in the next studies to achieve a better image uniformity.

Therefore, some simulations in GATE were performed to compare with experimental results. The geometry and the characteristics of the demonstrator were all defined in

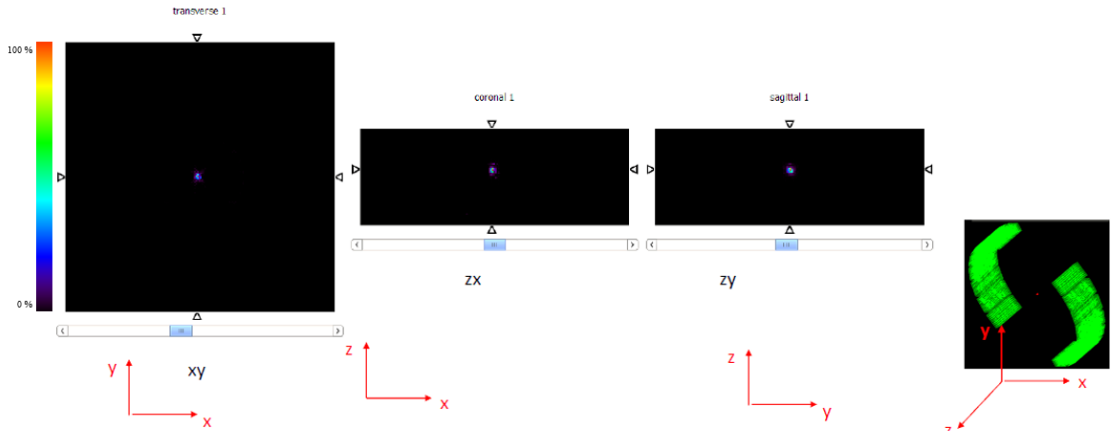

Figure 4.1: Image reconstruction for a measurement using the SiPM-based PET-TOF demonstrator and a Na22 point source with 1mm nominal diameter.

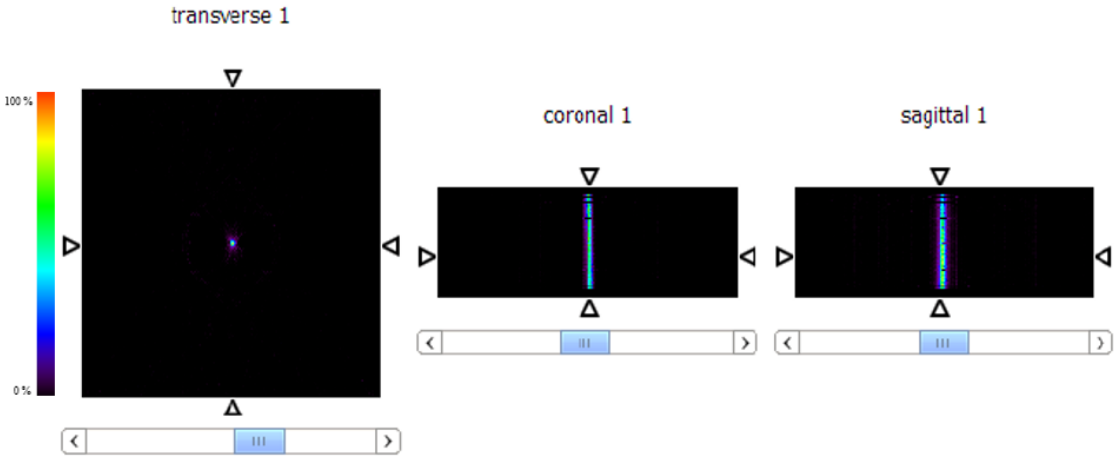

Figure 4.2: Image reconstruction for a measurement using the SiPM-based PET-TOF demonstrator and a Ge68 line source with 1.5mm diameter and a length of 60mm.

Table 4.1: Values obtained for the full width at half maximum (FWHM) for the experimental data profiles in the x, y and z planes.

	Point Source of Na-22		**Line Source of Ge-68**	
Planes	**FWHM**	**Uncertainty**	**FWHM**	**Uncertainty**
X	1.449 mm	+/-0.003 mm	1.953 mm	+/-0.004 mm
Y	1.701 mm	+/-0.004 mm	2.54 mm	+/-0.005 mm
Z	2.813 mm	+/-0.002 mm	-	-

the software, as all the specifications of the source and its dimensions. Results for the simulation using a line source are presented in Figures 4.3 and 4.4. As it was expected the best value for FWHM was in the axial plane (1.994 mm) and an average value of 2.312 +/- 0.002 mm FWHM was measured in this case. It is important to highlight that here the problem for compensating gaps is also seen, which gave us the certain that the problem is in the normalization software and has to be improved.

Results obtained for experimental and simulated data were similar for both simulations, which allows us to conclude that the simulation design was well performed and it's

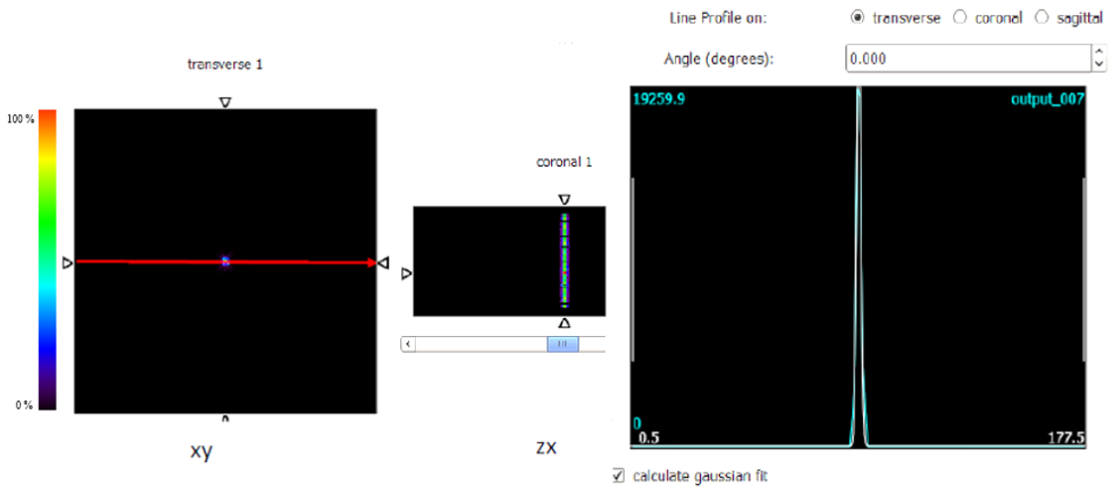

Figure 4.3: Image reconstruction for the simulation performed with GATE. Both demonstrator and source were simulated using the characteristics of the SiPM-based PET-TOF demonstrator and the Ge68 line source with 1,5 mm diameter and a length of 60 mm, respectively. Profile in axial plane was obtained with the profile tool present on AMIDE to allow the evaluation of the full width at half maximum (FWHM) value.

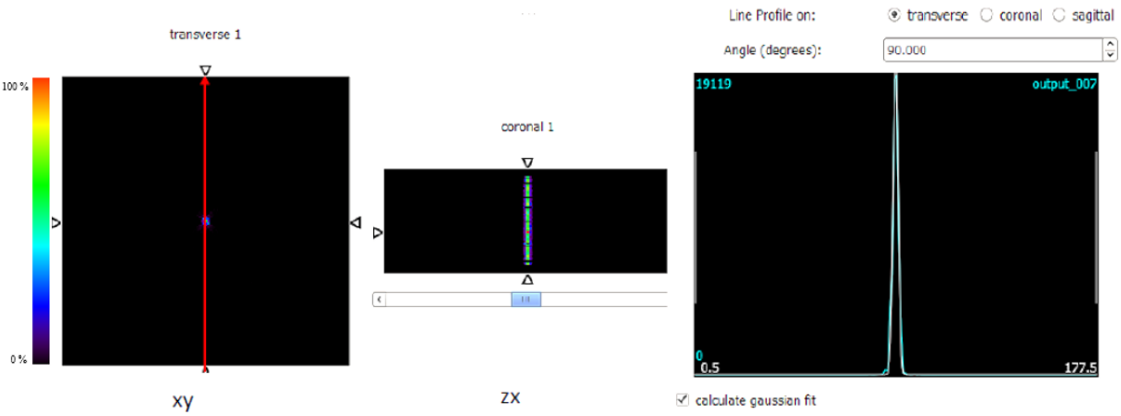

Figure 4.4: Image reconstruction for the simulation performed with Gate Software. Profile in transaxial plane was obtained with the profile tool present on AMIDE to allow the evaluation of the full width at half maximum (FWHM) value.

Table 4.2: Summary of the average values obtained for FWHM for the experimental and the simulated data.

	Experimental Data		**Simulated Data**	
Source	**Avg. FWHM**	**Uncertainty**	**Avg. FWHM**	**Uncertainty**
Point source of Na-22	1.77 mm	+/-0.01 mm	-	-
Line source of Ge-68	2.23 mm	+/-0.01 mm	2.32 mm	+/-0.002 mm

possible to use it in further studies. The evaluated values of FWHM obtained to evaluate spatial resolution, were also similar for the simulation and the experimental data. Specifically, for the axial plane, values were better than the ones obtained for the transaxial plane for both sources. Ideally, the resolution in both planes should be the same to permit a true volumetric imaging, which it's not possible to achieve specially due to intrinsically

specifications (scintillator material type, crystal dimensions, size of the field-of-view, and others) [4].

4.2 Normalization Study

In this section the effect of the normalization correction on reconstruction image is presented using computed Monte Carlo sensitivity images. For that purpose, three different uniform phantoms for system normalization were used, and then the sensitivity image of each one was reconstructed. As is was mentioned, PETsys demonstrator uses a direct method for normalization, by means of a long acquisition with a uniform and thin planar source. The source is placed half-way between the detector heads, parallel to them, equally illuminating every crystal composing the heads which was reproduced in this simulations for different types of sources.

Sensitivity images obtained with these simulations are presented in Figure 4.5. As it is possible to see in the referred image the intensity of the images directly depends on the simulated phantom. Figure 4.5a shows cylinder intensity image, which is the one that presents biggest values of intensity. Also, it's possible to verify a ring-like repeated sensitivity image in the top and the bottom of the image (Figure 4.5c), which could be related with an error in the simulation. Figure 4.5b related with planar phantom presents a similar behaviour comparatively with cylinder simulation. A non-uniform distribution is possible to see in all images and all of them present a peak of intensity in the central point. Furthermore, the LORs angular range for detected coincidence events is smaller in the edges of the image and the relative number of events actually passing through the gaps increases. This will lead to a loss of detection efficiency comparatively to the central region as observed.

In order to better understand the difference of normalization effects and intensity behaviour for all the simulated phantom, the sensitivity values of the obtained images were normalized accordingly to the biggest value obtained in all simulations. Figure 4.6 shows the graph with normalized intensity values obtained for each phantom. Values were obtained using the Line Profile tool of AMIDE, placed in the sagittal view of each obtained sensitivity image as shown in the Figure 4.5.

The main characteristics of sensitivities images presented in this study is the triangular non-uniform shape peaked at the central slice. Also, it's possible to verify that the non-uniform behaviour of the acquired values for each phantom are similar. It displays a complex pattern that differs considerable from the expected smooth sensitivity profile. This fact could be justified with in-detector effects, as well as the fact that a realistic geometry of the scanner is used which can have a significant effect in the calculated sensitivity images [10].

Also, solid angle defined by the detector is one of the main effects that can be challenging for normalization. It describes the differences on sampling for different detector elements depending on the distance of the defined LOR to the centre of the field-of-view (FOV). The angle of incidence of the photon and scatter in the crystals can also affect detection, mainly due to regions of low detection efficiency between crystals, gaps, and the

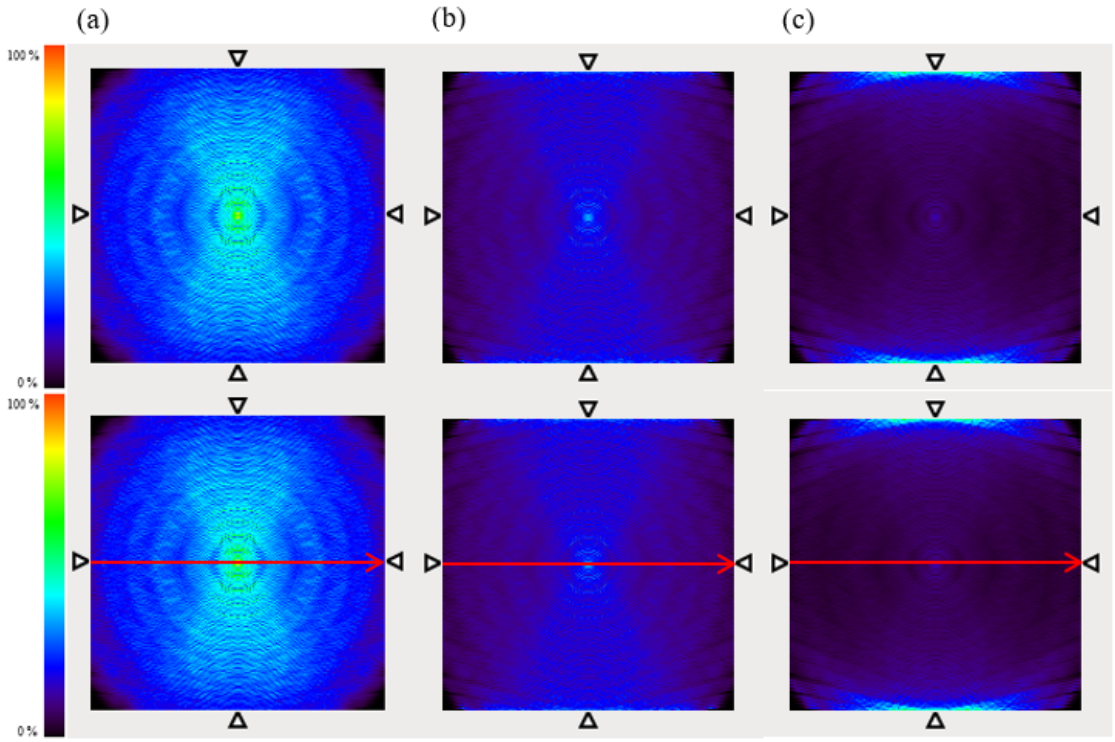

Figure 4.5: Transaxial view of sensitivity images along x- and y- axis for three different simulations: a) sensitivity image obtained for the cylindrical phantom, b) sensitivity image obtained for the planar phantom; c) sensitivity image obtained for the ring phantom.

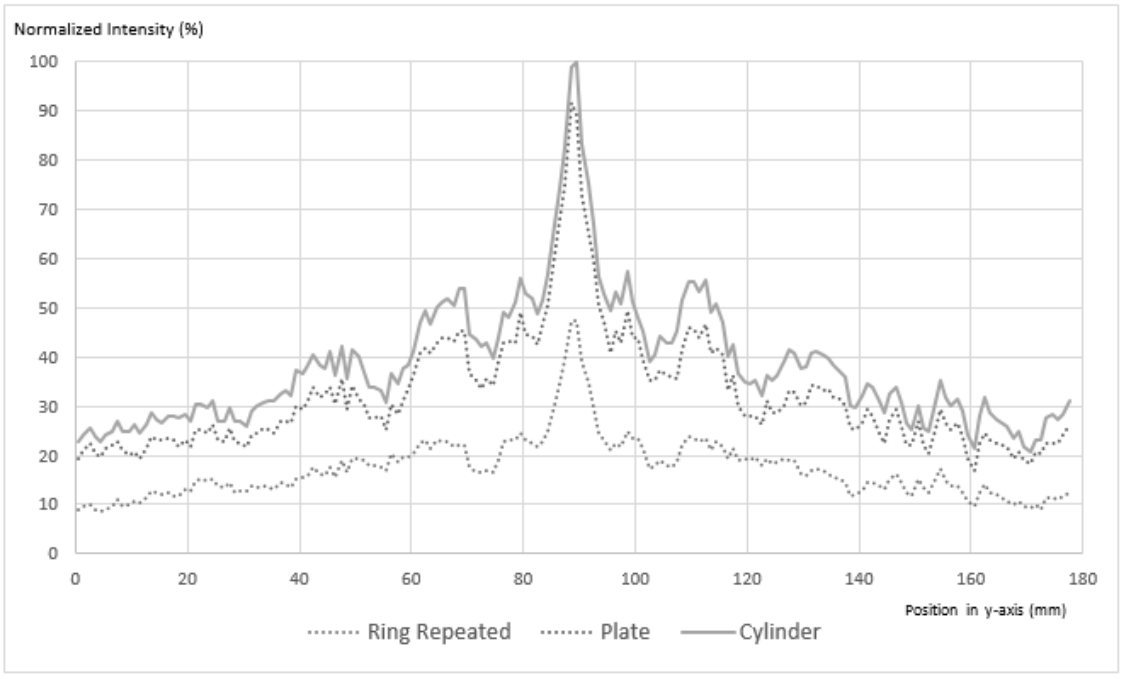

Figure 4.6: Line profiles over the centre of sensitivity images used as input for normalization that were presented above. Values obtained with AMIDE Line Profile tool.

deviation of photon trajectory out of the FOV. From LOR to LOR, crystals can represent an important cause for non-uniformity and different detection probability. This effect represents a factor that contributes to image degradation.

4.2.1 Normalization Effects on Image Reconstruction

As it was referred before, sensitivity images are then used as input to normalize the final image estimate in each iteration during image reconstruction. Accordingly, the second step of this study is related with final image estimate using as input the three different sensitivity images described above. For that, the 3D-OSEM List-Mode algorithm was used for image reconstruction of three different simulated phantoms. Phantoms' geometries were defined using GATE software as well as the geometry of the demonstrator, which is the same that was used in the previous study.

In Figure 4.7 it is possible to verify final images of the cylinder simulation. All of them presented a blurred background in the centre at the top and the bottom of the image, which could be related with the absence of detectors at that zone. This blurred background is more evident in Figure 4.7b, which results in distortion of the cylinder shape but with a uniform distribution. Image reconstructed using the cylinder sensitivity image for normalization presented also a uniform distribution but with less blurred background (Fig. 4.7a). Only Figure 4.7c presents a non-uniform distribution, close to the centre of the cylinder, however is also the one that presents the shape well defined.

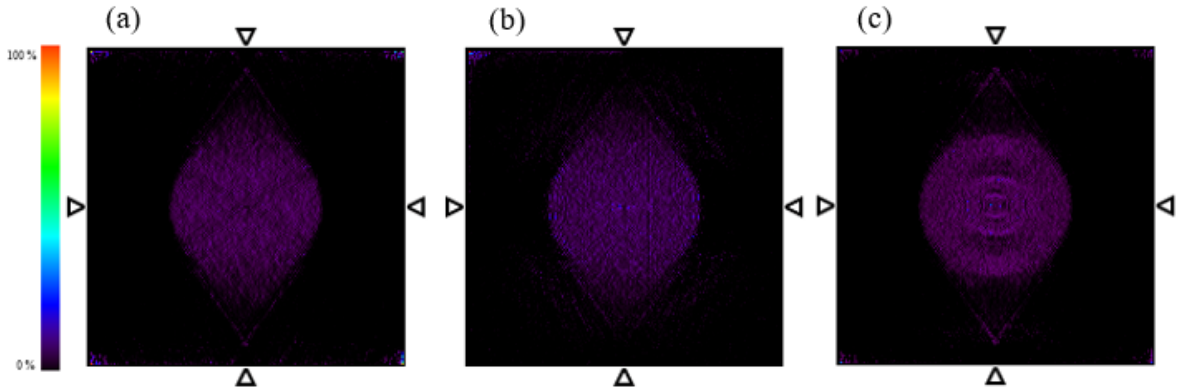

Figure 4.7: Uniform cylinder with diameter of 50 mm, simulated using a realistic simulation in Gate. For (a) image was reconstructed using for normalization a cylinder sensitivity image, for (b) image was reconstructed using for normalization a plate sensitivity image (c) image was reconstructed using for normalization a ring sensitivity image. Central axial slice is presented.

Line profiles were extracted from each reconstructed image of the cylinder and are presented in Figures 4.8, 4.9 and 4.10, which was done using AMIDE Line Profile tool. Values of recorded events are similar for the first and the second image, only the third one presents biggest values.

It is possible to verify that the image reconstructed using ring sensitivity image for normalization is the one that presents more variations, which results in non-uniformities on the image. Despite the fact of having a distortion in the shape at the top and the bottom, the image reconstructed using the planar sensitivity image for normalization is the one that presents more uniform values. Notwithstanding, a line profile obtained from a uniform cylinder it is expected to approach a flat profile in contrast with the ones obtained. It is also possible to verify that line profiles get noisy, essentially due to statistical fluctuations and poor correction of the detector gaps. Normalization corrections used on the phantom

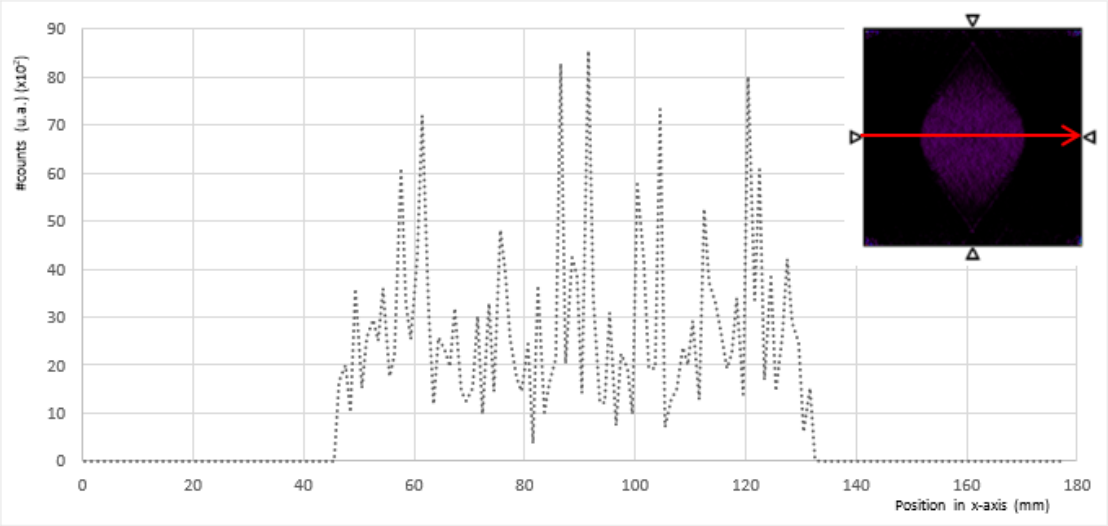

Figure 4.8: Line profiles over axial slices for each reconstructed cylinder image using for normalization the cylinder sensitivity image already discussed.

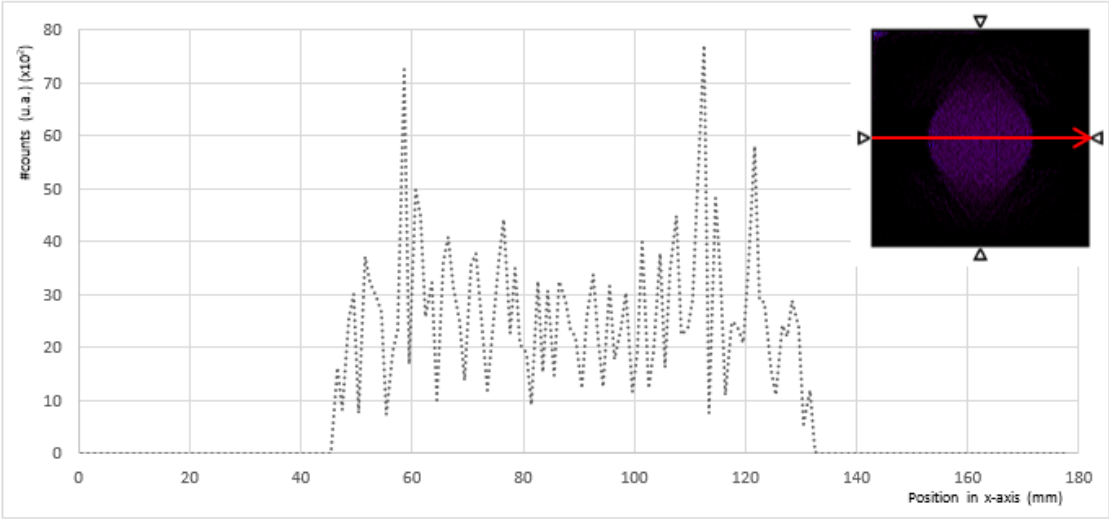

Figure 4.9: Line profiles over axial slices for each reconstructed cylinder image using for normalization the plate sensitivity image already discussed.

data were not completely efficient and therefore this correction may be improved on terms of statistics and, maybe, time of acquisition.

In figure 4.11 the images related with the final image obtained for the ring simulation are presented. Both present the same small distortion on the top and the bottom of the ring, which is, one more time, related with the absence of detector heads at that zone. Here it is possible to verify that all the images are very similar, the biggest difference is presented on the third one since appears to have two small circles in the middle of the ring. This could be related with some artefacts coming from the input image used for normalization.

Also for this case, line profiles were extracted from each reconstructed image of the Ring simulation and are presented in Figures 4.12, 4.13 and 4.14. One more time, values of recorded events for the first and the second image are very similar, the biggest difference

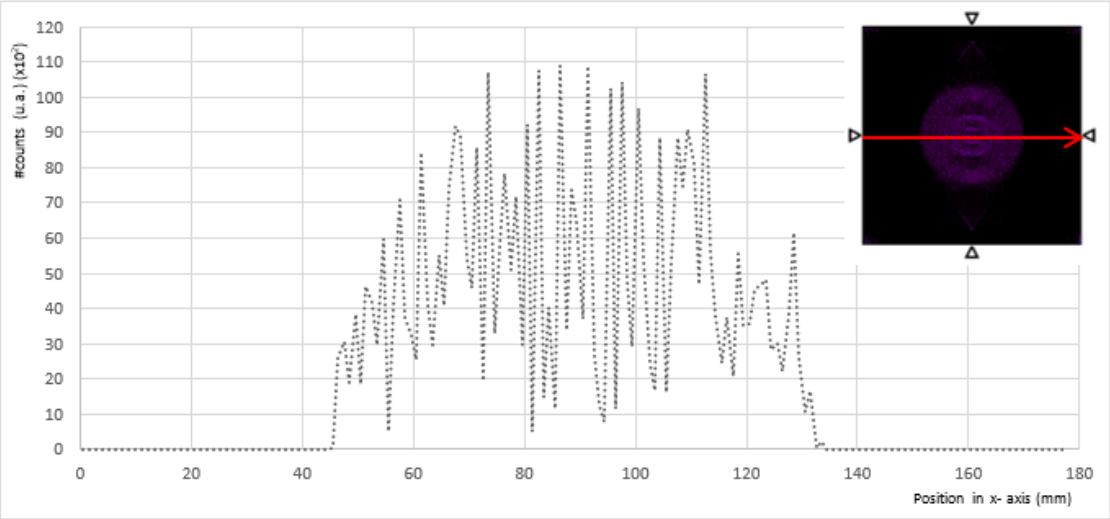

Figure 4.10: Line profiles over axial slices for each reconstructed cylinder image using for normalization the ring sensitivity image already discussed.

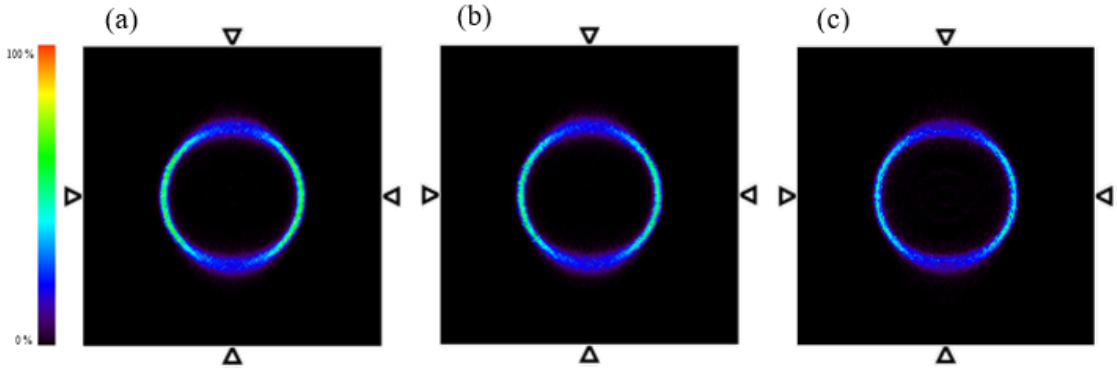

Figure 4.11: Ring phantom with an outer radius of 45 mm and a thickness of 3 mm, simulated using a realistic simulation in Gate. For (a) image was reconstructed using for normalization a cylinder sensitivity image, for (b) image was reconstructed using for normalization a plate sensitivity image (c) image was reconstructed using for normalization a ring sensitivity image. Central axial slice is presented.

is on the localization of this biggest value. For the first image the biggest value of recorded events is on the left side and for the second image is on the right side. Despite this fact, it is possible to verify that both images present two well defined peaks which does not happens in the third image. Here the recorded events are bigger but present artefacts, behaviour also verified for the cylinder line profiles. Blurred circles presented in Figure 4.11c are not possible to see in the graph, as it was expected since the values of recorded events in that circles are really small comparatively with the ones recorded for the simulated ring.

For this simulation, normalization corrections used on the phantom data were really efficient, predominantly on the first and the second image. However, it is important to highlight that the images present some distortion in the superior and inferior part of the ring in the reconstructed image for the three cases, which need to be corrected.

Lastly, images related with the final image obtained for the Derenzo phantom simulation are presented in Figure 4.15. As it was previously referred, the phantom is composed

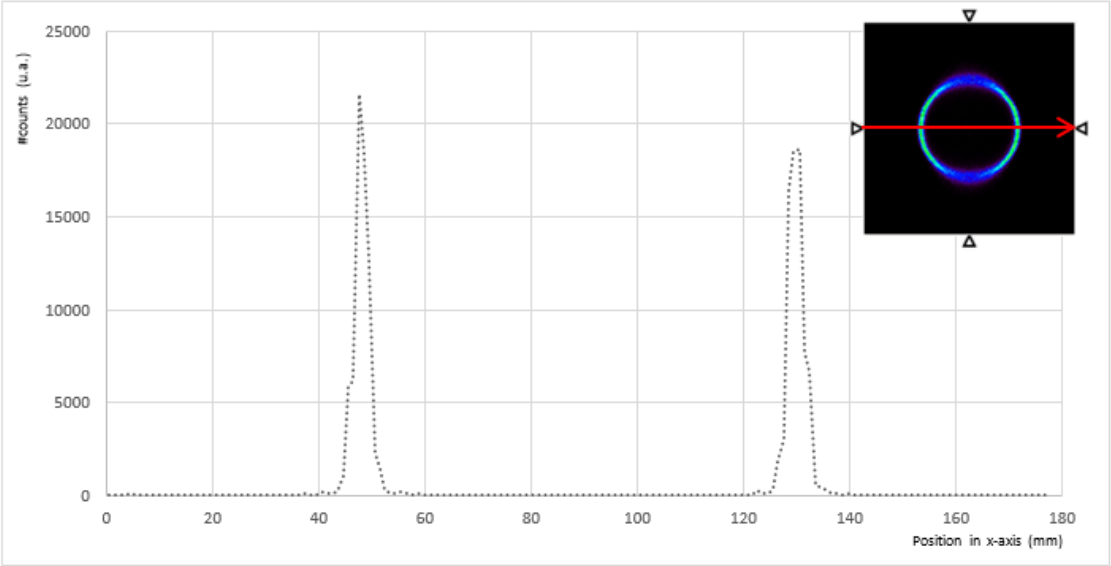

Figure 4.12: Line profiles over axial slices for each reconstructed ring image using for normalization the cylinder sensitivity image already discussed.

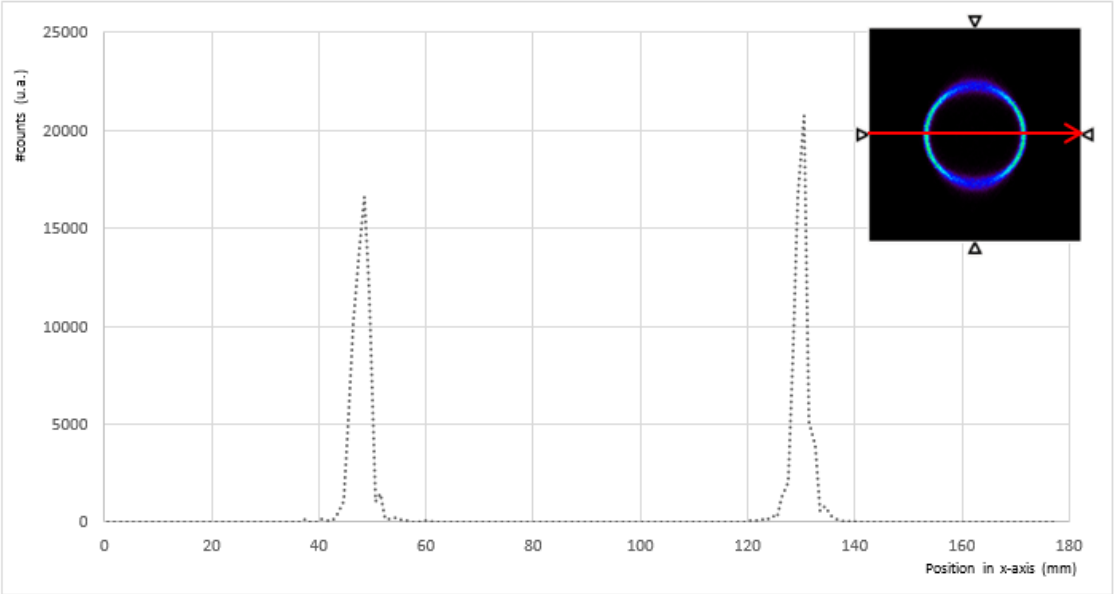

Figure 4.13: Line profiles over axial slices for each reconstructed ring image using for normalization the plate sensitivity image already discussed.

by rods with radius of 1.2 mm, 1 mm, 0.75 mm, 0.675 mm and 0.5 mm. So, the main objective of this part of the study is to understand how the normalization can affect the capability of resolving the rods with different radius.

Figure 4.15a shows Derenzo phantom reconstructed using for normalization the cylinder sensitivity image, which indicates that the 1.3-1 mm resolution can be obtained. For the reconstructed image using for normalization the planar sensitivity image presented in Figure 4.15b, the rods seem to be more distinguished, presenting the ability of resolving 1 mm rods. The worst solving capability is achieved in Figure 4.15c that uses for normalization the ring repeated sensitivity image. This could be justified by the background

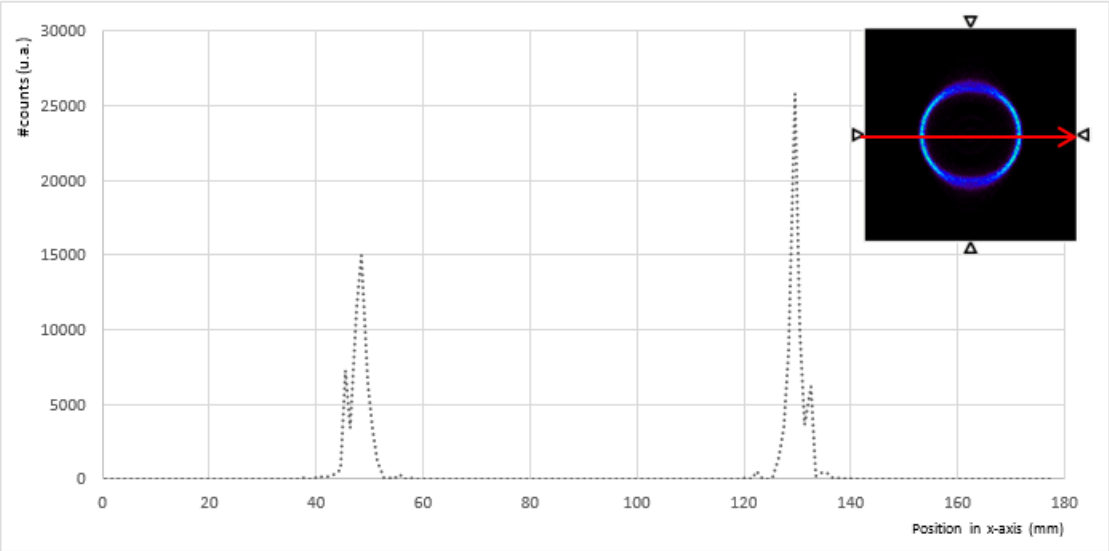

Figure 4.14: Line profiles over axial slices for each reconstructed ring image using for normalization the ring sensitivity image already discussed.

noise presented in the image brought by the input image used for normalization, which does not allow to distinguish correctly the smaller rods.

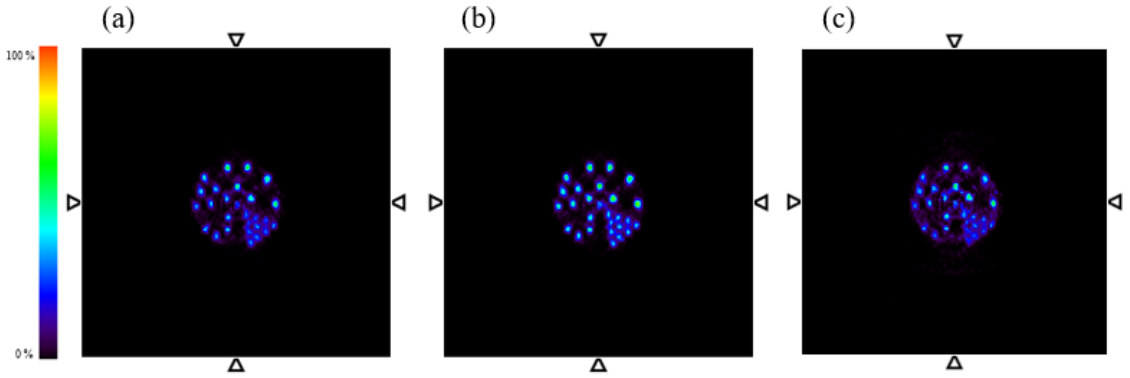

Figure 4.15: Derenzo phantom composed by rods with radius of 1.2 mm, 1 mm, 0.75 mm, 0.675 mm and 0.5 mm, simulated using a realistic simulation in Gate. For (a) image was reconstructed using for normalization a cylinder sensitivity image, for (b) image was reconstructed using for normalization a plate sensitivity image (c) image was reconstructed using for normalization a ring sensitivity image. Central axial slice is presented.

Based on this study, it is possible to conclude that the normalization factors used in image reconstruction as a big influence in the final result obtained. It was verified that the normalization factors achieved using a ring repeated simulation were not efficient in image reconstruction. The best results using different phantoms for image reconstruction were obtained using the planar sensitivity image as input, therefore this will be the only one used for image reconstruction in the next study.

4.3 TOF Impact on Image Reconstruction

In order to better understand the benefits of time of flight information in image reconstruction, a study using a Monte Carlo simulation was performed. Phantoms' geometries were defined using GATE software as well as the geometry of the demonstrator previously validated.

Based on the acquisition during two minutes, images were reconstructed using 3D-OSEM List-Mode algorithm with and without Time-of-Flight information and observed and analysed with AMIDE software and associated Tools. Figure 4.16 shows point sources images without TOF information in three different views, transverse, coronal and sagittal respectively. It is possible to verify that the image is inverted, since point sources in the y- axis are represented in the negative direction, which is probably related with the reconstruction algorithm and is not relevant for the purpose of this study. All the simulated points are similar as it was expected, since all of them as the same shape, dimensions and activity. More irregularities are observed in the near the edges of the detector FOV, especially in the transaxial direction. It is important to highlight that this behaviour was already observed in the previous study.

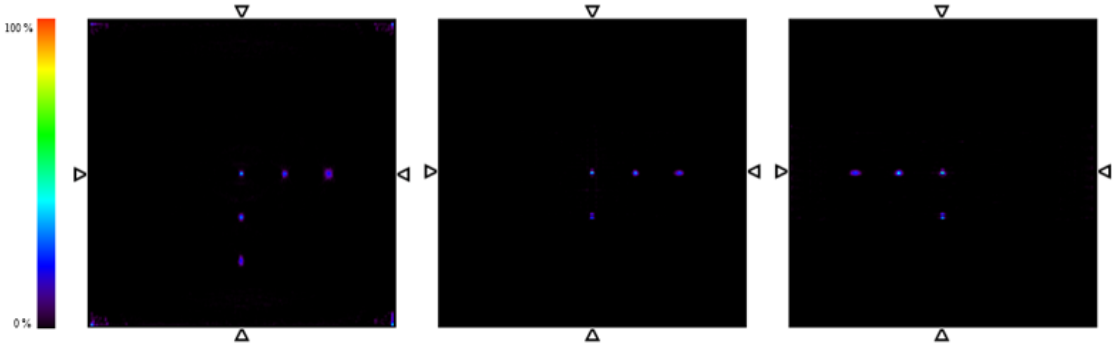

Figure 4.16: Orthogonal image views (transverse, coronal and sagittal respectively) of the reconstructed image using 3D-OSEM List-Mode algorithm without TOF information.

On the other hand, point sources images from the same simulation, but now reconstructed with TOF information, are presented in Figure 4.17. The image steel inverted, since the algorithm used is the same, but with the addition of time-of-flight information. The central point source (position A) appears to have a more intensive colour which means that a higher number of counts were achieved. However, using this methodology it is only possible to verify 5 point sources, and not 6 as it was expected. The point source in position E - (0,50,0) disappeared from the image, which represents a big problem in our reconstruction software, since this behaviour was not expected. Also, point sources near the edges of the detector FOV seems to have poorer spatial resolution, which leads to an image where the point sources in this positions are blurred and less resolved.

To better understand the analytical information provided from the reconstructed images, quantitative data from line profiles and traced ROI were reached. Initially, using the line profile AMIDE Tool, the intensity profiles trough x- and y- axis for both reconstructed images (with and without TOF information) were obtained.

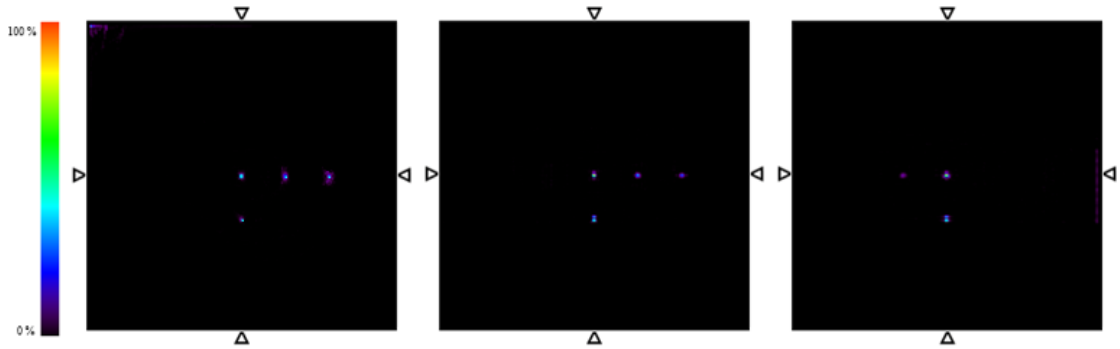

Figure 4.17: Orthogonal image views (transverse, coronal and sagittal respectively) of the reconstructed image using 3D-OSEM List-Mode algorithm with TOF information.

The first obtained line profiles were trough x- axis (horizontal line) as it is demonstrated in Figure 4.18. For both images, with and without TOF information, represented line profiles have a similar behaviour. The centred point is the one that has a higher number of counts which decrease along the x- axis for the position B and then for the position C. Although the possibility of identifying a similar behaviour for both cases in Figures 4.16 and 4.17, the number of counts presents a huge difference. For the centred point, the number of counts for the TOF imaging appears to be more than 20 times superior. For the position B and C, a great difference is also seen.

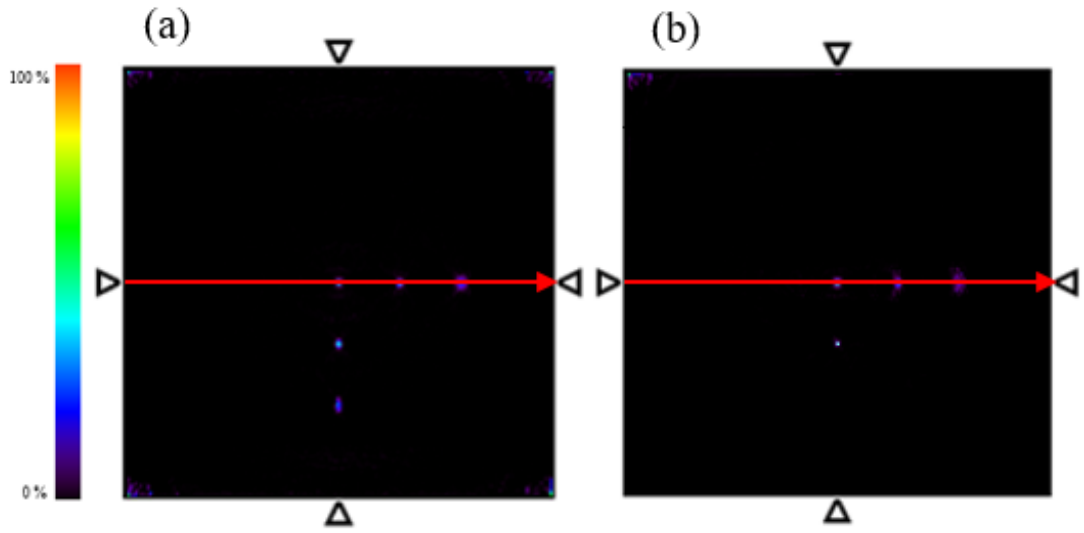

Figure 4.18: Line profile AMIDE Tool over axial slices on horizontal position for reconstructed images using 3D-OSEM List-Mode algorithm without TOF information (a) and with TOF information (b).

As it was referred, line profiles trough y- direction were also obtained for both image reconstructions without and with TOF information using the Line Profile Tool of AMIDE (Figure 4.21). Also here and as it was expected, a big difference on the number of counts is possible to verify for position A and D. Notwithstanding, position E is not possible to identify neither in the line profile neither in the reconstructed image. The variation of counts from point A to point D is much more pronounced in this direction than in x- axis

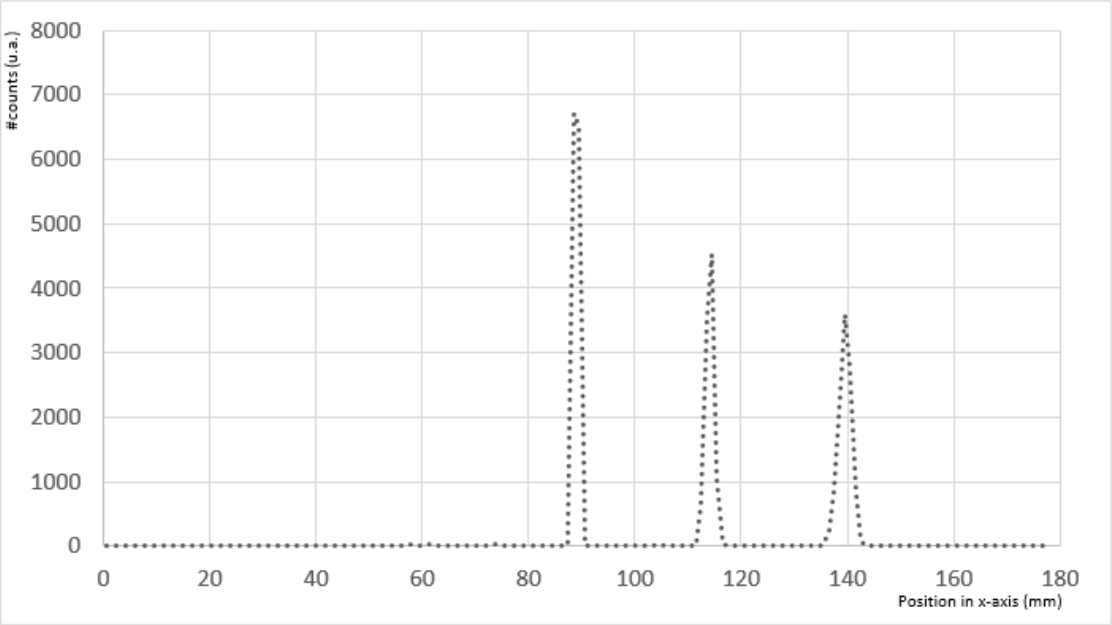

Figure 4.19: Line profiles over axial slices on horizontal position for reconstructed image using 3D-OSEM List-Mode algorithm without TOF information.

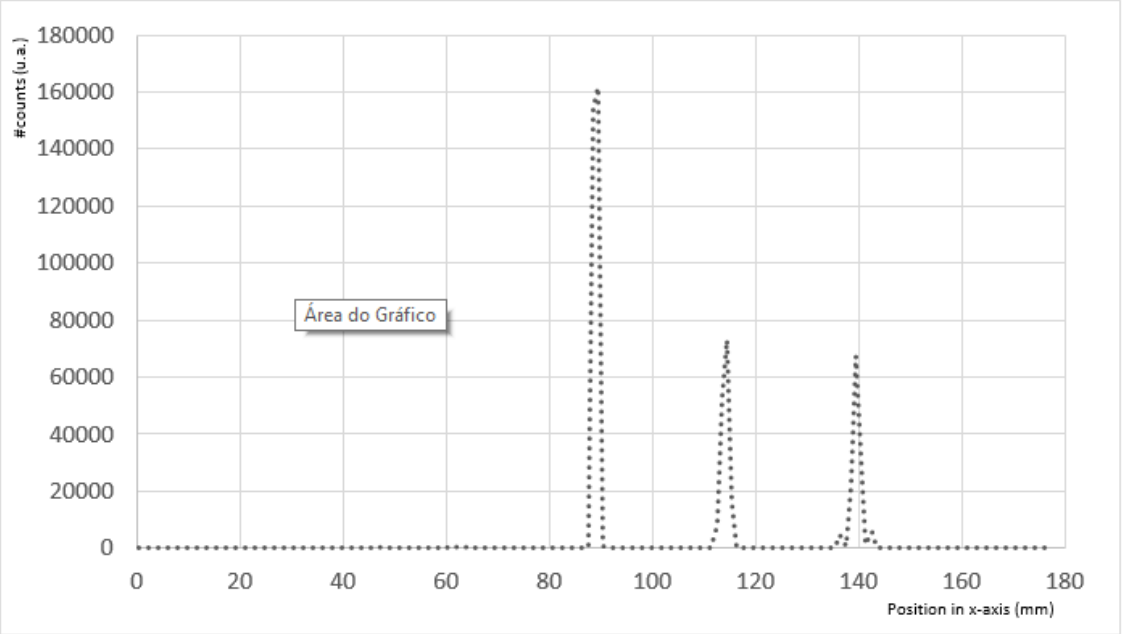

Figure 4.20: Line profiles over axial slices on horizontal position for reconstructed image using 3D-OSEM List-Mode algorithm with TOF information.

for image reconstruction using TOF information. These facts are demonstrated in Figure 4.22 and 4.23 and confirm the existence of a problem with the reconstruction algorithm near the edges of the FOV especially in y- direction when TOF information is added.

At the centre of the FOV (position A), a spatial resolution of approximately 0.95 mm in both transverse directions is verified for the image containing TOF information, which is better than 1.01 mm presented for the image without TOF. All obtained values of spatial resolution in the diferent positions are presented in 4.3. Since, as it was previously referred,

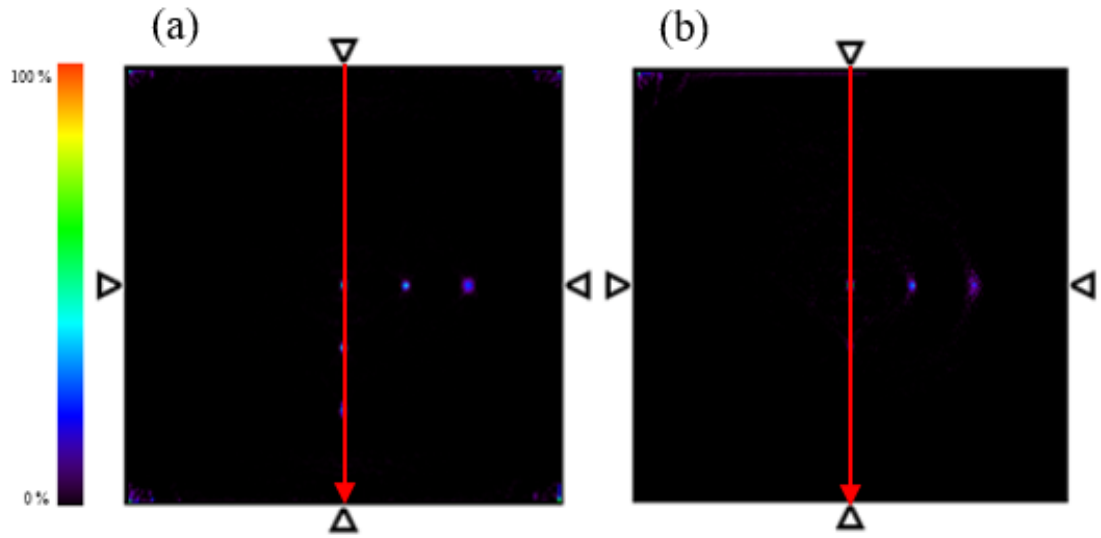

Figure 4.21: Line profile AMIDE Tool over axial slices on vertical position for reconstructed images using 3D-OSEM List-Mode algorithm without TOF information (a) and with TOF information (b).

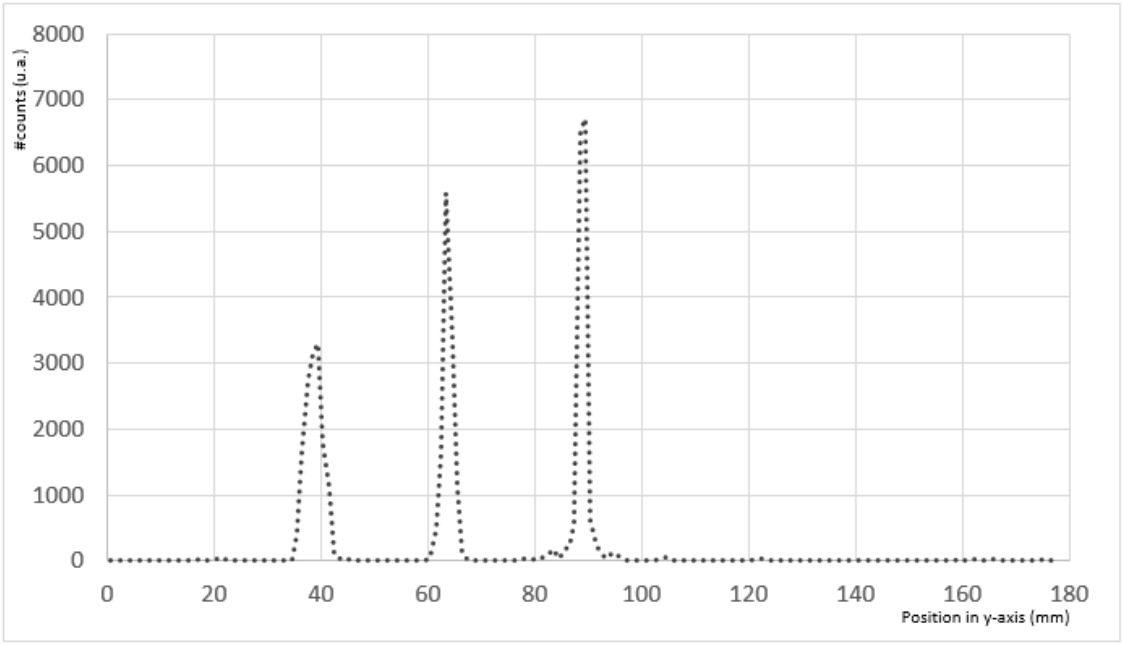

Figure 4.22: Line profiles over axial slices on vertical position for reconstructed image using 3D-OSEM List-Mode algorithm without TOF information.

spatial resolution represents the ability to distinguish between two points of radioactivity in an image, providing information about the precision with which positron emissions can be localized within the object under imaging. Therefore, small values of FWHM corresponds to a better spatial resolution which an important factor in image quality.

In general, values obtained from the image with TOF information presents smaller values of spatial resolution. The only that presents a bigger value is the one simulated in position C. For position C and D, the difference of spatial resolution presented for both images is not significant. This means that only in the central point a significant

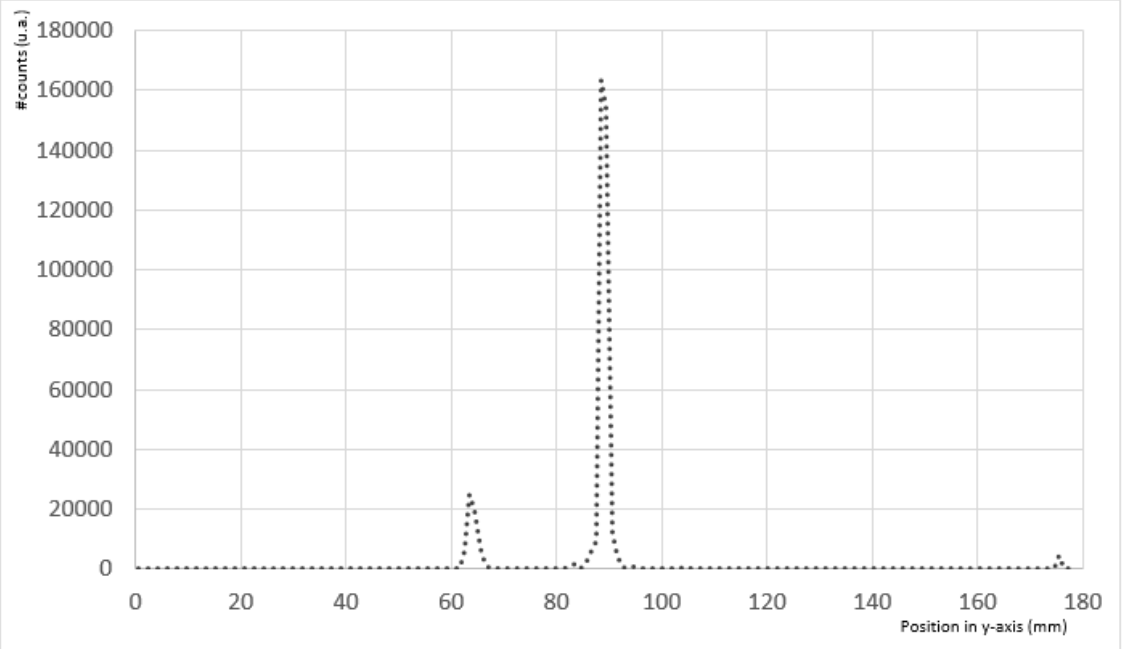

Figure 4.23: Line profiles over axial slices on vertical position for reconstructed image using 3D-OSEM List-Mode algorithm with TOF information.

Table 4.3: Image spatial resolution of the reconstructed point sources with and without TOF information. The spatial resolution is characterized by the FWHM of a Gaussian fit to profiles taken in transverse slice for y- and x- axis (mean values is presented).

	Image without TOF information		**Image with TOF information**	
Source	**FWHM at (0,0,0)mm**	**Uncertainty**	**FWHM at (0,0,0)mm**	**Uncertainty**
A	1.2089	+/-0.0004	0.9486	+/-0.0001
B	2.7143	+/-0.0007	2.5478	+/-0.0001
C	3.3365	+/-0.0008	3.6443	+/-0.0001
D	1.5585	+/-0.0004	1.5573	+/-0.0001
E	1.5129	+/-0.0008	-	-

improvement was verified in spatial resolution when TOF information is added to the image reconstruction method.

The next step of this quantitative analysis is based on a traced region of interest using AMIDE capabilities for ROI statistics calculations. Two ROIs with different dimensions were traced for both images (Figure 4.24 and 4.25). The smaller ROI has a volume of approximately 11 mm^3 and the bigger one a volume of 105 mm^3, covering 46 and 330 voxels of the image respectively. Results for TOF and non-TOF imaging are summarized in table 4.4.

Values were only analysed at position A, since it was the one that represents the ideal case. Based on this, it was verified that the maximum number of counts for the TOF image is more than 20 times higher than for the non-TOF image. Also, a similar ratio is achieved for the mean values of intensities for small ROI that encircles the point source and the big ROI, which represents a better detection sensitivity. Since detection sensitivity refers to the fraction of emitted annihilation photon pairs from the source that are identified as true coincidences by the detection system and contribute to the final reconstructed image.

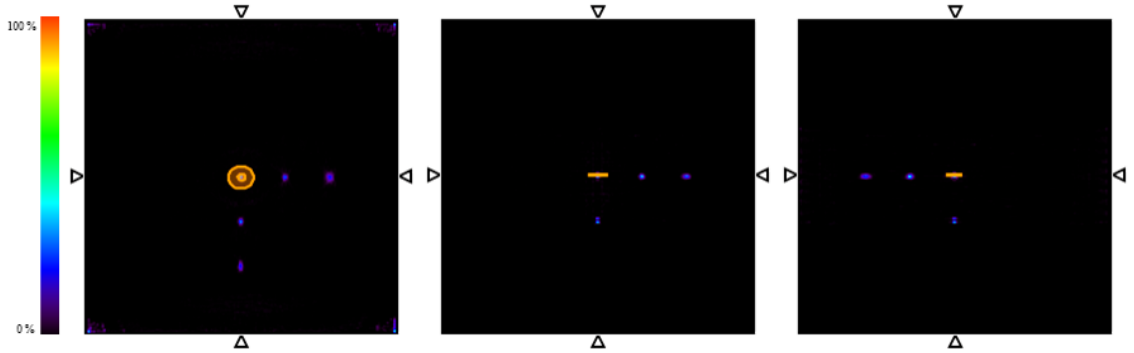

Figure 4.24: Orthogonal image views (transverse, coronal and sagittal respectively) of the reconstructed image using 3D-OSEM List-Mode algorithm without TOF information. In orange are presented the traced ROIs with 10.5 mm and 105.5 mm.

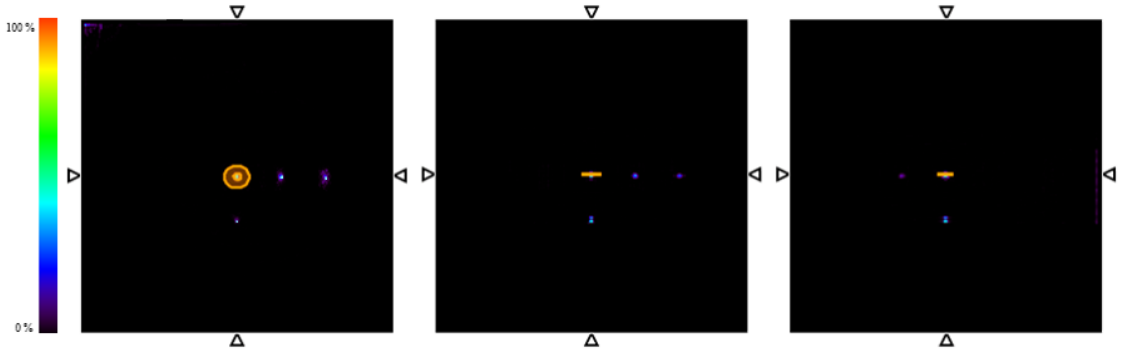

Figure 4.25: Orthogonal image views (transverse, coronal and sagittal respectively) of the reconstructed image using 3D-OSEM List-Mode algorithm with TOF information. In orange are presented the traced ROIs with 10.5 mm and 105.5 mm.

Thus, a higher counting efficiency represents the increase of statistics, which reduces noise level images, while keeping a low radiation dose for the patient.

Noise level reduction is observed by the calculation of the signal-to-noise ratio based on the mean values calculated in the traced ROIs which was already performed and documented by *Enrico Clementel* (Student Member, IEEE) [71]. It is possible to verify that for non-TOF images signal to noise ratio is smaller comparatively with the one obtained for the TOF image. This difference results in a TOF gain of 1.8, which shows the advantage in terms of image SNR when TOF algorithm is used in image reconstruction.

Using this methodology, two more simulations were performed and images were re-

Table 4.4: Images statistics based on the traced ROIs of the reconstructed images with and without TOF information.

	Non-TOF	**TOF**
Maximum Value of Counts	6719	178314
Small ROI (avg. value)	1341.2	34879.6
Big ROI (avg. value)	125.1	2421.85
SNR	1.5	2.0
TOF Gain	1.8	

constructed using 3D-OSEM List-Mode algorithm without and with TOF information. The first performed simulation was a uniform cylindrical phantom with uniform activity distribution. Figure 4.26 shows reconstructed images of the simulated cylinder without TOF (a) and with TOF (b). Qualitatively, it is possible to verify that when phantom image is reconstructed using TOF information shows less noise near to the edge of the detector FOV. Also, the shape of the cylinder presents to be well defined in the image with TOF information. Related to the number of counts, a more intense colour it's possible to verify in TOF imaging, which represents a higher number of counts identified as true coincidences by the detection system and contribute to the final reconstructed image.

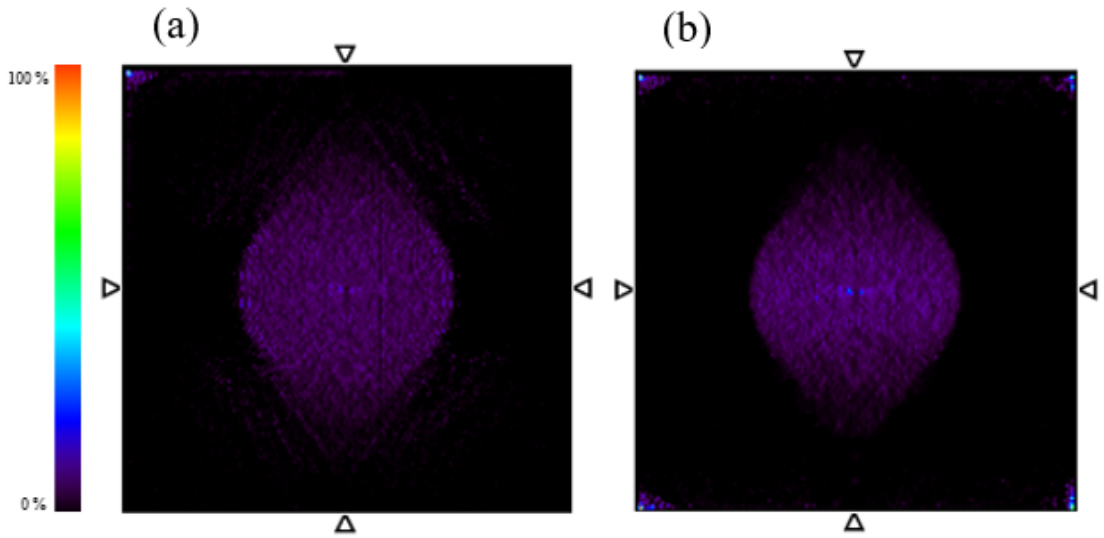

Figure 4.26: Uniform cylinder with diameter of 50 mm, simulated using a realistic simulation in Gate, Images reconstructed using 3D-OSEM List-Mode algorithm without TOF (a) and with TOF information (b).

The next performed simulation was a Derenzo phantom in order to investigate if the intrinsic resolution of the system is enhanced with the use of TOF information in image reconstruction. Figure 4.27shows the Derenzo phantoms images reconstructed without TOF (a) and with TOF information (b). Both images show a well-defined phantom since all the points can be resolved. The biggest difference in both images is the intensity colour of the rods, since for the TOF imaging they present more shine than when non-TOF algorithm is used, which represents a higher number of counts that contribute for final image reconstruction. For this case, problems near to the edge of the detector FOV are not possible to identify.

Based on this, time of flight information seems to be a great add in image reconstruction methodology since it presents to improve PET imaging quality. However, more studies should be performed in order to correct the errors described in this study. It is important to highlight that for the purpose of this study was chosen a constant iteration number for TOF and non-TOF image reconstruction for varying count levels and count statistics. Although it is expected that the data requires a different number of iterations to achieve contrast convergence at different count rates and count statistics, calculating the optimal

number of iterations for each of the datasets would be impractical in the context of this study.

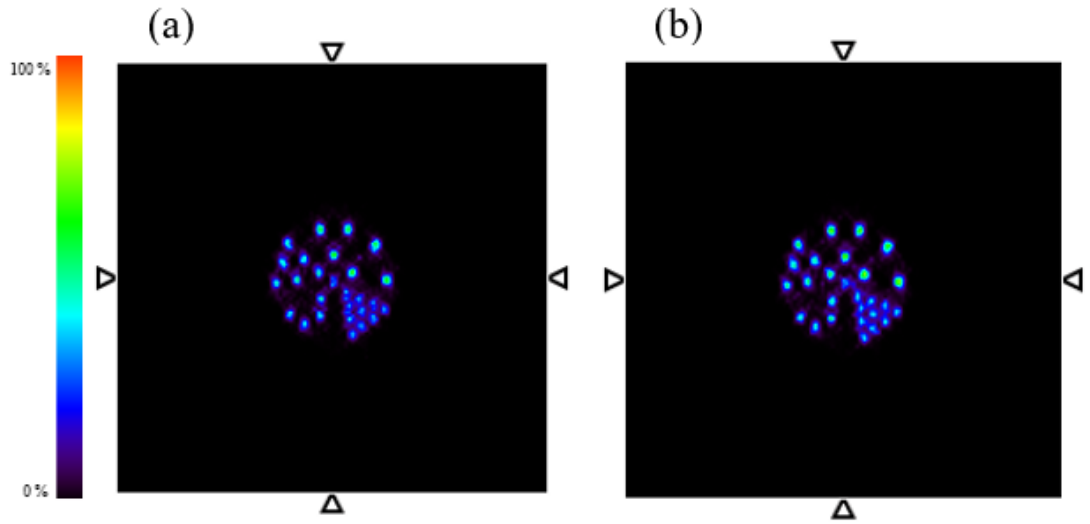

Figure 4.27: Derenzo phantom composed by rods with radius of 1.2 mm, 1 mm, 0.75 mm, 0.675 mm and 0.5 mm, simulated using a realistic simulation in Gate, Images reconstructed using 3D-OSEM List-Mode algorithm without TOF (a) and with TOF information (b).

Chapter 5

Conclusions and Prespectives

The SiPM-based PET-ToF demonstrator is a dedicated PET scanner prototype that aims to significantly improve the detection of early stage breast cancer, comparatively to whole-body PET or even conventional mammography techniques. The lesion detection capability of the SiPM-based PET-ToF prototype will be inherently dependent on the design principles and technological choices made for the detector, in particular regarding the radiation detection photonics, electronics processing, data acquisition capability and image reconstruction. The study of the influence of some of these factors on the image performance of the scanner was the primary objective of the work presented in this thesis. Specially, the geometry of the scanner and software that comprises the reconstruction algorithms chosen for image estimation and the associated normalization process. Also, TOF capabilities of the detector and its benefit in image reconstruction were extensively considered in this work. Studies were conceptualized for the evaluation of the sensitivity, spatial resolution and count rate performance through Monte Carlo simulation techniques.

In order to validate the design of the simulated detector and data acquisition using GATE, a first study was performed to compare experimental data with simulated one. Both data were reconstructed using the same algorithm for image final estimation. This study also allowed the evaluation of the intrinsic spatial resolution of the demonstrator along the axial and the transaxial planes. Reconstructed images of two different phantoms, a point source of Na-22 with 1mm nominal diameter and a Ge-68 line source with 1.5mm diameter and a length of 60mm, were evaluated. Images were reconstructed based on the List-Mode reconstruction algorithm without TOF information explained in chapter 3.3.3. Results obtained for experimental and simulated data were similar for both simulations, which allows us to conclude that the simulation design was well performed and it's possible to use it in further studies. The evaluated values of FWHM obtained to evaluate spatial resolution, were also similar for the simulation and the experimental data. Specifically, for the axial plane, values were better than the ones obtained for the transaxial plane for both sources. Ideally, the resolution in both planes should be the same to permit a true volumetric imaging, which it's not possible to achieve specially due to intrinsically specifications (scintillator material type, crystal dimensions, size of the field-of-view, and others) [6]. The values obtained for spatial resolution, which has the potential to increase lesion detectability, showed improvements comparatively with other recently developed scanners

[48]. It is important to highlight that, during this study, a problem for compensating gaps was observed for the line source image reconstruction. After some research, it was found that this problem could be due to the normalization procedure, which was evaluated in the next study to achieve better image uniformity.

The characterization of the effect of the normalization on image reconstruction was evaluated using computed Monte Carlo sensitivity images. Three different uniform phantoms for system normalization were used, and then the sensitivity image of each one was reconstructed. These sensitivity images are then used as input to normalize the final image estimate in each iteration during image reconstruction. This means that, for this scanner, a direct method for normalization was used, by means of a long acquisition. For all of the obtained sensitivity images, a triangular non-uniform shape peaked at the central slice was verified. It displays a complex pattern that differs considerable from the expected smooth sensitivity profile. This fact could be justified with in-detector effects, as well as the fact that a realistic geometry of the scanner is used which can have a significant effect in the calculated sensitivity images which was already observed during the studies of other systems prototypes, such as the Clear-PEM [13].

In order to understand qualitatively the behaviour of the sensitivity images in final image estimate, data from three different simulated phantoms were obtained and images were reconstructed using as input the three different sensitivity images. For that 3D-OSEM List-Mode algorithm was used. Based on this study, it was possible to conclude that the normalization factors used in image reconstruction as a big influence in the final result obtained. For the three phantoms used for final image estimation, the best results were obtained with using the planar sensitivity image as input, probably due to its thin geometry since it is known as presenting little scatter [13]. Since final image estimation obtained using the planar sensitivity image as input presents lower values of background noise and higher count rates.

Improvement of both spatial resolution and detection sensitivity in PET scanners has the potential to increase lesion detectability, needed for a diagnosis of the disease in early stages where the treatment is usually more effective. Time-of-Flight information in image reconstruction appears to an alternative for noise reduction, faster image convergence and SNR improvement. To evaluate TOF gains in image estimation, a simulation of six point sources were performed and images reconstructed with and without the integration of TOF algorithm in the image reconstruction method were compared.

Using the reconstruction method without TOF information, all the simulated points are similar as it was expected, since all of them as the same shape, dimensions and activity. More irregularities are observed in the near edges of the detector FOV, especially in the transaxial direction. On the other hand, the image obtained from the same simulation but now reconstructed with TOF information, presented a more intensive colour in the central point which means that in this position a higher number of counts were achieved. This statement was confirmed evaluating the correspondent line profiles, since for the central point the number of counts for the TOF imaging appears to be more than 20 times superior. However, using TOF algorithm in image reconstruction it is only possible

to verify 5 point sources, and not 6 as it was expected in the final image. This behaviour was not expected and represents a problem in the image reconstruction software when the source is near the edges of the detector FOV, especially in -y direction. This could be justified by the limited-angle shape of the detector, which corresponds to a limited angular coverage. Similar behaviours were verified in [52] but only when TOF information is not used in the image reconstruction software.

An evaluation of the FWHM was also performed in the aim of this study, since it was expected that with the integration TOF algorithm better values of spatial resolution could be achieved [57]. This fact was verified during this study, since in general values obtained from the image with TOF information presented smaller values of spatial resolution. However, only in the central point a significant improvement was verified in spatial resolution when TOF information is added to the image reconstruction method. In order to verify other TOF benefits, the noise level reduction was also evaluated by the calculation of the signal-to-noise ratio based on the mean values calculated in the traced ROIs which was already performed and documented by *Enrico Clementel* (Student Member, IEEE) [72]. It is possible to verify that for non-TOF images signal to noise ratio was smaller comparatively with the one obtained for the TOF image. This difference results in a TOF gain of 1.8, which shows the advantage in terms of image SNR when TOF algorithm is used in image reconstruction. Based on this, time of flight information seems to be a great add in image reconstruction methodology since it presents to improve PET imaging quality which was already verified in previous studies [51, 54].

In the scope of this study, two more simulations were performed and images were reconstructed using 3D-OSEM List-Mode algorithm without and with TOF information. For both cases, images obtained show well-defined shapes. The biggest difference is in the intensity colour, since for the TOF imaging they presented more shine than when non-TOF algorithm is used, which represents a higher number of counts that contribute for final image reconstruction. For these images, problems near to the edges of the detector FOV were not possible to identify. This work attempts to quantify the TOF benefit using simulated data and shows results that are consistent with the phantom studies. Studies to assess how these results translate to clinical diagnosis and patient management are needed after the correction of the errors found.

Future Prespectives

During the execution of this Master Thesis work, adaptation to new conditions and reformulation of the initial approaches was a constant and an essential factor to account for. However, limitations in terms of time hindered the feasibility of testing some alternative approaches. The general trend of the simulation results presented in this thesis, foresees a good performance of the SiPM-based PET-ToF prototype in image estimation, supporting the design and technological choices made for the detector.

Nevertheless, some errors were found during the evaluation of the obtained results specially when TOF algorithm was introduced in the image reconstruction method. This

means that, more studies should be performed in order to obtain the expected results. Since the integration of TOF information in image reconstruction technique seems to be a great add in image reconstruction without the need of spending money in detector electronic and components. Also, in the aim of further studies the simulation of realistic breasts with different characteristics of density, sizes and types of carcinomas should be performed to evaluate more carefully the viability of the SiPM-based PET-TOF demonstrator in the detection of early stage breast cancer. In addition, faster scintillators for better timing resolution and more computationally efficient reconstruction approaches should be studied and adaptation for multi-modality imaging can be also considered.

References

[1] Lao, D., Lenox, M. W., and Akabanil, G. (2013). The sparsity-promoted solution to the undersampling TOF-PET imaging: numerical simulations. Progress in Electromagnetics Research, Vol 133, 235-258, 2013.

[2] Wallace, A. M., Comstock, C., Hoh, C. K., and Vera, D. C. (2005). Breast imaging: a surgeon's prospective. Nuclear medicine and biology, 32(7):781-792.

[3] Muehllehner, G. and Karp, J. S. (2006). Positron emission tomography. Physics in medicine and biology, 51(13):R117.

[4] Hruska, C. B. and O'Connor, M. K. (2013). Nuclear imaging of the breast: Translating achievements in instrumentation into clinical use. Medical physics, 40:050901.

[5] Glenn G. Gray, MD, Richard J. Katz, MD. "Sarcoidosis", 2003. Radiological Case of the Month in http://www.medscape.com/viewarticle/448598

[6] Cherry, S. and Dahlbom, M. PET: Physics, Instrumentation, and Scanners. In Phelps, M. E., editor, PET, pages 1-117. Springer New York. 2006.

[7] Matela, N. (2008). 2D Iterative Image Reconstruction for Dual Planar Detector for Positron Emission Mammography. PhD thesis, Faculdade de Ciências, Universidae de Lisboa.

[8] Champion, C. and Le Loirec, C. Positron follow-up in liquid water: II. Spatial and energetic study for the most important radioisotopes used in PET (2008). Physics in medicine and biology, 52(22):6605.

[9] C. Ferreira, "The Clear-PEM detector in breast cancer: correction methods for improved imaging" Ph.D. dissertation, Instituto Superior Técnico, Universidade de Lisboa,Portugal, 2014.

[10] Martins, M. V. (2007). 3D Image Reconstruction for a Dual Plate Positron Emission Tomograph: Application to Mammography. PhD thesis, Faculdade de Ciências, Universidade de Lisboa.

[11] Strother SC, Casey ME, Hoffman EJ. (1990). Measuring PET scanner sensitivity: relating count rates to image signal-to-noise ratios using noise equivalent counts. IEEE Trans Nucl Sci 37(2):783e8.

[12] Badawi, R., Lodge, M., and Marsden, P. "Algorithms for calculating detector efficiency normalization coefficients for true coincidences in 3d pet. Physics in medicine and biology, 1998.

[13] Rodrigues, A. "Design and Evaluation of a Positron Emission Tomograph for Breast Cancer imaging". PhD Thesis, Instituto Superior Técnico, Universidade de Lisboa, 2007.

[14] Bugalho R., Ferramacho L., Franscesco A. et al. "A SiPM-based PET TOF demonstrator featuring a highly integrated readout and DAQ system". PETsys Electronics, LIP and Vrije Universiteit Brussel. December 2015.

[15] S. R. Cherry, J. A. Sorenson, and M. E. Phelps. "Physics in nuclear Medicine (3rd edition)", chapter 16 – Tomographic reconstruction in nuclear medicine, pages 273-294. W. B. Saunders Co, Elsevier, March 2003.

[16] J. Qi and R. M. Leahy. "Iterative reconstruction techniques in emission computed tomography". Phys. Med. Biol., 51:R541-78, 2006.

[17] M. Lubberink, R. Boellaard, A. P. van der Weerdt, C. F. Visser, and A. A. Lammertsma. "Quantitative comparison of analytic and iterative reconstruction methods in 2- and 3- dimensional dynamic cardiac 18F-FDG PET", J. Nucl. Med., 45:2008-15,2004.

[18] R. Gordon, R. Bender, and Herman G. T. "Algebraic reconstruction techniques (ART) for three-dimensional electron microscopy and X-ray photography". J. Theor. Biol., 29:471-81, 1970.

[19] L. A. Sheep and Y. Vardi. "Maximum Likelihood reconstruction for emission tomography". IEEE Trans. Med. Imaging, 13:601-91, 1994.

[20] Giammarile, F. and Bremond, A. "Diagnostic of breast cancer: what do clinicians expect from PEM?" Nuclear Instruments and Methods in Physics Research Section A: Accelerators, Spectrometers, Detectors and Associated Equipment, 527(1):83-86, 2004.

[21] M. Martins, "Positron Emission Mammography", Chapter 3 in "Mammography Techniques and Review", p. 39-62, Intech 2015.

[22] P. Shreve and D.W. Townsend (eds.), "Clinical PET-CT in Radiology: Integrated Imaging in Oncology", DOI 10.1007/978-0-387-48902-52, Springer Science and Business Media, LLC 2011.

[23] Conti M, Townsend DW, Casey ME, Lois C, Jacoby BW, Long MJ, et al. (2008). Assessment of the clinical potential of a time-of-flight PET/CT scanner. SNM Annual Meeting Proceedings, New Orleans, Louisiana.

[24] Surti, S. (2015). Update on Time-of-Flight PET Imaging. J Nucl Med 56:98–105.

[25] Snyder DL, Thomas LJ, Terpogossian MM. (1981). A mathematical model for positron emission tomography systems having time-of-flight measurements. IEEE Trans Nucl Sci. 28:3575–3583.

[26] Moses, William W. (2007). Recent advances and future advances in time-of-flight PET. Nuclear Instruments and Methods in Physics Research A, 580:919–924.

[27] Kyba CCM, Wiener RI, Newcomer FM, Van Berg R, Dressnandt N, Karp JS. (2007). Timing measurements from a TOF-PET scanner using local PMT triggering. IEEE, Nuclear Science Symposium Conference Record, Honolulu, Hawaii.

[28] Jacobson, M., Levkovitz, R., Ben-Tal, A., Thielemans, K.,Spinks, T., Belluzo, D., Pagani, E., Bettinardi, V., Gilardi, M., Zverovich, A., et al. (2000). Enhanced 3D PET OSEM reconstruction using inter-update Metz filtering. Physics in medicine and biology, 45(8):2417.

[29] Anger HO. (1966) Survey of radioisotope cameras. ISA Trans. 5:311–334.

[30] Brownell GL, Burnham CA, Wilensky S, Aronow S, Kazemi H, Streider D. (1969) New developments in positron scintigraphy and the application of cyclotron produced positron emitters. In: Medical Radioisotope Scintigraphy. Vol 1. Vienna, Austria: IAEA; 163–176.

[31] Budinger TF. (1977). Instrumentation trends in nuclear medicine. Semin Nucl Med. 7:285–297.

[32] Ter-Pogossian MM, Ficke DC, Hood JT Sr, Yamamoto M, Mullani NA. (1982). PETT VI: a positron emission tomograph utilizing cesium fluoride scintillation detectors. J Comput Assist Tomogr. 6:125–133.

[33] Ter-Pogossian M, Ficke D, Yamamoto M, Hood JT. (1982). Super PETT I: a positron emission tomograph utilizing photon time-of-flight information. IEEE Trans Med

Imaging. M1-1:179–187.

[34] Gariod R, Allemand R, Cormoreche E, Laval M, Moszynski M. (1982). The "LETI" positron tomograph architecture and time-of-flight improvements. In: Proceedings of IEEE Workshop on Time-of-Flight Emission Tomography. St. Louis, MO: Washington University; 25–29.

[35] Wong WH, Mullani NA, Philippe EA, et al. (1984). Performance characteristics of the University of Texas TOF PET-I camera [abstract]. J NuclMed. 25:P46–P47.

[36] Lewellen TK, Bice AN, Harrison RL, Pencke MD, Link JM. (1988). Performance measurements of the SP3000/UW time-of-flight positron emission tomograph. IEEE Trans Nucl Sci. 35:665–669.

[37] Mazoyer B, Trebossen R, Schoukroun C, et al. (1990). Physical characteristics of TTV03, a new high spatial resolution time-of-flight positron tomograph. IEEE Trans Nucl Sci. 37:778–782.

[38] Allemand R, Gresset C, Vacher J. (1980). Potential advantages of a cesium fluoride scintillator for a time of flight positron camera. J Nucl Med 21:153e5.

[39] Laval M, Moszynski M, Allemand R, Cormoreche E, Guinet P, Odru R, et al. (1983). Barium fluoridedInorganic scintillator for subnanosecond timing. Nucl Inst Methods 206:169e76.

[40] Ishii K, Orihara H, Matsuzawa T, Binkley DM, Nutt R. (1990). High resolution time-of-flight positron emission tomograph. Rev Sci Instr. 61(12):3755e62.

[41] Soussaline S, Comar D, Allemand R, Campagnolo R, Laval M, Vacher J, et al. (1985). New developments in positron emission tomography instrumentation using the time-of-flight information. In: Gretz T, editor. The metabolism of the human brain studied with positron emission tomography. New York: Raven Press; p. 1e11.

[42] Lewellen TK. (1998). Time-of-flight PET. Semin Nucl Med 28(3):268e75.

[43] Melcher CL, Schweitzer JS. (1992). Cerium-doped lutetium orthosilicate: a fast, efficient new scintillator. IEEE Trans Nucl Sci 39:502e5.

[44] Moses WW, Derenzo SE. (1999). Prospects for time-of-flight PET using LSO scintillator. IEEE Trans Nucl Sci 46(3):783e8.

[45] Conti M, Bendriem B, Casey M, Chen M, Kehren F, Michel C, et al. (2004).

Implementation of time-of-flight on CPS HiRez PET scanner. IEEE Nuclear Science Symposium Conference Record, Rome, Italy.

[46] Conti M, Bendriem B, Casey M, Chen M, Kehren F, Michel C, et al. (2005). First experimental results of Time-Of-Flight reconstruction on an LSO PET scanner. Phys Med Biol 50:4507e26.

[47] Surti S, Karp JS, Muehllehner G, Raby PS. (2003). Investigation of lanthanum scintillators for 3-D PET. IEEE Trans Nucl Sci 50(3):348e54.

[48] M. Martins, "Positron Emission Mammography", Chapter 3 in "Mammography Techniques and Review", p. 39-62, Intech 2015.

[49] Surti S, Kuhn A, Werner ME, Perkins AE, Kolthammer J, Karp JS. (2007). Performance of Philips Gemini TF PET/CT scanner with special consideration for its time-of-flight imaging capabilities. J Nucl Med 48(3):471e80.

[50] S. VandenbergheEmail author, E. Mikhaylova, E. D'Hoe, P. Mollet and J. S. Karp. "Recent developments in time-of-flight PET" EJNMMI Physics20163:3, February 2016.

[51] Surti S, Karp JS. (2009). Experimental evaluation of a simple lesion detection task with time-of-flight PET. Phys Med Biol. 54:373–384.

[52] M. Martins, "Positron Emission Mammography", Chapter 3 in "Mammography Techniques and Review", p. 39-62, Intech 2015

[53] Loening AM1, Gambhir SS. "AMIDE: a free software tool for multimodality medical image analysis." Mol Imaging. 2003 Jul;2(3):131-7.

[54] Conti, Maurizio (2009). State of the art and challenges of time-of-flight PET. Physica Medica 25, 1e11.

[56] Conti M. (2006). Effect of random reduction on signal-to-noise-ratio in TOF PET. IEEE Trans Nucl Sci 53(3):1188e93.

[57] Karp JS, Surti S, Daube-Witherspoon ME, Muehllehner G. (2008). Benefit of time-of-flight in PET: experimental and clinical results. J Nucl Med. 49:462–470.

[58] M. Jacobson, R. Levkovitz, A. Ben-Tal, K. Thielemans, T. Spinks, D. Belluzzo, E. Pagani, V. Bettinardi, M. Gilardi, A. Zverovich, et al., "Enhanced 3D PET OSEM reconstruction using inter-update Metz filtering," Physics in Medicine and Biology, vol. 45, no. 8, p. 2417, 2000.

[59] Ollinger, J. “Detector efficiency and Compton scatter in fully 3D PET. Nuclear Science, IEEE Transactions on, 42(4):1168-1173, 1995.

[60] C. Ferreira, “The Clear-PEM detector in breast cancer: correction methods for improved imaging” Ph.D. dissertation, Instituto Superior Técnico, Universidade de Lisboa,Portugal, 2014.

[62] Townsend D, Schorr B, Jeavons A. (1980) 3-Dimensional Image-Reconstruction for a Positron Camera with Limited Angular Acceptance. IEEE Trans. Nucl. Sci; 27:463–470.

[63] A. J. Reader, S. Ally, F. Bakatselos, R. Manavaki, R. J. Walledge, A. P.Jeavons, P. J. Julyan, S. Zhao, D. L. Hastings, and J. Zweit, “One-pass list-mode em algorithm for high-resolution 3-d pet image reconstruction into large arrays,” IEEE Transactions on Nuclear Science, vol. 49, no. 3, pp. 693–699, 2002.

[64] Liji Cao, Ricardo Bugalho, Cláudia Ferreira, Catarina Ortigão, Ricardo Capote, João Varela, and Jorg Peter. “A Fast List-Mode Reconstruction Algorithm with Dedicated Correction for Random Coincidences for the Clear-PEM System”. IEEE Transactions on Nuclear Science Vol 61, 3. Pp 1182 – 1191, 2014.

[65] J. Liow and S. Strother, “Noise and signal decoupling in maximum likelihood reconstructions and Metz filters for PET brain images,” Physics in Medicine and Biology, vol. 39, no. 4, p. 735, 1994.

[66] R. Lewitt and G. Muehllehner, “Accelerated iterative reconstruction for positron emission tomography based on the EM algorithm for maximum likelihood estimation,” IEEE Transactions on Medical Imaging, vol. 5, no. 1, pp. 16–22, 1986.

[67] A. Rahmim, M. Lenox, A. Reader, C. Michel, Z. Burbar, T. Ruth, and V. Sossi, “Statistical list-mode image reconstruction for the high resolution research tomograph,” Physics in medicine and biology, vol. 49, no. 18, p. 4239, 2004.

[68] R. Siddon, “Fast calculation of the exact radiological path for a threedimensional CT array,” Medical physics, vol. 12, no. 2, p. 252, 1985.

[69] Shepp, L. A, and Vardi, Y. (1982). Maximum Likelihood reconstruction for emission tomography. Medical Imaging, IEEE Transactions on 1(2):113-122.

[70] Cao, L., Bugalho, R., Matela, N., Martins, M., Almeida, P., Peter, J. and Varela, J.. (2011) List-Mode Maximum-Likelihood Reconstruction for the ClearPEM System. In Nuclear Science Symposium conference Record, 2011 IEEE, pages 4171-4174.

[71] Clementel E., Vandenberghe S., Karp J. S. “Evaluation of image Signal-to-Noise Ratio in Time-of-Flight PET” Nuclear Science Symposium Conference Record (NSS/MIC), 2010 IEEE. December 2010.